D 3.5

DELIVERABLE

PROJECT INFORMATION

Project Title:	**Harmonized approach to stress tests for critical infrastructures against natural hazards**
Acronym:	**STREST**
Project N°:	603389
Call N°:	FP7-ENV-2013-two-stage
Project start:	01 October 2013
Duration:	36 months

DELIVERABLE INFORMATION

Deliverable Title:	**Report on cascading events and multi-hazard probabilistic scenarios**
Date of issue:	27 March 2015
Work Package:	WP3 – Integrated low probability-high consequence hazard assessment for critical infrastructures
Editor/Author:	Arnaud Mignan (ETH Zurich, SEG)
Reviewer:	Bozidar Stojadinovic (ETH Zurich, IBK)

REVISION: Version 2

Project Coordinator:	Prof. Domenico Giardini
Institution:	ETH Zürich
e-mail:	giardini@sed.ethz.ch
fax:	+ 41 446331065
telephone:	+ 41 446332610

Abstract

Developing upon the generic multi-risk (genMR) framework developed by Mignan et al. (2014) in the scope of the *New Multi-Hazard and Multi-Risk Assessment Methods for Europe* (MATRIX) project, we generate probabilistic multi-hazard scenarios in which cascades of events emerge from natural hazard correlations. We investigate the characteristics of the cascades under various parametric conditions and discuss of their possible inclusion in stress tests of critical infrastructures. Focus is made on three types of hazard interactions: (1) "intra-event" earthquake triggering based on concepts of dynamic stress to evaluate the maximum magnitude M_{max} of cascading fault ruptures, (2) "intra-hazard" earthquake triggering based on the theory of Coulomb stress transfer to evaluate earthquake spatiotemporal clustering and (3) various "inter-hazard" interactions at dams (impact of earthquakes, floods, internal erosion, and malfunctions on dam and foundation, spillway, bottom outlet and hydropower system). Each hazard interaction type is applied to a specific site, respectively: Turkey (CI-B1: Hydrocarbon pipelines), northern Italy (CI-C1: Industrial district), and Switzerland (CI-A2: Dams).

Keywords: Hazard interactions; genMR; earthquake clustering; maximum earthquake magnitude; cascades at dams; risk migration; risk amplification; stress tests

Acknowledgments

The research leading to these results has received funding from the European Community's Seventh Framework Programme [FP7/2007-2013] under grant agreement n° 603389

Deliverable Contributors

ETH Zurich	Arnaud Mignan (all sections)
	Laurentiu Danciu (sections 3-4)
EPFL	José P. Matos (section 5)
	Anton Schleiss (section 5)

Table of Contents

Abstract i

Acknowledgments iii

Deliverable Contributors v

Table of Contents vii

List of Figures ix

List of Tables xi

1 Introduction 1

2 Generic Multi-Risk (GenMR) Framework 3

- 2.1 METHOD 3
  - 2.1.1 Sequential Monte Carlo method 3
  - 2.1.2 Multi-hazard terminology 4
- 2.2 PROOF-OF-CONCEPT 4
  - 2.2.1 Abstraction of perils and hazard interactions 4
  - 2.2.2 Concept of Virtual City 11
- 2.3 APPLICATION TO REAL-WORLD CONDITIONS 12

3 Intra-Event Interactions: Intra-Earthquake Triggering (Inference on M_{max}) 15

- 3.1 INTRODUCTION 15
- 3.2 METHOD & DATA 16
  - 3.2.1 Appraisal of criteria for multi-segment rupture from the dynamic stress modelling literature 16
  - 3.2.2 Multi-segment rupture method assumptions and limitations 18
  - 3.2.3 The ESHM13 database 19
  - 3.2.4 Assessment of M_{max} considering individual fault segment lengths or cascade lengths 20
- 3.3 RESULTS 22
  - 3.3.1 Strike-slip cascades in the Anatolian Peninsula 22
  - 3.3.2 Reassessment of M_{max} considering rupture cascade lengths in the Anatolian Peninsula 23
- 3.4 IMPLICATIONS FOR STRESS TESTS 25
- 3.5 APPENDIX: MULTI-SEGMENT RUPTURE ALGORITHM 27

4 Intra-Hazard Interactions: Earthquake-Earthquake Interactions 31

4.1 INTRODUCTION 31
4.2 METHOD 32
4.2.1 Theory of earthquake interactions 32
4.2.2 Sensitivity analysis 32
4.2.3 GenMR implementation 33
4.2.4 Generic building & damage assessment 34
4.3 APPPLICATION: NORTHERN ITALY (GENERIC BUILDING) 36
4.3.1 Stochastic event set 36
4.3.2 HCM_{EQ-EQ} 39
4.3.3 Generic building and damage assessment in northern Italy 40
4.3.4 Results 42
4.4 IMPLICATIONS FOR STRESS TESTS 46
5 Inter-Hazard Interactions: Case of Large Dams 49
5.1 OVERVIEW 49
5.1.1 Introduction 49
5.1.2 Brief account of a dam’s main components and operation 50
5.1.3 Historical perspective 52
5.2 THEORY 53
5.2.1 On current design practices and safety criteria for large dams 53
5.2.2 Brief overview of relationships between natural hazards affecting dams 55
5.2.3 Evaluating risks associated with dams using the Multi-Risk (GenMR) framework 56
5.3 EXPLORATORY APPLICATION TO A REPRESENTATIVE DAM 57
5.3.1 Introduction 57
5.3.2 Characterization of hazards 57
5.3.3 Characterization of system elements 61
5.4 RESULTS AND DISCUSSION 65
5.4.1 Analysis of system responses 65
5.4.2 On the influence of hazard interactions 68
5.5 CONCLUSIONS 69
6 General Conclusions 70
References 73

List of Figures

Fig. 1.1 Top-down brick-by-brick approach to multi-risk assessment....................................2

Fig. 2.1 The generic multi-risk (genMR) framework (Mignan et al., 2014)..............................3

Fig. 2.2 Characterization of generic primary perils (Mignan et al., 2014) 6

Fig. 2.3 Example of hazard correlation matrix (HCM) (Mignan et al., 2014)...........................8

Fig. 2.4 Quantification of generic one-way causal effects (Mignan et al., 2014) 9

Fig. 2.5 Risk migration (Mignan et al., 2014) 10

Fig. 2.6 Risk amplification (Mignan et al., 2014)...10

Fig. 2.7 Risk migration matrix (modified from Mignan et al., 2014) 11

Fig. 2.8 Concept of Virtual City 12

Fig. 3.1 Different types of fault segment association 17

Fig. 3.2 Criteria for multi-segment rupture 18

Fig. 3.3 ESHM13 fault map of the Anatolian Peninsula 20

Fig. 3.4 ESHM13 length-M_{max} relationships (strike-slip, Anatolian Peninsula) 21

Fig. 3.5 Examples of generated strike-slip cascades 23

Fig. 3.6 Length-M_{max} scaling for cascades (strike-slip, Anatolian Peninsula) 24

Fig. 3.7 M_{max} maps (ESHM13; Δ = 5 km; Δ = 10 km)...26

Fig. 3.8 Illustration of step 2.3 of the algorithm 28

Fig. 3.9 Rupture cascade length distribution at different iterations.......................................29

Fig. 3.10 Maximum cascade length L_{max} per iteration..30

Fig. 4.1 Sensitivity of the mean conditional probability to the parameter set θ.....................33

Fig. 4.2 Generic building capacity curve, matching damage states & fragility curves 36

Fig. 4.3 Simplified surface projection of the 20 ESHM13 shallow thrust composite faults ITC*xxxx* in northern Italy...37

Fig. 4.4 Coulomb stress changes $\Delta\sigma_f(EQ_1, EQ_j)$ due to EQ_1 on receiver faults....................40

Fig. 4.5 Earthquake hazard & damage footprints (incl. aleatoric uncertainties) for EQ_3.......41

Fig. 4.6 Distribution of the number of earthquakes per simulated year 42

Fig. 4.7 Risk migration matrix (RMM) for strong earthquake clustering & poor building performance 43

Fig. 4.8 "Delta-loss" curve matching the RMM of Figure 4.7 44

Fig. 4.9 RMM for different clustering and building performance levels.................................45

Fig. 4.10 N_{DS4+} distribution for one characteristic earthquake...46

Fig. 4.11 Stress test design using the RMM (Mignan et al., in press, b) 47

Fig. 5.1 Scheme of hazards, elements, system states, and interactions considered in the application of the GenMR framework to large dams 56

Fig. 5.2 Medvedev-Sponheuer-Karnik (MSK) intensities of ground shaking admitted for the area under study 58

Fig. 5.3 Peak ground accelerations (PGA) admitted for the area under study 58

Fig. 5.4 Peak flood inflows to the reservoir 59

Fig. 5.5 Probability density of a flood's duration 59

Fig. 5.6 Normalized hydrograph of flood inflows..60

Fig. 5.7 Admitted probability of occurrence of a flood throughout the year 60

Fig. 5.8 Intensity of internal erosion events admitted for the dam under study 60

Fig. 5.9 Vulnerability curve of the dam and foundation to earthquakes................................61

Fig. 5.10 Illustration of possible slip lines corresponding to the admitted dam damage states 61

Fig. 5.11 Vulnerability of the spillway element to earthquakes 62

Fig. 5.12 Vulnerability of the bottom outlet element to earthquakes....................................62

Fig. 5.13 Distribution of the damage induced to the bottom outlet element by equipment malfunction 62

Fig. 5.14 Vulnerability of the hydropower system to earthquakes 63

Fig. 5.15 Distribution of the damage induced to the hydropower system by equipment malfunction 63

Fig. 5.16 Expected inflows into the reservoir 64

Fig. 5.17 Target volume of the reservoir throughout the year. Normalized in respect to the volume of the reservoir at the spillway level..64

Fig. 5.18 Maximum outflows of the reservoir as a function of the normalized volume of the reservoir 65

Fig. 5.19 Illustrative response of the system to a design earthquake (T=10 000 yr) and associated flood (T≈316 yr). 66

Fig. 5.20 Illustrative response of the system to an extreme earthquake (T≈31 600 yr), leading to overtopping and consequent dam failure..67

Fig. 5.21 Illustrative response of the system to clustering of extreme earthquakes (trigger with T≈31 600 yr), leading an event of internal erosion and dam failure 68

List of Tables

Table 2.1 Multi-risk hypotheses H_i 9

Table 3.1 Length-magnitude scaling relationships (1: ESHM13, 2: Stirling et al. (2013), 3: present study) 22

Table 4.1 Stochastic earthquake set 38

Table 5.1 Comparison between theoretical and simulated return periods for internal erosion events. 69

1 Introduction

Recent major catastrophes have been shown to be the result of cascading processes at the hazard and risk level. Some of the most infamous examples are (i) the 2005 hurricane Katrina, which produced a surge large enough to breach levees, ultimately triggering the wide-scale flooding of the city of New Orleans (Comfort, 2006) and (ii) the 2011 Tohoku earthquake, whose unexpected high magnitude triggered a tsunami larger than planned in the protection of the Fukushima nuclear power plant, therefore triggering a major nuclear accident with radioactive material release along with other industrial accidents (Norio et al., 2011). Catastrophes including cascading components are not a novelty and many examples through history exist. For instance, the 1755 Lisbon earthquake (Muir-Wood and Mignan, 2009) triggered a tsunami as well as fires and had long-term consequences on society, politics and philosophy (Marques, 2005). Similarly the 1906 San Francisco earthquake damaged gas and water supply; both combined yielded extreme fires, destruction of most of the city and financial panic (Odell and Weidenmier, 2001). Another example, of a different triggering type, more local and yet with dramatic consequences, is the 1963 Vajont landslide in a water reservoir, which triggered a tsunami in the artificial lake, dam over-topping and finally downstream flooding with the destruction of several villages (Kilburn and Petley, 2003). If multi-risk appears even more problematic today, it is due to amplifying factors related to human development. With the exponential growth of population and urbanization, risks increase relative to a constant hazard background (e.g., Bihlam, 2009) while there is a potential for more trigger events (hazards so far "dormant", e.g., Mignan et al., 2011) and for more consequences (more technological accidents; Petrova and Krausmann, 2011). Moreover our modern society becomes more complex with networks becoming larger and more interconnected, potentially leading to more cascading effects (e.g., Adachi and Ellingwood, 2008). Finally, global warming increases the intensity and clustering of storms, again yielding more cascading effects, such as floods and landslides (van Aalst, 2006).

While science is catching up to consider all of these aspects, there are still some important limitations in multi-risk analysis, which can be considered a nascent sub-field of risk management. In a review on multi-risk, Kappes et al. (2012) stated that "*despite growing awareness of relations between hazards, still neither a uniform conceptual approach nor a generally used terminology is applied*". It is explained by the fact that cross-disciplinary modelling remains marginal. Indeed, although cascade processes are integrated into innovative models (e.g., complex interdependent networks, Natech engineering, physics and statistics of natural hazard clustering), those models have yet to be combined to provide a comprehensive approach to multi-risk. After the 2011 Fukushima disaster, it was emphasized that "*we need to mobilize scientific imagination in the process of decision*" (Kameda, 2012). The term "*reasoned imagination*" has also been proposed (Paté-Cornell, 2012). Multi-risk model are often based on a limited number of interactions observed in past catastrophes. It means that we may possibly be always one step behind a new "surprise" event, which relates to the concept of Black Swan and unpredictability of the unknown (Taleb, 2007). In order to tackle these various issues, Mignan et al. (2014) proposed a generic multi-risk (genMR) framework, developed in the scope of the *New Multi-Hazard and Multi-Risk Assessment Methods for Europe* (MATRIX) project. The aim of genMR is to help better understanding the different aspects of multi-hazard and multi-risk, to define a common terminology and to integrate knowledge from various types of models into a same framework. The long-term goal of genMR is, by a top-down approach (Fig. 1.1), to develop a comprehensive model of multi-hazard and multi-risk to improve multi-risk management (including stress tests). The framework is described in detail in Section 2.

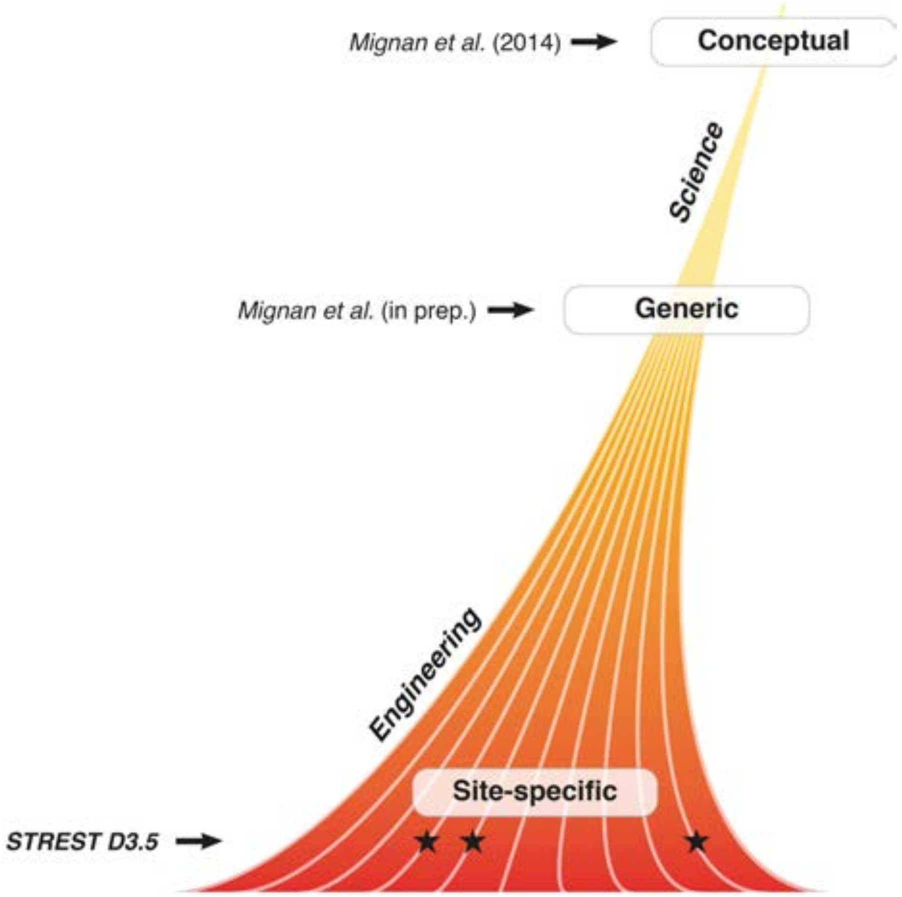

Fig. 1.1 Top-down brick-by-brick approach to multi-risk assessment

So far, genMR has been tested and validated at the conceptual level (Mignan et al., 2014) and at a “simplified reality” level with the development of the Virtual City concept by A. Mignan (Komendantova et al., 2014; Mignan et al., “*The Quantification of Low-Probability–High-Consequences Events: Part II. Guidelines to Multi-Risk Assessment Based on the Virtual City Concept*”, in prep.). In the scope of the STREST project (Work Package WP3), we aim at testing the framework with site-specific applications by determining how various models that compute cascade phenomena, developed in different fields of expertise, can be combined and integrated into genMR. We consider models of dynamic stress transfer for earthquake rupture propagation/cascading, static stress transfer for earthquake/earthquake interactions, and empirical models for the impact of earthquakes, floods and internal erosion on dam and foundation, spillway, bottom outlet and hydropower systems. While genMR can also consider time-variant exposure and vulnerability, focus of this work is on multi-hazard correlation only. For work on damage-dependent vulnerability, the reader should refer to STREST WP4.

.

---

2 Generic Multi-Risk (GenMR) Framework

2.1 METHOD

2.1.1 Sequential Monte Carlo method

The generic multi-risk (genMR) framework (Mignan et al., 2014) is based on the sequential Monte Carlo method (MCM) and on a variant of a Markov chain. Figure 2.1 illustrates its principle. GenMR generates simulation sets S composed of N_{sim} simulations, with each simulation a time series defined over the interval $[t_0, t_{max}]$. Events are sampled from a Poisson distribution (homogeneous or non-homogeneous process) and are defined in a stochastic event set with long-term frequency of occurrence λ and various hazard/risk characteristics (see subsection 2.2). Figure 2.1a shows two examples of simulation sets, S_0 (with no interactions) and S_1 (with hazard interactions). In the first case, events are drawn from a Poisson distribution. In the second case, the probability of occurrence of each event is conditional on the occurrence of previous events, corresponding to a non-stationary Poisson process. Conditional probabilities are listed in a transition matrix, called *hazard correlation matrix* (HCM) and shown in Figure 2.1b. It is an n-square matrix with n the number of events. Rows represent trigger events and columns, the target/potentially triggered events. Here the notation P_i indicates event i of peril P. Each cell of the square matrix indicates the 1-to-1 conditional probability $\Pr(j|i) = \Pr(P_j|P_i)$ over $[t, t_{max}]$. The n-to-1 conditional probability is also considered by incorporating a memory element to the HCM (different from a strict memory-less Markov chain). Based on the defined correlations, chains of events can emerge in set S_1. The complete algorithm is given in Mignan et al. (2014).

.

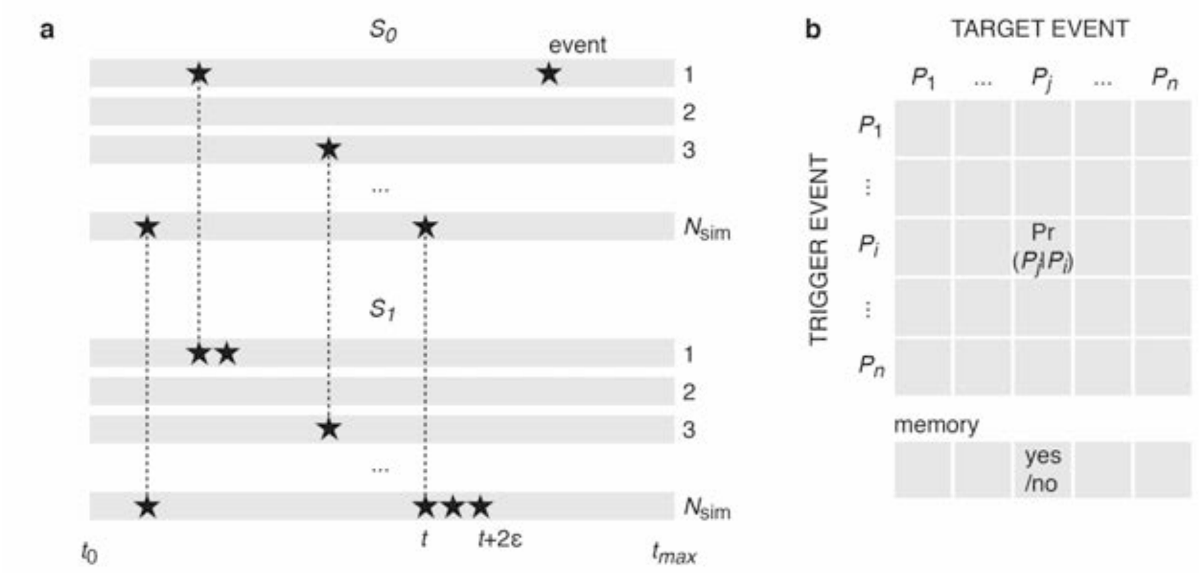

Fig. 2.1 The generic multi-risk (genMR) framework (Mignan et al., 2014)

The proposed approach is flexible enough that it should be able to include any type of hazard interaction, whatever the underlying physical process or modelling procedure. This is tested in the present report (see Sections 4 and 5).

2.1.2 Multi-hazard terminology

Based on the framework described above, Mignan et al. (2014) proposed a terminology for multi-hazard, which is as follows:

- Event repeat: $P_i \rightarrow P_i$ with P a given peril;
- Intra-hazard interaction: $P_i \rightarrow P_j$ with $i \neq j$ and P a given peril;
- Inter-hazard interaction: $A_i \rightarrow B_j$, with A and B different perils;
- Primary peril: $\lambda_A > 0$, with λ the long-term occurrence rate;
- Secondary peril: $\lambda_B = 0$ and $\Pr(B|A) > 0$;
- Invisible event: $\Lambda_i = 0$, $\Pr(j|i) > 0$ and Λ_j, with Λ the event loss and i the invisible event.

These terms are used consistently throughout this report.

2.2 PROOF-OF-CONCEPT

In a first phase, generic data and processes were generated by following the heuristic method and by abstracting the concepts of peril, peril characterization and interacting processes into basic characterizations and categorizations. This approach provides some general guidelines for cascade event quantification (with focus on low-probability–high-consequences LP-HC events) and a synthetic dataset for testing the genMR framework. What is described below follows the existing recommendations on extreme event assessment (Bier et al., 1999; Kameda, 2012; Paté-Cornell, 2012) by combining inductive generalization and reasoned imagination to include known examples of extremes as well as potential “surprise” events in a same framework. Subsection 2.2.1 presents the basic concepts of multi-risk described by Mignan et al. (2014) and subsection 2.2.2 presents the concept of Virtual City, to move from abstract concepts to a simplified reality (Komendantova et al., 2014; Mignan et al., in prep.). They represent the two first steps of the proposed top-down approach to multi-risk (Fig. 1.1) and provide the blueprint for the site-specific applications described later on.

2.2.1 Abstraction of perils and hazard interactions

Mignan et al. (2014) defined a stochastic event set made of two primary perils *A* and *B* (representative of earthquakes, volcanic eruptions, *etc.*) and three secondary perils *C*, *D* and *E* (tsunamis, industrial accidents, *etc.*). For perils A and B, the frequency-size distribution of events is defined by the exponential law

$$\lambda_i = \exp(-\beta \iota_i) \tag{2.1}$$

where ι_i is the hazard intensity, λ_i the long-term occurrence rate and β the exponential law exponent. The mean damage ratio δ_i is then approximated by the cumulative lognormal distribution

$$\delta_i = \frac{1}{2} erfc\left(-\frac{\ln(\iota_i) - \mu}{\sigma\sqrt{2}} \right) \tag{2.2}$$

where μ and σ are respectively the mean and standard deviation of the variable's logarithm and depend on the peril and asset response type. Note that 0 (no damage) $\leq \delta \leq 1$ (total destruction). Since a comparison of hazards would require a rather subjective intensity classification scheme (Kappes et al., 2012), Mignan et al. (2014) proposed to remove the hazard intensity ι by combining Eqs. 2.1 and 2.2 such that

$$\delta_i = \frac{1}{2} erfc\left(-\frac{\ln(-\ln(\lambda_i)) - \ln(\beta) - \mu}{\sigma\sqrt{2}} \right) \tag{2.3}$$

making each stochastic event defined only by its long-term occurrence rate and potential damage. The different parameters (β, μ, σ) are defined such that peril A dominates risk at short return periods and peril B at long return periods. Eqs. 2.1, 2.2 and 2.3 are represented in Figure 2.2. For each primary peril, 31 events are defined in the range $10^{-4} \leq \lambda \leq 10^{-1}$. For each secondary peril, 3 events are defined characterizing low, medium and high damage (i.e., $\delta_1 = 0.01$, $\delta_2 = 0.1$ and $\delta_3 = 1$).

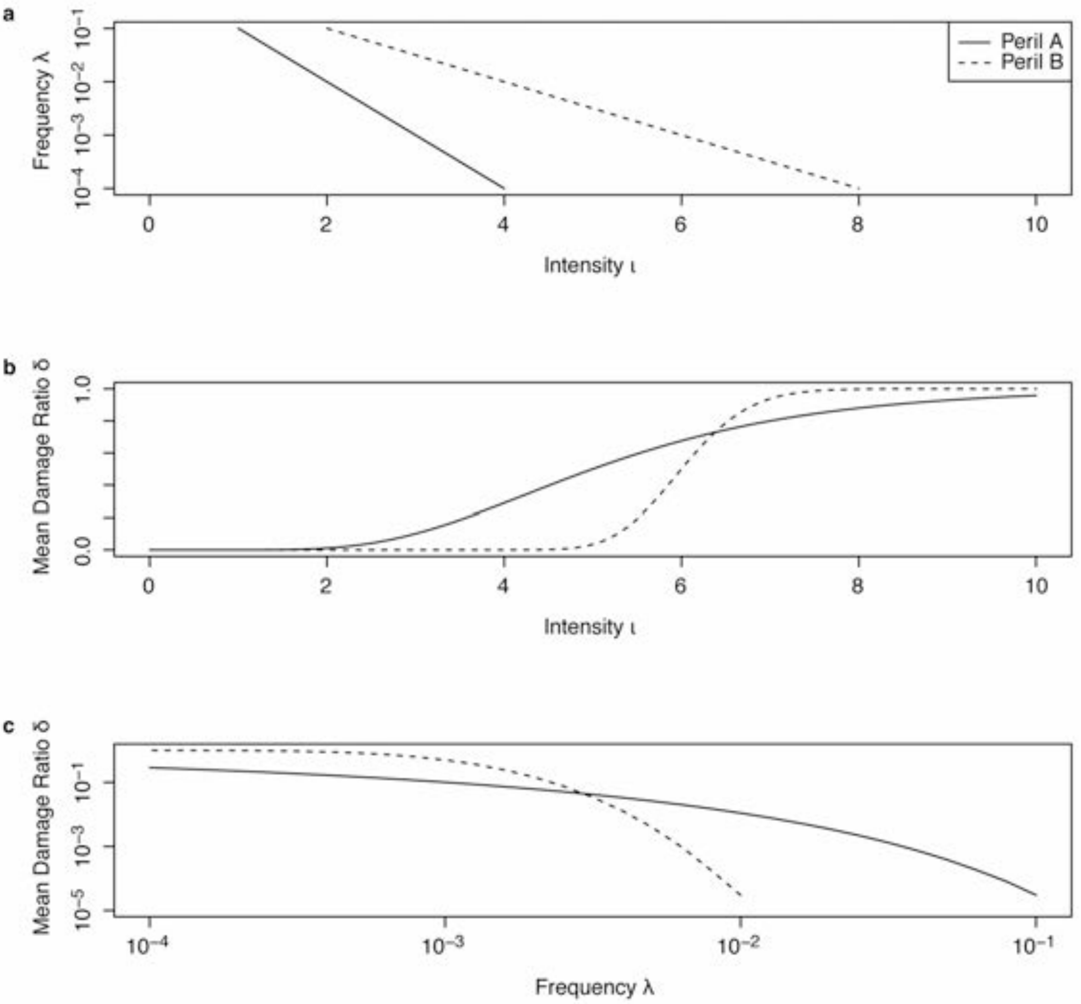

Fig. 2.2 Characterization of generic primary perils (Mignan et al., 2014)

Hazard interactions are then defined for a given configuration of the HCM, as shown in Figure 2.3. The proposed configuration includes different types of interactions (event repeat, intra- and inter-hazard interactions, possibility for multiple cascading effects), different aspects of memory (Yes/No) and different probability changes (forced to zero, increase/decrease, increase only). Analogies to real hazard correlations are given in Mignan et al. (2014). Event repeats are defined by the lognormal distribution

$$\Pr(A_i \mid A_i) = \int_{t_0}^{t_{\max}} \frac{1}{t\sqrt{2\pi\alpha_i^2}} \exp\left(-\frac{(\ln(t)-1/\lambda_i)^2}{2\alpha_i^2}\right) dt \qquad (2.4)$$

with the shape α_i fixed to 1. It means that the greater the size of an event (i.e., the lower its long-term rate), the less likely it is to occur again on the time period considered. Intra- and inter-hazard interactions between primary perils are defined by a process of time advance or time delay ("clock change") with

$$\Pr(j \mid i) = 1 - \exp(-\lambda_{j,mem}\Delta t) \quad \text{for } i \neq j \qquad (2.5)$$

based on the non-homogeneous Poisson process with *i* the trigger event, *j* the target event and

$$\lambda_{j,mem(updated)} = \frac{1}{1/\lambda_{j,mem} + \Delta T_{ij}} \quad (2.6)$$

$\Delta T_{ij} > 0$ represents a time delay in Eq. 2.6. $\lambda_{j,mem}$ is updated after each event occurrence j, including the case $i = j$, and represents the memory of the process (with $\lambda_{j,mem} = \lambda_j$ at t_0). For an analysis at the conceptual level, Mignan et al. (2014) defined $\Delta T_{ij} = \pm f/\lambda_i$ with f an ad-hoc coupling factor, such that the time shift due to event i is proportional to the return period of this event (i.e., a rare large event will have a greater impact than a small, more common, event). The sign of ΔT_{ij} (time advance or delay) was fixed randomly. This type of interaction ("clock change") is investigated in Section 4 for earthquake clustering where physical constraints are used based on the theory of Coulomb stress transfer. Finally, secondary perils – in Mignan et al. (2014) – occur based on the following one-way causal effects: $A \rightarrow C$, $C \rightarrow D$ and $D \rightarrow E$ (Fig. 2.3) with possibility for the domino effect $A \rightarrow C \rightarrow D \rightarrow E$. Mignan et al. (2014) considered a linear relationship between trigger event i and target event j such that

$$j(i) = \frac{n_j - 1}{n_i - 1}(i-1) + 1 \quad (2.7)$$

where n_i and n_j are the number of stochastic events i and j, respectively. Figure 2.4a illustrates the principle that for any event i in the range $[1, n_i]$, there is an associated event j in the range $[1, n_j]$. The conditional probability $\Pr(j|i)$ is then determined from the Binomial distribution

$$\Pr(k \mid i) = \frac{n_j!}{k!(n_j - k)!}\left(\frac{j(i)}{n_j}\right)^k \left(1 - \frac{j(i)}{n_j}\right)^{n_j - k} \quad (2.8)$$

where $0 \leq k \leq n_j$. $k = j$ except for the case $k = 0$, which corresponds to the probability of having no event triggered $\Pr(\emptyset|i)$ (Fig. 2.4b). Note that the higher the trigger increment i is (i.e., proxy to hazard intensity), the greater is the probability of triggering a severe target event j, which is a direct consequence of Eq. 2.7.

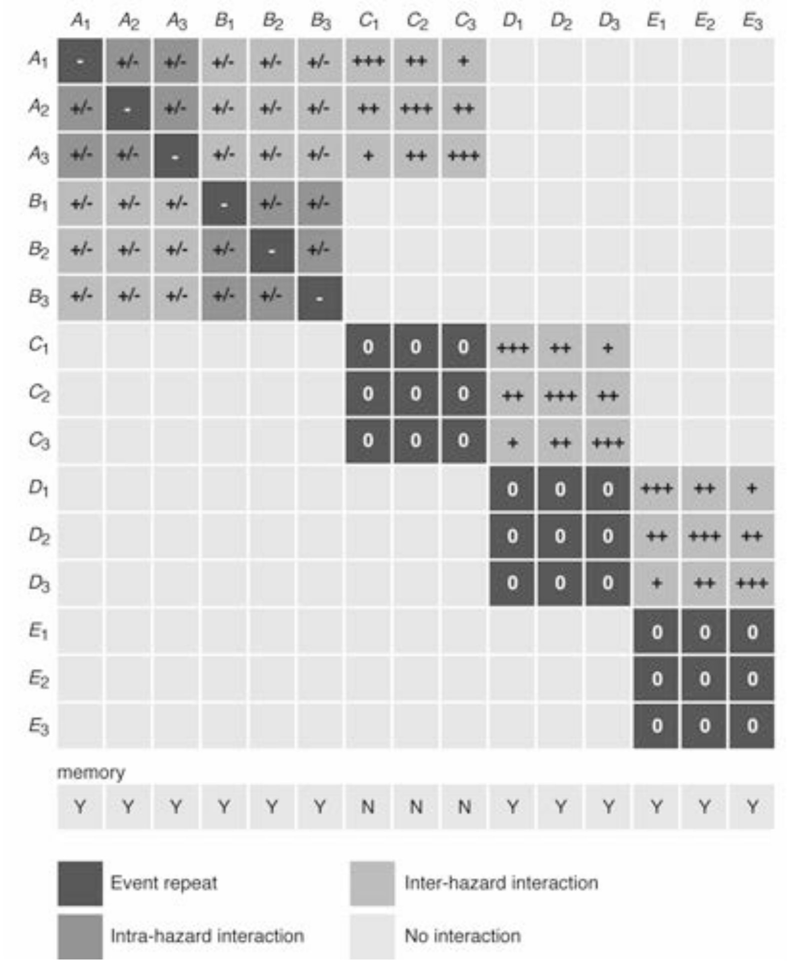

	A_1	A_2	A_3	B_1	B_2	B_3	C_1	C_2	C_3	D_1	D_2	D_3	E_1	E_2	E_3
A_1	-	+/-	+/-	+/-	+/-	+/-	+++	++	+						
A_2	+/-	-	+/-	+/-	+/-	+/-	++	+++	++						
A_3	+/-	+/-	-	+/-	+/-	+/-	+	++	+++						
B_1	+/-	+/-	+/-	-	+/-	+/-									
B_2	+/-	+/-	+/-	+/-	-	+/-									
B_3	+/-	+/-	+/-	+/-	+/-	-									
C_1							0	0	0	+++	++	+			
C_2							0	0	0	++	+++	++			
C_3							0	0	0	+	++	+++			
D_1										0	0	0	+++	++	+
D_2										0	0	0	++	+++	++
D_3										0	0	0	+	++	+++
E_1													0	0	0
E_2													0	0	0
E_3													0	0	0
memory	Y	Y	Y	Y	Y	Y	N	N	N	Y	Y	Y	Y	Y	Y

Event repeat
Inter-hazard interaction
Intra-hazard interaction
No interaction

Fig. 2.3 Example of hazard correlation matrix (HCM) (Mignan et al., 2014)

Based on the parameters defined above and on the different hypotheses listed in Table 2.1, Mignan et al. (2014) showed that multi-risk has two principal characteristics:

- Risk migration: When events from perils *A* and *B* interact with each other, the distribution of the size of chains of events shifts from Poisson to a Negative Binomial distribution, which is characteristic of a clustering behaviour. This is verified in Figure 2.5 where distributions are compared using the Akaike Information Criterion (AIC). It shows that risk migrates to lower-probability–higher-consequences when hazard interactions are considered.
- Risk amplification: The phenomenon of risk amplification is illustrated in Figure 2.6 where aggregated losses increase faster with larger initiating events. This increase is defined by a power law exponent, which increases when interactions are considered, in particular when secondary perils are introduced in the system (case $A \rightarrow C$, $C \rightarrow D$ and $D \rightarrow E$).

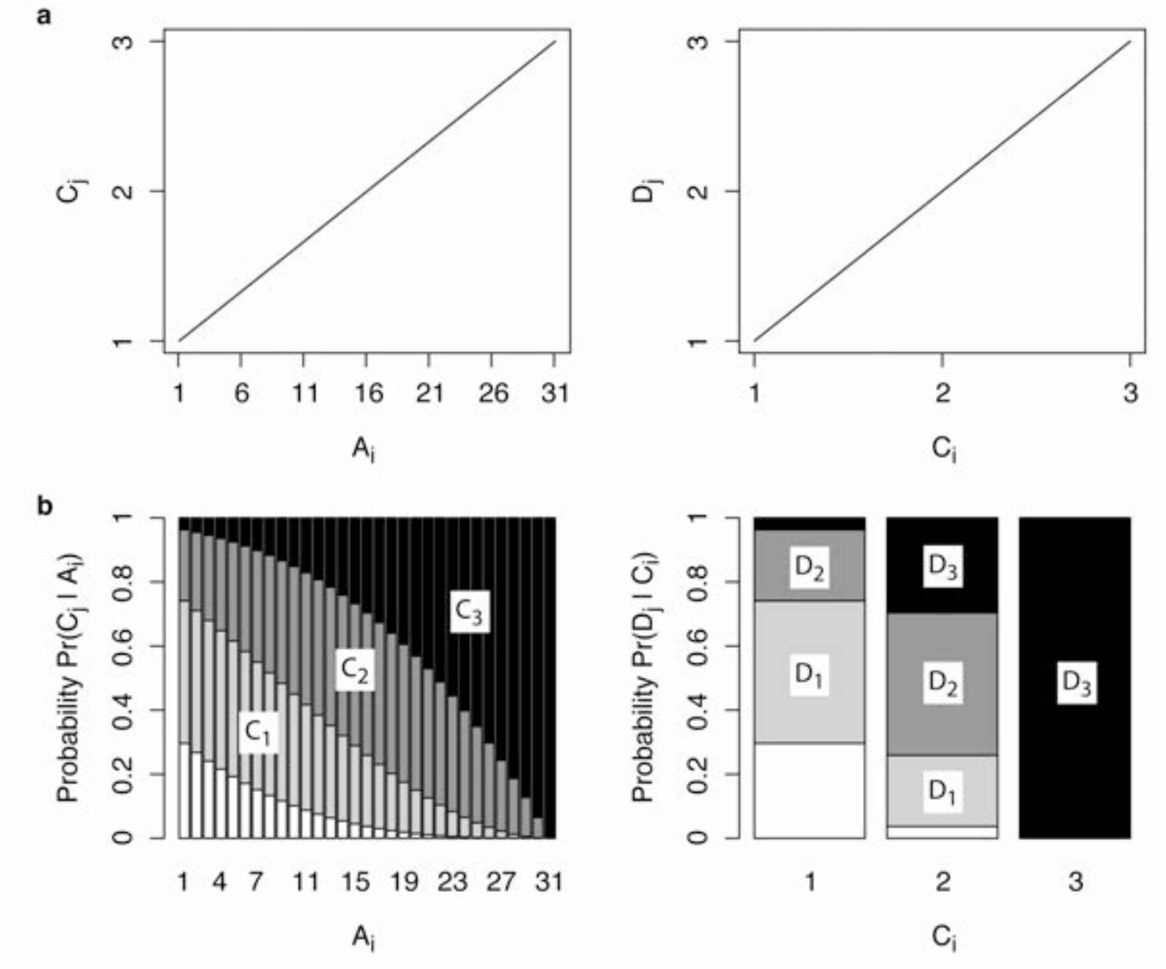

Fig. 2.4 Quantification of generic one-way causal effects (Mignan et al., 2014)

Table 2.1 Multi-risk hypotheses *H_i*

H_i	**Primary peril interactions**	**Secondary peril interactions**	**Time-variant vulnerability**	**Time-variant exposure**
H_0	✗	✗	✗	✗
H_1	✓	✗	✗	✗
H_2	✓	✗	✓	✗
H_3	✓	✓	✓	✗

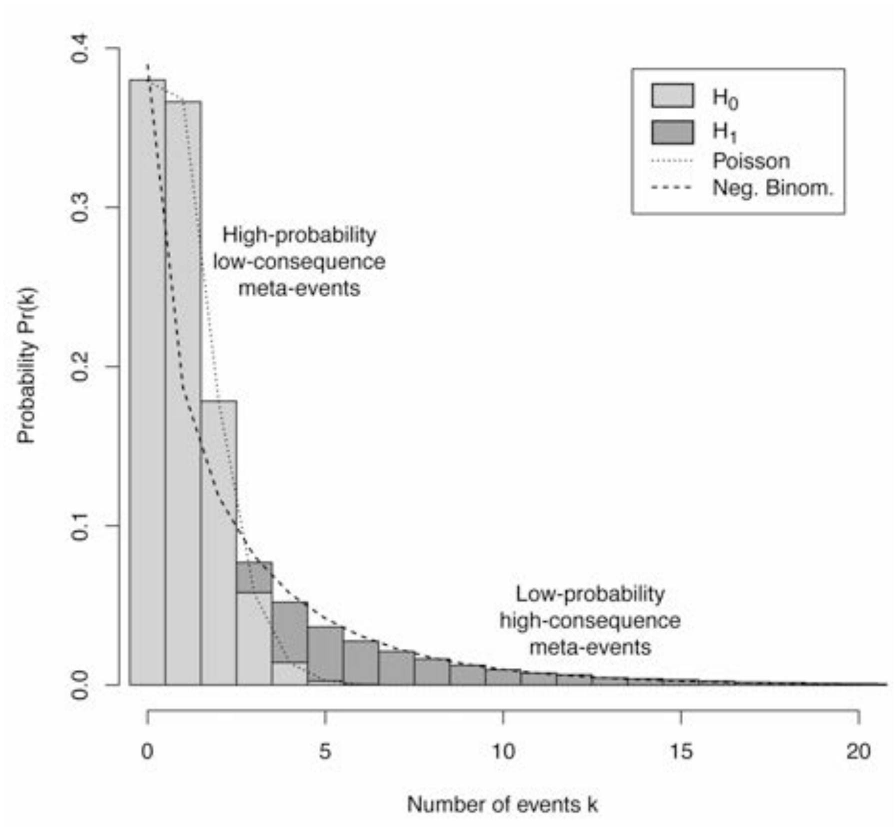

Fig. 2.5 Risk migration (Mignan et al., 2014)

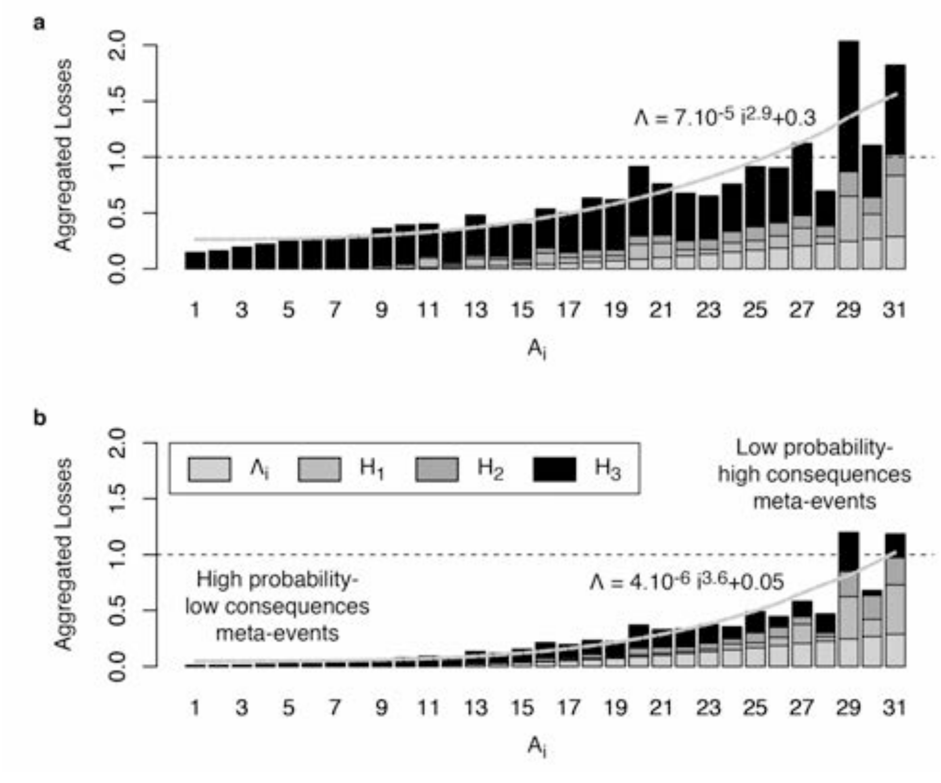

Fig. 2.6 Risk amplification (Mignan et al., 2014)

To represent multi-risk results, Mignan et al. (2014) (see also Komendantova et al., 2014) proposed a new multi-risk metric, referred to as the *risk migration matrix* (RMM). Based on the concept of risk matrix and in contrast with loss curves, this metric provides a more visual representation of the risk and of the impact of chains of events. Shown in Figure 2.7, the RMM is defined as the difference in the density of risk scenarios observed between two hypotheses. Risk scenarios are represented by dots (black for H_2 and white for H_1) and correspond to outputs from the simulation sets generated in genMR. To avoid a pixelated result, the densities are first calculated using a Gaussian kernel, large enough to focus on the first-order migration patterns. An increase in risk in a given frequency-loss domain is represented in red and a decrease in blue. The proposed approach permits to visualize how the risk migrates as a function of frequency and aggregated losses when new information is added to the system. The migration is particularly pronounced in the case of domino effects with $A \rightarrow C \rightarrow D \rightarrow E$. The RMM is tested in section 4.

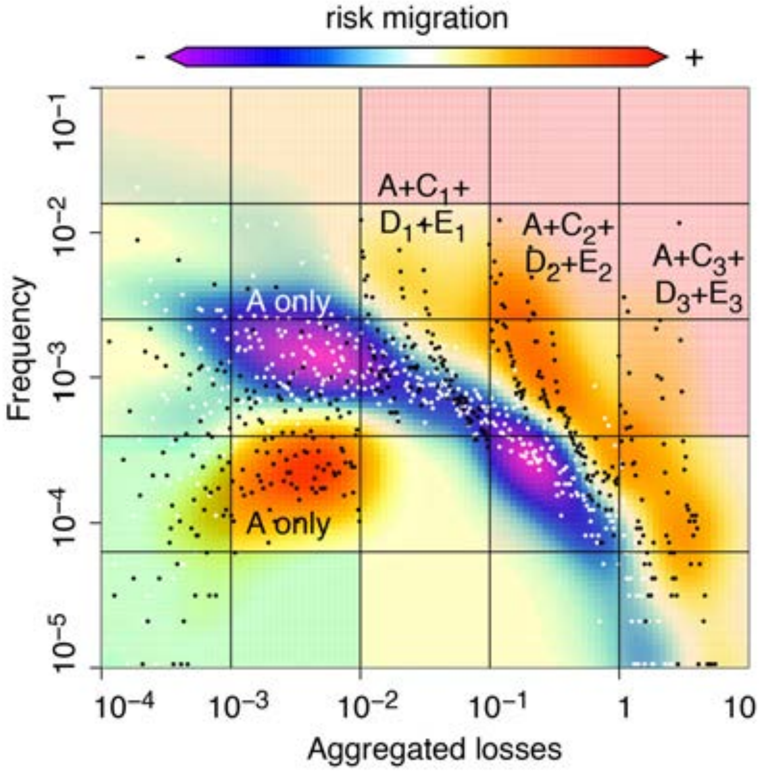

Fig. 2.7 Risk migration matrix (modified from Mignan et al., 2014)

2.2.2 Concept of Virtual City

To switch from abstract concepts to a simplified reality, the concept of Virtual City in a hazardous virtual region was proposed (Fig. 2.8; Komendantiva et al., 2014; Mignan et al., in prep.). It is a 100 by 100 km region where various geological and hydrological objects are defined: A volcano with an unstable slope in the north-eastern sector, faults in the north-western and central sectors, a river basin in the southern sector and a coast on the western side. Additionally, offshore faults are defined. Based on this configuration, various perils may occur, such as volcanic eruptions, landslides, earthquakes, fluvial floods, storms, sea submersion or asteroid impacts. Data (hazard, risk, interactions) are then defined using the heuristic approach, literature surveys and calibrations to real data. This approach is part of the top-down brick-by-brick approach described in Figure 1.1. Advantages are threefold: (i) In contrast with real sites, which have their own specific multi-risk aspects, the Virtual City is a playground where any multi-risk scenario can be defined (following reasoned imagination). Therefore a variety of scenarios can be tested as well as general aspects of multi-risk; (ii) The Virtual City is a controlled environment where sensitivity analyses can be made; (iii) In a top-down focus, the Virtual City can be used as a blueprint for real site experiments, thanks to a data switch, moving from generic relationships to site-specific ones. While epistemic uncertainties may remain high, use of the Virtual City permits to “fill in the gaps” and to run any multi-risk scenario where data are lacking.

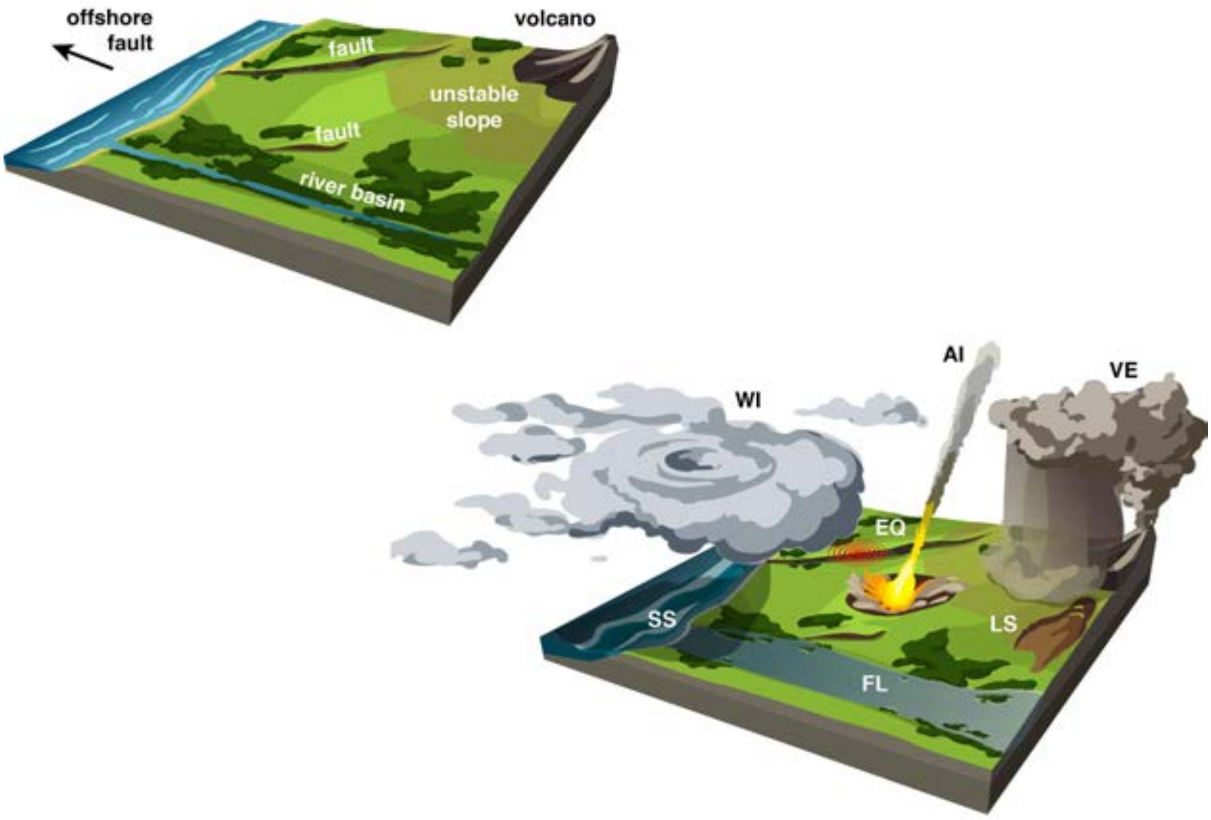

Fig. 2.8 Concept of Virtual City

2.3 APPLICATION TO REAL-WORLD CONDITIONS

In the scope of the STREST project, the genMR framework is tested for the first time in site-specific applications. Due to temporal and expertise constraints, work is limited to three test sites exemplifying three different types of hazard interactions:

- Intra-event interactions (Turkey): While not directly considered in genMR but of high interest for the STREST project, intra-earthquake triggering is a complementary process to earthquake interactions that should permit to better evaluate the maximum magnitude M_{max}. Concepts of dynamic stress transfer and fault propagation are used and tested in Turkey, where major hydrocarbon pipelines are located (CI-B1). A full description is given in Section 3;

- Intra-hazard interactions (northern Italy): Earthquake interactions are computed using the well-accepted Coulomb stress transfer theory. The method is ported to genMR and earthquake clustering quantified for faults located in northern Italy where critical industrial districts are located (CI-C1). A full description is given in Section 4;
- Inter-hazard interactions (Switzerland): A generic dam system (dam and foundation, spillway, bottom outlet, and hydropower system) and the main natural hazards that might affect it (earthquakes, floods and internal erosion) are defined as elements in the genMR framework. Characterisation of the different elements is based on empirical relationships. A full description is given in Section 5.

Testing of models developed in different fields of expertise shall provide the proof that the genMR framework is flexible enough to integrate a variety of multi-hazard models. Multi-risk aspects investigated in STREST WP4 and WP5 may also contribute to the testing/improvement of genMR.

3 Intra-Event Interactions: Intra-Earthquake Triggering (Inference on M_{max})

> "*It is the stress field during the dynamic rupture that loads the next fault segment and satisfies a rupture criterion that determines if a M6 earthquake cascades into a M8 earthquake*" – Harris et al. (1991)

The term "intra-earthquake triggering" was coined by Harris et al. (2002) to refer to dynamic stress transfer. If static stress transfer helps understanding and quantifying interactions between individual earthquakes that occur at different times (see Section 4), dynamic stress transfer is required to determine how a rupture propagates in the time lapse of one earthquake. The length of the rupture L_{max} then directly relates to the maximum magnitude M_{max} (all other parameters being kept the same). Such process is important to understand with M_{max} a critical parameter in probabilistic seismic hazard assessment (Cornell, 1968) and in stress tests (M_{max} what-if scenarios).

It should be noted that, while intra-earthquake triggering can be considered as a type of hazard interaction, it is not implemented in the generic multi-risk framework genMR (see Section 2), which considers interactions between events and not sub-events as input to the HCM. However events defined from intra-earthquake triggering (i.e., longer fault ruptures) could be defined as additional stochastic events (with a greater magnitude) in genMR.

A modified version of Section 3 has been published in a peer-reviewed journal (Mignan et al., in press, a): Mignan, A., L. Danciu and D. Giardini, "***Reassessment of the maximum fault rupture length of strike-slip earthquakes and inference on Mmax in the Anatolian Peninsula, Turkey***", Seismol. Res. Lett, in press (as of March 2015).

3.1 INTRODUCTION

It has become evident in recent years that probabilistic seismic hazard analyses and stress tests for critical infrastructures show limitations in the treatment of extreme events. These extreme events can be great earthquakes and/or their cascading effects, generally neither foreseen nor forecasted in most of the seismic hazard studies and stress tests for critical infrastructures. The 2011 Fukushima nuclear disaster – a consequence of the great Tohoku, Japan, earthquake – is the prime example of such model failure demonstrating the need for "a targeted reassessment of the safety margins" of critical infrastructures, particularly of nuclear power plants (ENSREG, 2011). A major error yielding the 2011 Fukushima nuclear disaster was the underestimation of the maximum magnitude (hereafter M_{max}) in the Japanese seismic hazard model in which the fault segment in the Tohoku region was attributed M_{max} = 7.6 while the 2011 earthquake ruptured several segments, reaching a magnitude M_w = 9.0 (e.g., Goto and Morikawa, 2012). The earthquake-triggered tsunami was thus greater than possibly expected, with an estimated maximum wave height of ~14 m, which was much larger than the 5.7 m seawall (ENSI, 2012; Lipscy et al., 2013).

The present study aims at tackling such issue, (1) by proposing criteria for earthquake rupture cascading over fault segments based on geometrical and physical considerations and (2) by assessing the M_{max} of these ruptures spanning over hundreds of kilometres. Focus is made on strike-slip mechanisms due to some conceptual limitations explained below. Different definitions of M_{max} have been proposed in the past, such as the maximum observed magnitude, the deterministic "maximum credible" magnitude (Reiter, 1990) and the statistical "maximum possible" magnitude (Kijko and Singh, 2011). The term "probable maximum" magnitude has also been proposed recently, which depends on the time period considered (Rong et al., 2014). All definitions except for the latter are based on the assumption that no earthquake is expected above that threshold. Our proposed method to compute M_{max} is directly related to the deterministic approach.

Earthquake ruptures are known to potentially propagate over several segments (e.g., Eberhart-Phillips et al., 2003; Fliss et al., 2005) and in the case of subduction zones to consequently be able to trigger greater tsunamis (e.g., Fujii and Satake, 2007). Yet fault segments are still modelled as individual faults in most regional seismic hazard models based on expert opinion and on limited paleoseismic data. Here we define a set of simple criteria to assess cascades from individual fault segments by using dynamic stress modelling assumptions (e.g., Kame et al., 2003) and field observations (e.g., Wesnousky, 2006). We apply these criteria to a subset of strike-slip faults in the Anatolian Peninsula (Basili et al., 2013), as defined within the 2013 released *European Seismic Hazard Model* (hereafter ESHM13). We estimate M_{max} for the resulting cascading events by use of empirical magnitude scaling relationships (Stirling et al., 2013 and references therein) taking into account saturation effects at long lengths and other physical constraints (Anderson et al., 1996).

3.2 METHOD & DATA

3.2.1 Appraisal of criteria for multi-segment rupture from the dynamic stress modelling literature

Three types of fault segment association can be defined based on geometrical configurations (Fig. 3.1): (1) bending or rupture propagation along the same fault via segments of potentially different strikes, (2) branching or rupture propagation switching from a segment to a branching segment via a triple junction (in this case, only part of the first segment ruptures), and (3) jumping or propagation from a source to another one, separated in space.

An examination of numerous surface rupture traces of historical strike-slip earthquakes by Wesnousky (2006) showed that ruptures stop propagating (jumping) if the dimension of the fault step Δ is above 3-4 km. For strike-slip faults in Turkey, Barka and Kadinsky-Cade (1988) had already remarked that ruptures generally do not jump step-overs that are wider than 5 km. Dynamic models confirm the importance of the size of the fault step in rupture arrest. Harris and Day (1993) showed that a strike-slip earthquake is unlikely to jump a fault step wider than 5 km, in agreement with field observations. This was confirmed in the case of the 1999 Izmit earthquake, which rupture was stopped by a narrower step-over at its eastern end (Harris et al., 2002). For a rupture to propagate over a wider step, linking structures such as transfer faults (*en echelon* structures) are necessary, as shown by Harris and Day (1999) in the case of the 1992 Landers earthquake. The most favourable side for bending/branching switches from the extensional to the compressional side as the angle Ψ between the direction of maximum compressive pre-stress and the fault strike becomes shallower. Propagation through bending or branching then depends on the fault geometry, i.e., the inclination φ of a segment with respect to another one (Poliakov et al., 2002; Kame et al., 2003). This has been verified in the case of the 2002 Denali branching earthquake (Bhat et al., 2004).

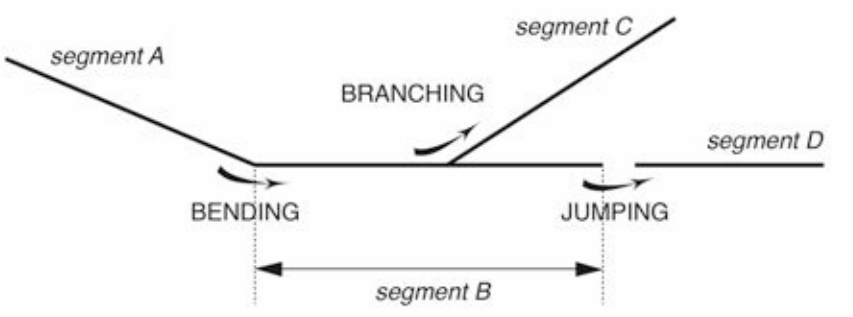

Fig. 3.1 Different types of fault segment association

Based on these two-dimensional geometrical constraints (no depth constraint), we propose the following criteria, which all have to be satisfied for a rupture to propagate along strike from a segment to another one (Fig. 3.2; see also algorithm in the Appendix, Subsection 3.5). The proposed rules are simplifications from the reality and may not represent the full spectrum of possible cascades (see next subsection on assumptions and limitations).

1. Compatibility of segments: Segments involved in a cascade must have the same mechanism (left- or right-lateral) and the same dip direction (i.e. not antithetic).
2. Maximum distance: The minimum distance Δ between two sources must be lower than 5 km (Harris and Day, 1993; Wesnousky, 2006).
3. Maximum strike difference: The relationship $\psi-\delta \leq \varphi \leq \psi+\delta$ must be respected with φ the angle between two segments (i.e. strike difference), $\psi = \gamma(45-\Psi-180\ \mathrm{atan}(\mu_d)/2\pi)$ the optimal angle for rupture (Poliakov et al., 2002; Kame et al., 2003; Bhat et al., 2004), $\Psi > 0$ the angle between the first segment and the direction of maximum compressive stress S_{max}, μ_d the dynamic friction coefficient, $\gamma = 1$ for right-lateral and $\gamma = -1$ for left-lateral, and $\delta = 30°$ the range of preferred orientation (see Fig. 3.2 for angle sign convention).
4. Relative position of segments: The rupture can propagate from all or part of a segment to all or part of another segment if the angle between the two subsequent segments remains obtuse (i.e., no backward branching/bending allowed).

Angle notation follows Kame et al. (2003). The term $\pi/2-\Psi-\mathrm{atan}(\mu_d)/2$ represents the optimum angle once the effect of dynamic friction μ_d is taken into account (Kame et al., 2003). The parameter δ represents the angle range where the shear stress is larger than the frictional resistance, with ±2δ = 90° the stressed quadrant. The angle Ψ between the fault segment and the direction of maximum compressive stress is defined as $\Psi = \Re/2+45°$ modulo 90°, assuming that variations in the rake $\Re$ represent the variations in the regional stress field orientation. The angle Ψ is defined such that there is no difference between right-lateral and left-lateral mechanisms. It is only the parameter γ that assigns the mechanism and therefore the main orientation of the stressed quadrant. Source orientations are calculated from their tips in disregard of track irregularity. We fix μ_d = 0.12 and δ = 30° following Kame et al. (2003). The δ value choice is also in agreement with Barka and Kadinsky-Cade (1988), who found that strike-slip ruptures in Turkey do not propagate past bends that have angles greater than about 30°.

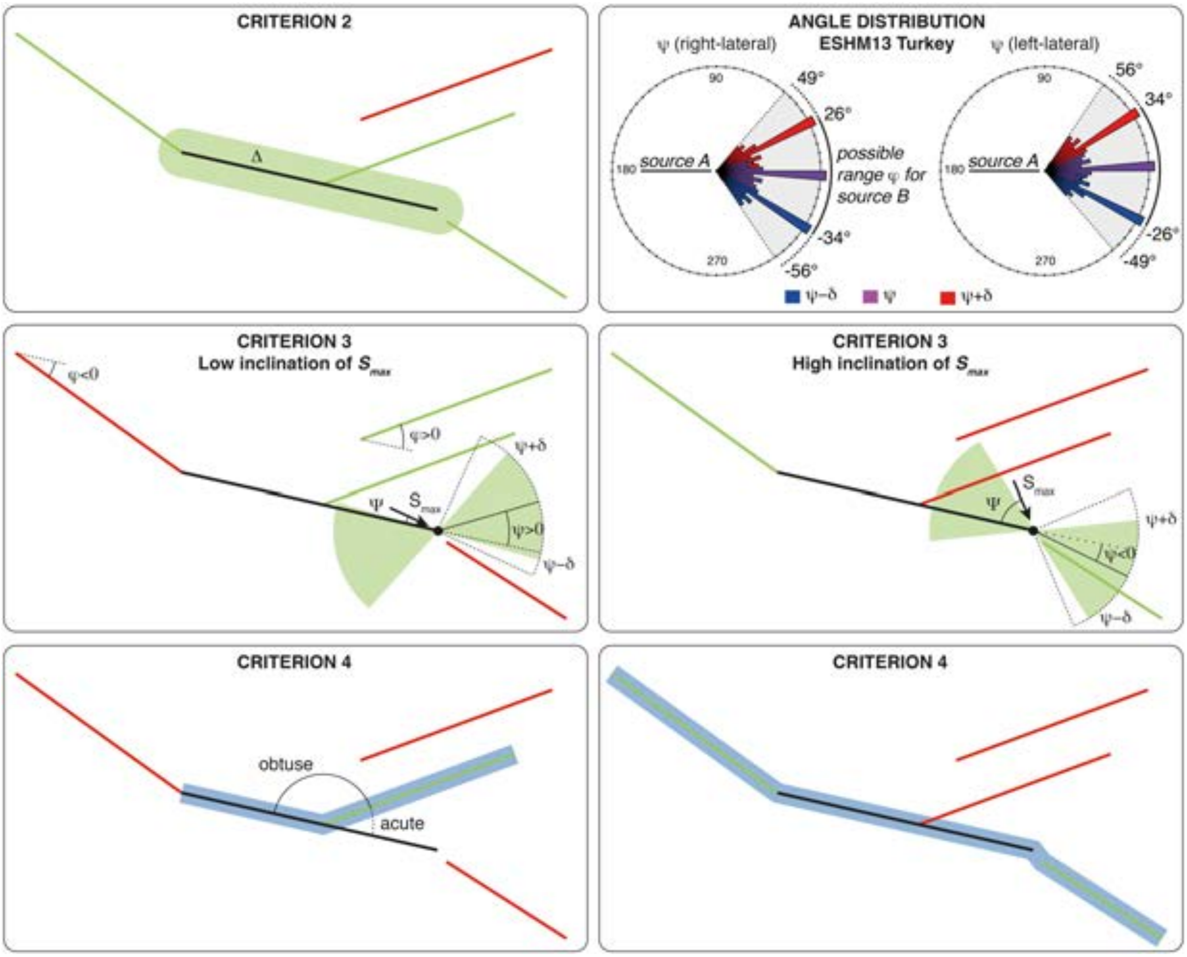
CRITERION 2
Δ
ANGLE DISTRIBUTION
ψ (right-lateral)
ESHM13 Turkey
ψ (left-lateral)
90
180
270
source A
49°
26°
-34°
-56°
possible range ψ for source B
56°
34°
-26°
-49°
ψ−δ
ψ
ψ+δ
CRITERION 3
Low inclination of S_{max}
ψ<0
ψ>0
ψ+δ
ψ
S_{max}
ψ>0
ψ−δ
CRITERION 3
High inclination of S_{max}
ψ
S_{max}
ψ+δ
ψ<0
ψ−δ
CRITERION 4
obtuse
acute
CRITERION 4

Fig. 3.2 Criteria for multi-segment rupture

3.2.2 Multi-segment rupture method assumptions and limitations

The proposed method for multi-segment rupture does not consider the case of dip-slip multi-segment rupture. As indicated by Magistrale and Day (1999), it may be misleading to apply results found for strike-slip systems to dip-slip ones since slip direction and strike directions are parallel in the former case and perpendicular in the second. While the same authors found that jumping between thrusts in dynamic stress simulations is limited to $\Delta \leq 2$ km (i.e., different criterion 2), we did not find information regarding the maximum orientation change allowed between two dip-slip segments (i.e., no criterion 3 defined for horizontal propagation of dip-slip ruptures so far). Similarly, criterion 1 enforces that two segments with left- and right-lateral mechanisms cannot rupture together in a same earthquake. Once again, this criterion is based on the fact that no such an association has been described in the literature on dynamic stress modelling.

Inclusion of “multifault ruptures” is a new feature of the latest version of the *Uniform California Earthquake Rupture Forecast* (hereafter UCERF3; Field et al., 2013; Milner et al., 2013) compared to the previously published UCERF2 version (Field et al., 2009). Generally, for strike-slip-dominant regimes, our method should satisfy seismic hazard modellers due to its simplicity. Otherwise, the UCERF3 method appears more flexible since it applies for any earthquake mechanism, but at the cost of some subjective choices (e.g., $|\varphi| \leq 60°$ proposed to only prevent large changes in rupture strike, such as right angles or U-turns). Nonetheless, both methods are independent procedures, which can be applied individually when one needs to estimate M_{max} (this study) or needs to model the floating ruptures and their associated rates in seismic hazard analyses (UCERF3).

Rupture velocity (hereafter V_r) is one of the three key parameters to consider in bending/branching scenarios (with the angles Ψ and φ discussed above). Stresses that could initiate rupture on a bend/branch have been shown to significantly increase with crack speed (Poliakov et al., 2002). However, some earthquakes have been observed to propagate very slowly and others very fast (e.g., Bhat et al., 2007 – see also the concept of supershear earthquakes in Rosakis et al., 1999). Such uncertainty on the process is overcome in our approach by implicitly assuming a reasonably high V_r (close to the elastic wave speed level), which implies that propagation from a fault segment to another one depends only on the segment orientation, thus yielding a conservative M_{max}.

Whether a rupture can continue on a larger scale also depends on the history of the stress field in the area (e.g., Poliakov et al., 2002). It has also been recognized that the pre-stress conditions play an important role for a given offset to be breached (Harris and Day, 1999). We assume that the stress field conditions are always favourable for rupture propagation to obtain a conservative estimate of M_{max}. This assumption avoids including a time-variant component that depends on the earthquake history in the considered region (King et al., 1994).

A last limitation is the sensitivity of the results to the spatial resolution of the fault dataset considered as input for the M_{max} analysis. This is investigated in detail in the next section.

3.2.3 The ESHM13 database

The ESHM13 (Giardini et al., 2013) represents the latest seismic hazard model for the European-Mediterranean region. The model combines the up-to-date information about earthquakes, active faults and crustal deformation, including the quantification of model and data inherent uncertainties for Europe and Turkey without the limits of national borders. Since the method proposed in the present article is limited to strike-slip mechanisms, we focus our analysis to the Anatolian Peninsula where strike-slip structures are predominant and have the potential to rupture over great distances.

We use the fault sources as defined in ESHM13 and described in the European Database of Seismogenic Faults (available at http://diss.rm.ingv.it/share-edsf/, last assessed September 2014). The seismically active faults, as defined by Basili et al. (2013), represent a composite structure that consists of multiple single mapped faults. By this definition, the size of a composite seismogenic source spans a larger area than the one of the largest observed earthquake due to high uncertainties on the end-points of the defined segments. The end-points were defined either at the end of an adjacent identified fault rupture or at a significant structural change (Haller and Basili, 2011).

Figure 3.3 shows a map of the region including the fault mechanisms derived from the source rake $\Re$ (see inset for rake/mechanism convention in ESHM13). We only consider strike-slip faults for our analysis, with $\Re \leq 45^\circ$ or $\Re \geq 315^\circ$ for left-lateral faults and $135^\circ \leq \Re \leq 225^\circ$ for right-lateral faults. Since ESHM13 only provides minimum and maximum values of the rake, we use $\Re = (\Re_{min}+\Re_{max})/2$. Arithmetic mean values are also used for other ESHM13 parameters (strike, dip and slip rate).

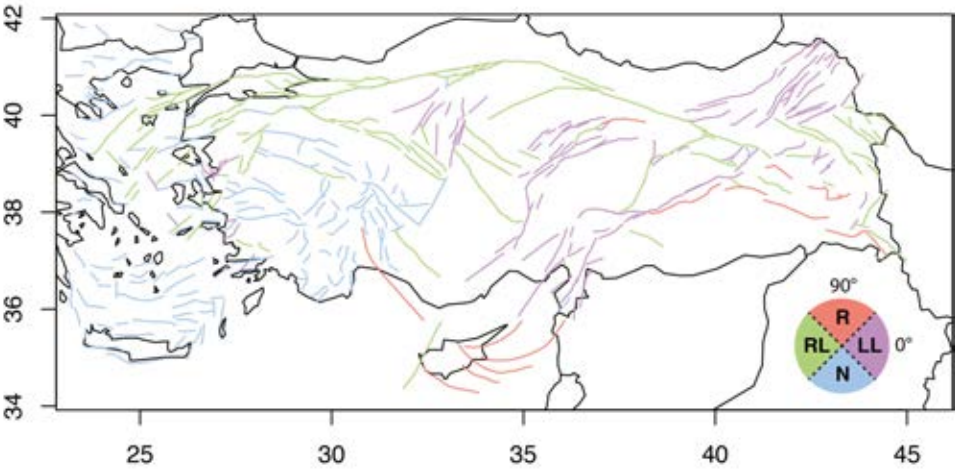

Fig. 3.3 ESHM13 fault map of the Anatolian Peninsula

3.2.4 Assessment of M_{max} considering individual fault segment lengths or cascade lengths

M_{max} is commonly estimated from the length L of individual fault segments. We first investigate the scaling relationships listed in Table 3.1 (Wells and Coppersmith, 1994; Mai and Beroza, 2000; Hanks and Bakun, 2002; Leonard, 2010; Wesnousky, 2008), used in ESHM13 and/or recommended by Stirling et al. (2013) for the case of “plate boundary crustal, fast plate boundary faults, strike-slip dominated” (their tectonic regime A11). Figure 3.4 compares these relationships to the ESHM13 data here defined by M_{max}, the total subsurface length L_{tot} and the effective subsurface length L_{eff}. L_{tot} is the total subsurface length spanning the entire composite source, geographically defined (i.e., the “trace length in map view” definition of Kim and Sanderson, 2005). It is not directly linked to the assigned M_{max} but represents possible extensions of the individual fault ruptures, due to uncertainty in their location. L_{eff} is linked to M_{max} in ESHM13 via the empirical magnitude-length scaling relationships mentioned above. Only in ~20% of cases is L_{eff} less than 80% of L_{tot}, corresponding to corrections to account for low slip rates. In the purpose of our study, we only use L_{tot} while correcting for slip rates at a later stage. In ESHM13, the minimum, median and maximum lengths of fault segments are 17 km, 50 km and 360 km, respectively (Fig. 3.4a). For the longest length, the corresponding M_{max} equals 8.1 in ESHM13 (composite source case).

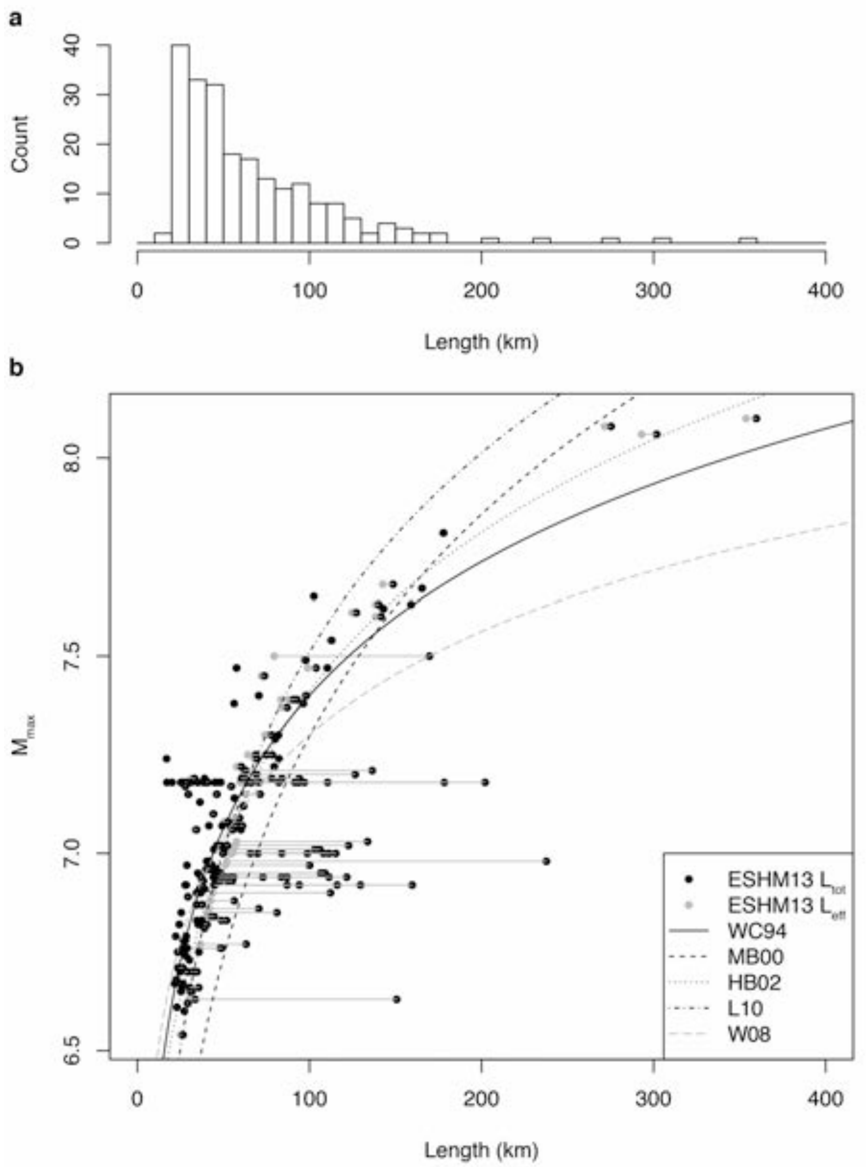

Fig. 3.4 ESHM13 length-M_{max} relationships (strike-slip, Anatolian Peninsula)

In the case of rupture cascades, the resulting rupture length can easily reach several hundreds of kilometres long, which in turn exceeds the calibration range of the length-magnitude scaling equations. In this view, we dismiss the equations proposed by Mai and Beroza (2000) (estimated L_{max} = 180 km) and by Leonard (2010) (estimated L_{max} = 50 km for strike-slip ruptures). We also do not use the relationship by Wells and Coppersmith (1994) since Hanks and Beroza (2002) include their dataset while adding five more strike-slip ruptures above 200 km long. Following Stirling et al. (2013), the two remaining relationships (Hanks and Bakun, 2002; Wesnousky, 2008) apply up to M_w = 8 (L_{max} ~ 430 km in both cases).

Since empirical magnitude-length scaling equations are not well constrained at very high length values, physical constraints are also considered. We investigate the role of slip rate (s) on M_{max} by using the scaling equation of Anderson et al. (1996) (Table 3.1) even if this additional empirical relationship is also poorly constrained for very long lengths (L_{max} = 470 km).

Table 3.1 Length-magnitude scaling relationships (1: ESHM13, 2: Stirling et al. (2013), 3: present study)

Reference	Relationship*	Parameters (± standard error)	1	2	3
Wells and Coppersmith (1994)	$M_w = a \log(L) + b$	$a = 1.12$ (±0.13); $b = 5.16$ (±0.08)	✓		
Mai and Beroza (2000)	$M_w = 0.67 ((\log(L) - a) / b + 7) – 10.7$	a = -5.15 (±1.11); b = 0.36 (±0.06)	✓		
Hanks and Bakun (2002)	$M_w = a \log(A) + b$	{ A ≤ 537 km^2: $a = 1$; $b = 3.98$ (±0.03) }; { A > 537 km^2: $a = 4/3$; $b = 3.07$ (±0.04) }	✓	✓	✓
Leonard (2010)	$M_w = a \log(L) + b$	$a = 1.67$; $b = 4.24$	✓	✓	
Wesnousky (2008)	$M_w = a \log(L) + b$	$a = 0.87$; $b = 5.56$; M_w±0.24		✓	✓
Anderson et al. (1996)	$M_w = A + B \log L - C \log s$	$A = 5.12$ (±0.12); $B = 1.16$ (±0.07); $C = 0.20$ (±0.04)			✓

3.3 RESULTS

3.3.1 Strike-slip cascades in the Anatolian Peninsula

For the dataset considered, the algorithm for multi-segment rupture (see Appendix) produces a total of 272 cascades (including some redundancies). Figure 3.5a shows an example of cascade on the North Anatolian Fault (NAF), which is composed of seven ESHM13 fault segments, complete or partial. Figure 3.5b shows the longest rupture cascades possible in different parts of the Anatolian Peninsula based on the data and method employed (with $\Delta = 5$ km fixed), each colour representing one distinct cascade.

It should be noted that these results are sensitive to the definition of the fault network trace and to the values of Δ and δ. While the defined mean orientation of a fault segment is likely accurate, the gap between different segments depends on the spatial resolution of the fault mapping, indicating the importance of improved fault mapping in seismic hazard studies, especially considering the link between the different structures in three dimensions (e.g., slip-partitioning and complex *decollements*) (e.g., Choi et al., 2012). Ambraseys (1970) noted that the Anatolian fault zone appears at a small scale as a continuous structure except for the step near Niksar (Fig. 3.5b). This step explains why no rupture cascades along the full NAF structure when using the ESHM13 database and $\Delta = 5$ km. However *en echelon* structures link the two fault segments at a larger scale, which suggests possible jumping between the eastern and western sides of the NAF when refined information is used.

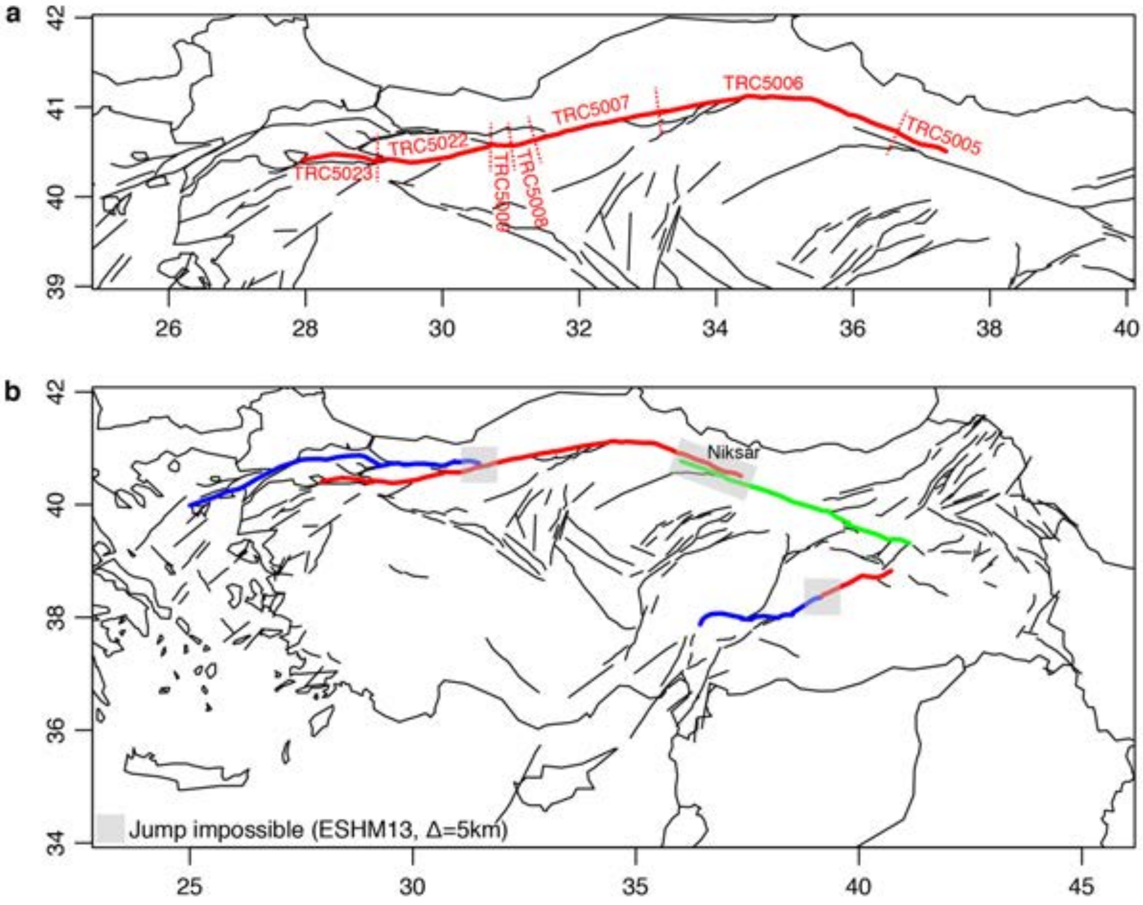

Fig. 3.5 Examples of generated strike-slip cascades

While we consider that the values Δ = 5 km and δ = 30° fixed in the criteria defined above are reliable physical constraints, verified in both dynamic models (Harris and Day, 1993; Kame et al., 2003; Harris et al., 2002) and in the field (Wesnousky, 2006; Barka and Kadinsky-Cade, 1988), Δ may need some adjustment in order to take into account obvious inconsistencies in the fault input dataset. This is investigated in the next subsection with the mapping of M_{max}.

It should be added that the rupture cascades generated cannot be compared to historical complex ruptures, since some of the ESHM13 sources are already defined from these events explaining why some individual sources are bended (e.g., ESHM13 stochastic versions of the 1939 Ercincan, 1943 Ladik and 1999 Izmit earthquakes, which all present bends – Ambraseys, 1970; Harris et al., 2002). In other words, all the cascades generated here are potential ruptures that have not yet been observed.

3.3.2 Reassessment of M_{max} considering rupture cascade lengths in the Anatolian Peninsula

Figure 3.6a shows the distribution of rupture cascade lengths with minimum, median and maximum lengths of 33 km, 254 km and 853 km, respectively for the “standard” Δ = 5 km. For an increased Δ = 10 km, the median and maximum lengths increase to 436 km and 1480 km, respectively. It means – following the proposed method – that events could rupture over more than twice the length of the longest fault defined in ESHM13 when considering the standard input parameters (Δ = 5 km, δ = 30°) but that they could rupture over more that four times the ESHM13 maximum length if Δ is doubled. Figure 3.6b shows new estimates of M_{max} based on rupture cascade length using the scaling relationships of Hanks and Bakun (2002) and of Wesnousky (2008). We additionally investigate the role of the slip rate (s) on M_{max} by defining the slip rate of cascades $s_{casc} = \sum s_{seg}/n_{seg}$ with n_{seg} the number of ESHM13 segments of slip rate s_{seg}. We then test the equation of Anderson et al. (1996) (Table 3.1) and find values comprised between the Hanks and Bakun (2002) and Wesnousky (2008) estimates with M_{max} = 8.3±0.3 for L_{max}(Δ = 5 km) = 853 km and M_{max} = 8.5±0.3 for L_{max}(Δ = 10 km) = 1480 km (Fig. 3.6b).

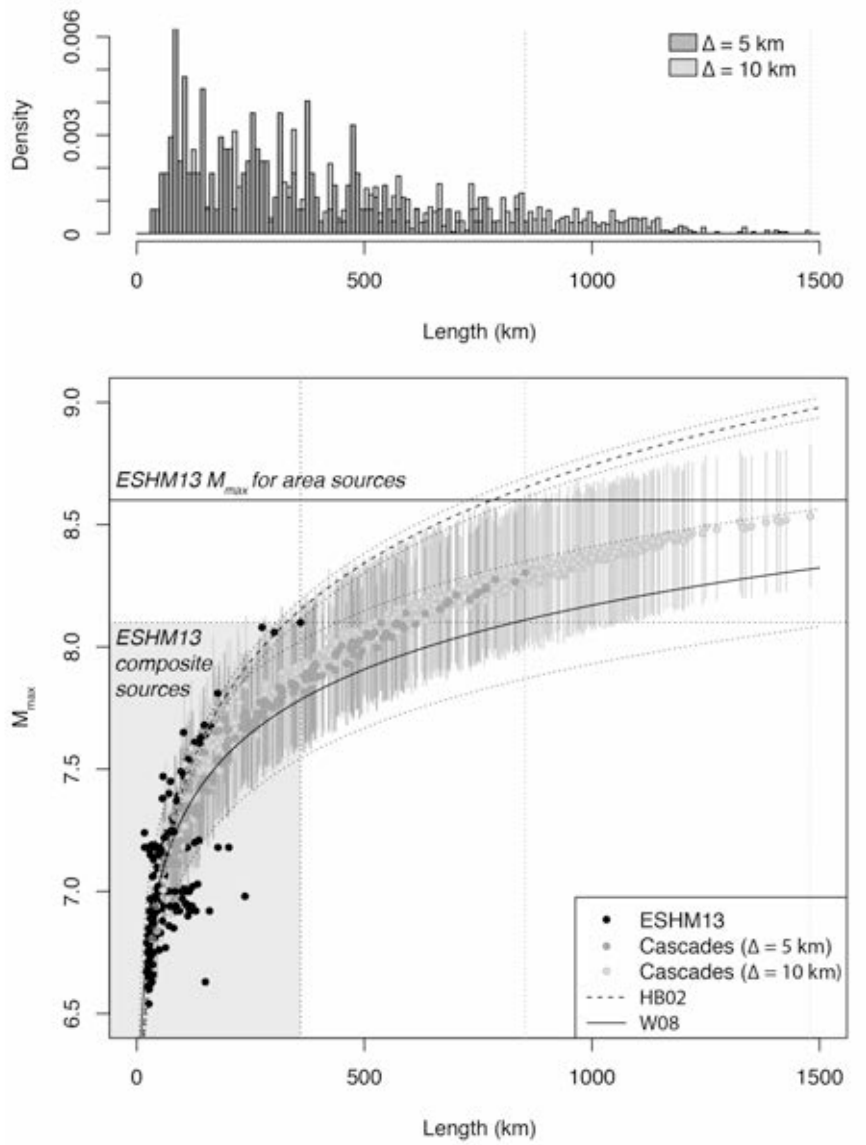

Fig. 3.6 Length-M_{max} scaling for cascades (strike-slip, Anatolian Peninsula)

Figure 3.7 shows M_{max} maps of the strike-slip faults in the Anatolian Peninsula for ESHM13 segments (Fig. 3.7a) and for multi-segment cascades with standard Δ = 5 km (Fig. 3.7b) and increased Δ = 10 km (Fig. 3.7c). M_{max} is here computed for all maps as the mean of the M_{max} values obtained from the Hanks and Bakun (2002) and Wesnousky (2008) relationships. As already discussed earlier, an earthquake cannot rupture all along the NAF when using the standard Δ = 5 km (see Fig. 3.5b). It is only with Δ = 10 km that the NAF can rupture in one event. Assuming that Δ = 5 km is reliable, this result indicates that surface geology is insufficient. This is easily argued in the case of plate boundaries (e.g., NAF), which by definition have to be continuous. In the present case, it is reasonable to use an increased Δ = 10 km to reproduce the plate boundaries as continuous structures (Fig. 3.7c). This is in agreement with field observations on the NAF (e.g., Barka and Kadinsky-Cade, 1988).

We find that M_{max} is increased locally from about 0.5 to 1.5 units along the NAF and the East Anatolian Fault (EAF). A number of other faults show an increase from about 0.5 to 1.0 (Figs. 3.7a-c). These results are subject to epistemic uncertainties. With longer ruptures being characterized by greater slip and a wider shaking spatial footprint, our results indicate a possible change in hazard in the Anatolian Peninsula once cascades are considered. On the other hand, the maximum M_{max} obtained in the present study (max(M_{max}) = 8.5±0.3) is close to M_{max} = 8.6 for the NAF area source of ESHM13 (Basili et al., 2010). The area source M_{max} is assigned as the largest value between the historical observations and largest maximum magnitude as estimated from fault sources, plus an increment of 0.2 corresponding to the reported magnitude error on the earthquake catalogue (Meletti et al., 2009). It is well known that the M_{max} of strike-slip events are unlikely to reach M_w 9 values since great strike-slip ruptures scale with length L and not area L^2 (e.g., Romanowicz and Ruff, 2002). The 2012 equatorial Indian Ocean earthquakes of M_w 8.6 (mainshock) and 8.2 (aftershock) were two of the largest strike-slip earthquakes ever recorded (Duputel et al., 2012).

3.4 IMPLICATIONS FOR STRESS TESTS

A stress test is defined as a targeted assessment of the safety margins of a given critical infrastructure. This assessment consists in particular in the evaluation of the response of the critical infrastructure when facing a set of extreme situations (ENSREG, 2011) (see also STREST WP5). In this context, we are interested in generating the “worst” earthquake magnitude that is physically possible. Seismic hazard analyses must also define the largest earthquake possible within a specified source zone or known fault. The probabilistic approach describes the maximum possible earthquake magnitude, whereas the deterministic approach describes the maximum credible earthquake magnitude. The maximum possible magnitude is estimated from geological features (active faults), historical and instrumental earthquake observations, tectonic settings and physical principles (Wheeler, 2009). The maximum credible magnitude is generally defined as a function of the longest known fault system and generally does not imply occurrence of this earthquake during any lifetime (Reiter, 1990).

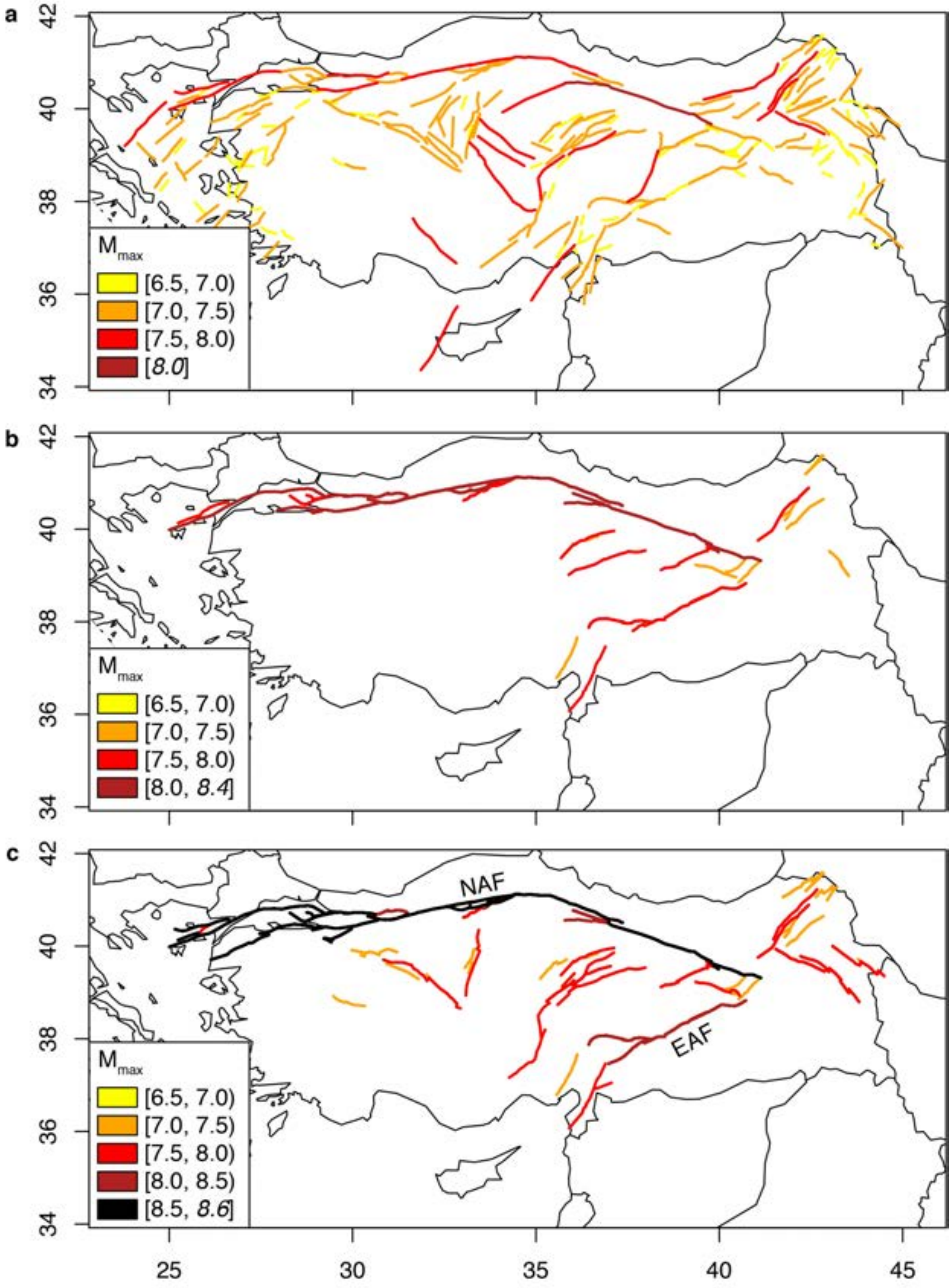
a
b
c
42
40
38
36
34
M_max
[6.5, 7.0)
[7.0, 7.5)
[7.5, 8.0)
[8.0]
[8.0, 8.4]
[8.0, 8.5)
[8.5, 8.6]
NAF
EAF
25
30
35
40
45

Fig. 3.7 M_{max} maps (ESHM13; $\Delta = 5$ km; $\Delta = 10$ km)

The proposed multi-segment rupture approach – by generating physically constrained cascades linking individual fault segments – provides refined values of M_{max}

(which can then yield refined maximum fault displacements for stress tests using this hazard intensity indicator, see STREST WP6). It can be seen as a deterministic approach, by converting the longest modelled cascade rupture into an M_{max} using empirical magnitude-length scaling relationships. Hence it can be used directly in stress test what-if scenarios, providing a refined value of M_{max}. By applying the algorithm presented in the Appendix (Subsection 3.5), a cascade dataset is generated that could be ported into a probabilistic seismic hazard model. Occurrence rates could then be estimated by using the rules already established for composite sources (i.e., using the Gutenberg-Richter law or one of its variants, *etc.*).

Kijko and Singh (2011) provide a review of the state-of-practice on the statistically based M_{max} estimation procedures. All these procedures are seismicity driven and they have certain limitations mostly due to Gutenberg-Richter statistics uncertainties in the magnitude domain. It has recently been shown that the predictive power of these procedures to estimate M_{max} is rather poor (Zöller et al., 2013). Furthermore, Holschneider et al. (2014) found that it is essentially impossible to infer M_{max} from earthquake catalogues alone. These recent results reinforce the need to include the long-term geological data as a more appropriate way to estimate M_{max} and thus to reduce its uncertainty, as initiated in the present study.

The impact of these results on the maximum rupture displacement possible in Turkey will be investigated in WP5/6 in the case of pipelines, relating to STREST CI-B1. The new cascade-based M_{max} what-if scenarios could also be considered as a generic feature of stress tests to earthquakes in WP5. In that scope, new earthquake occurrence rates will have to be assessed based on a frequency-magnitude distribution bounded on a greater M_{max}. The main risk metric for pipelines will then be maximum displacement instead of M_{max}.

3.5 APPENDIX: MULTI-SEGMENT RUPTURE ALGORITHM

An algorithm is proposed to generate cascades based on the four defined criteria for multi-segment rupture. It is an iterative procedure for searching, identifying and linking individual sources into longer fault structures:

1. Input: Select all strike-slip individual fault segments from a fault source database defined by rake $\Re \leq 45°$ or $\Re \geq 315°$ for left-lateral faults and $135° \leq \Re \leq 225°$ for right-lateral faults. Fix increment $i = 0$ and define the set S_0 composed of the n_0 selected segments.

2. Cascade definition loop: For each segment $1 \leq j \leq n_i$ of set S_i:

2.1 Maximum distance (jumping): Define a buffer $\Delta = 5$ km wide (or wider – see previous sections for details) from segment j. Find all segments $k_{tmp} \neq j$ of set S_0 with at least one coordinate point within the buffer zone and with the same mechanism (right-lateral or left-lateral) and dip direction (positive or negative).

2.2 Maximum strike difference (bending/branching): Calculate $\Psi = \Re_j/2+45°$ modulo 90° and $\psi = \gamma_j(45-\Psi-180.\text{atan}(\mu_d)/2\pi)$ with $\gamma_j = 1$ or -1 if segment j is right- or left-lateral, respectively and $\mu_d = 0.12$. Find all segments $k \in k_{tmp}$ which verify $\psi-\delta \leq \varphi_{jk} \leq \psi+\delta$ with $\delta = 30°$ and φ_{jk} the difference between the strikes of segments j and k (see Fig. 3.2 for angle sign convention).

2.3 Relative position of segments (Fig. 3.8): For each segment k, find the 2 nearest anchor points linking segments j and k, each located on segment j and k, respectively. Define the sub-segments j_A, j_B, k_A and k_B defined from the tips of the original segments and the 2 anchor points. Of all possible sub-segment combinations $\{ j_A - k_A, j_A - k_B, j_B - k_A, j_B - k_B\}$, keep only the combinations with obtuse angle (i.e. no backward propagation). If more than one combination remains, save only the longest cascade into the cascade set S_{i+1} and define the cascade rake and strike as the arithmetic mean of the rakes and strikes of the 2 sub-segments.

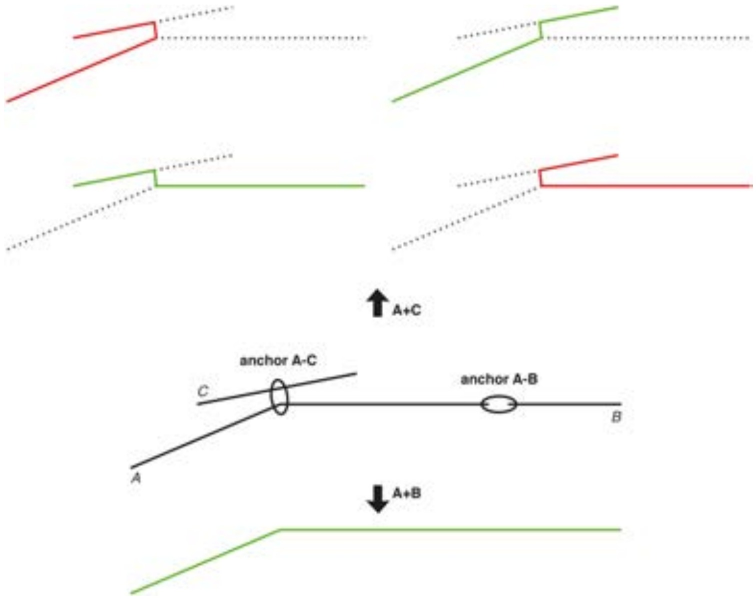

Fig. 3.8 Illustration of step 2.3 of the algorithm

3. Cascade growth loop: Fix $i = i+1$ and repeat step 2 until the number of cascades in S_i is $n_i = 0$ (Fig. 3.9) or tends to a constant maximum cascade length L_{max} (Fig. 3.10). Save all cascades of set S_i into the final cascade set S_{casc}.

In the first iteration $i = 0$, both segments j and k are individual fault segments from input set S_0. In subsequent iterations $i \geq 1$, the input segments j are the cascades defined in the previous iteration, such that any cascade in set S_i is composed of $i+1$ individual segments (or sub-segments). For the case of the Anatolian Peninsula ESHM13 fault segments with $\Delta = 5$ km, the algorithm stopped at iteration $i = 9$ indicating that the longest cascades were composed of 10 ESHM13 segments, complete or partial, in set S_9 (Fig. 3.9). Depending on the fault data configuration, some redundancies may occur (i.e. non-unique sub-segment associations yielding a same cascade path). Although the number of cascades dropped to $n_{10} = 0$ in the present analysis for $\Delta = 5$ km, it is possible that redundant cascades may lead to $n_{+\infty} > 0$. In such a case, step 3 of the algorithm includes a test for maximum length L_{max} stability combined to a maximum number of possible iterations. This is for example the case when using $\Delta = 10$ km, for which stability is obtained at iteration $i = 11$ (Fig. 3.10). By construction, all the cascades generated have tips which match with existing tips of different individual segments defined in ESHM13.

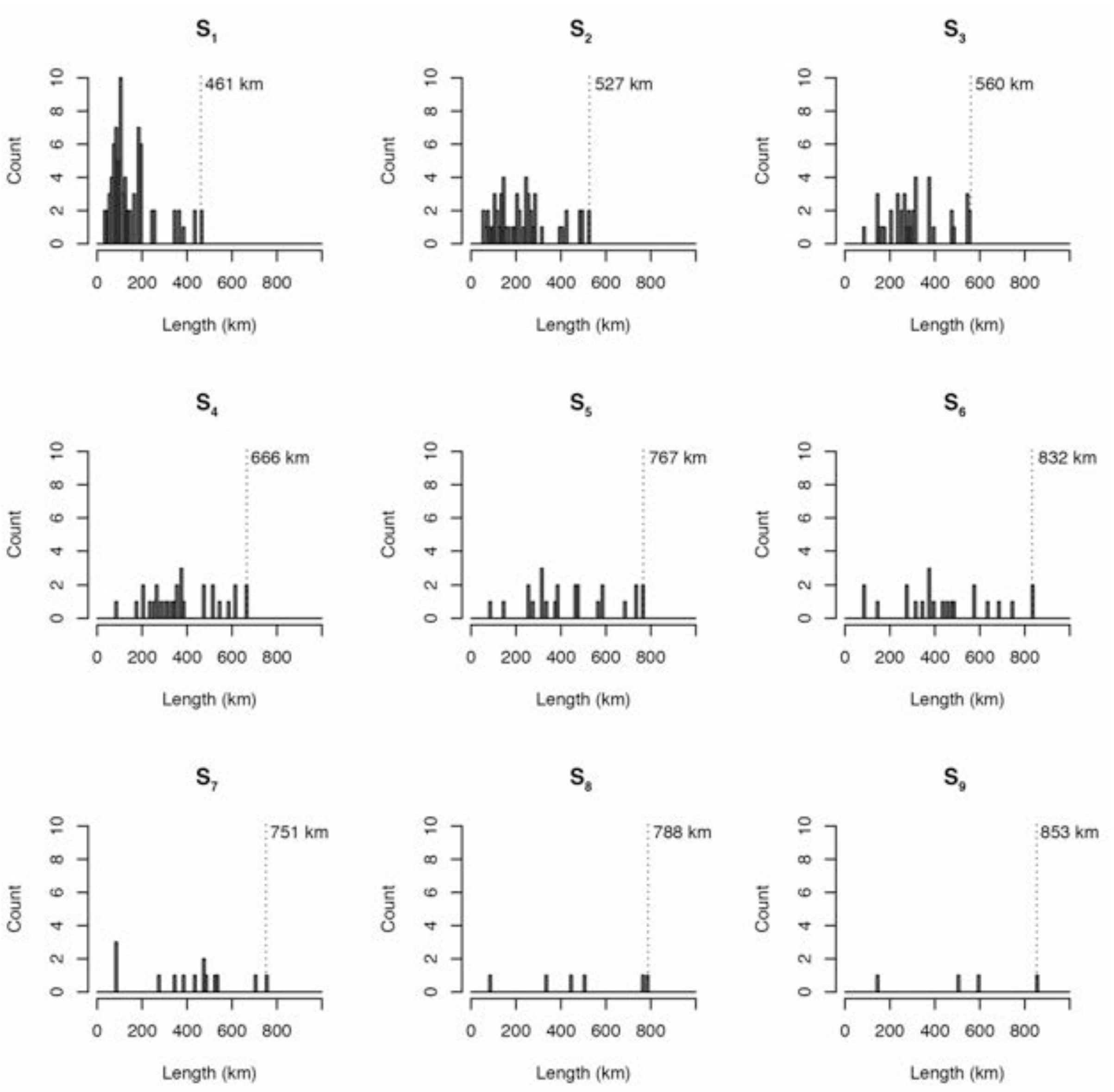

Fig. 3.9 Rupture cascade length distribution at different iterations

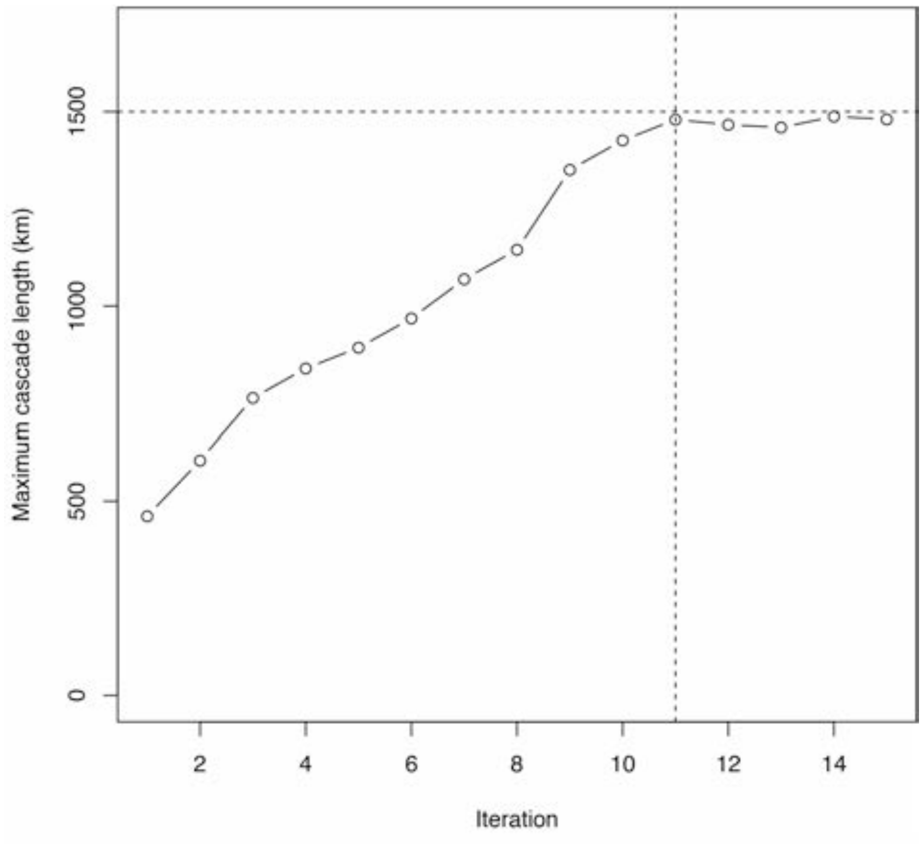

Fig. 3.10 Maximum cascade length L_{max} per iteration

4 Intra-Hazard Interactions: Earthquake-Earthquake Interactions

The work presented below considers the impact of earthquake interactions on hazard (and risk). The role of earthquake clustering on building vulnerability is investigated in STREST WP4. Here a risk analysis is made considering that building vulnerability does not change with pre-damage in order to investigate solely the role of hazard interactions on risk. This analysis uses the GenMR framework presented in Section 2.

4.1 INTRODUCTION

Earthquakes cluster in space and time due to stress redistributions in the Earth's crust (see review by King, 2007). The impact of this clustering on building damage is non-linear, as the capacity of a structure degrades with increased damage (e.g., Polese et al., 2013; Iervolino et al., 2014).

Performance-based seismic assessment consists in quantifying the response of a structure to earthquake shaking using decision variables, such as damage or economic loss. Such a procedure is described in the benchmark *Pacific Earthquake Engineering Research* (PEER) method, summarized by Cornell and Krawinkler (2000). Aftershock probabilistic seismic hazard analysis was added to the PEER method in recent years (Yeo and Cornell, 2009), as well as damage-dependent vulnerability (Iervolino et al., 2014). However, these approaches express earthquake clustering analytically with the temporal component defined from the Omori law and with an ad-hoc spatial component. In particular, they do not consider the coupling of large earthquakes on separate fault segments that is observed in nature. Cases of successive large earthquakes occurring on neighbouring fault segments and within days or tens of days of each other include the 2004-2005 Sunda megathrust doublet (Nalbant et al., 2005), the 1999 Izmit and Duzce North Anatlian earthquakes (Parsons et al., 2000) and the 1811-1812 New Madrid Central United States triplet (Mueller et al., 2004). A more realistic spatiotemporal representation of earthquake clustering is feasible using the well-established theory of Coulomb stress transfer (King et al., 1994; King, 2007) in which earthquake interactions are explicit.

Multi-risk analysis combining explicit interactions between events (being any type of perils) as well as dynamic vulnerability and exposure is the main feature of the GenMR framework (Mignan et al., 2014 – see Section 2). Here, we implement earthquake Coulomb stress interactions in GenMR with an application to fictitious buildings of different generic performances (poor, medium, high) homogeneously distributed within the thrust fault system of northern Italy (STREST CI-C1 site). This area recently encountered a doublet of magnitude $M \sim 6$ earthquakes (2012 Emilia-Romagna seismic sequence; Ganas et al., 2012) with the second event yielding significantly more damage (the number of homeless people raising from 5,000 to 15,000; Magliulo et al., 2014), possibly due to buildings rendered more vulnerable following the first shock. The aim of this section is to provide an overview of the effects of earthquake clustering on "seismic multi-risk", using GenMR as basic framework, and to provide the hazard model necessary for the damage-dependent fragility assessment made in STREST WP4. The method and the risk results apply in principle to any region subject to multiple active faults.

The present study enters in the long-term scope of GenMR, which is to become a comprehensive multi-risk framework by implementing all known types of interactions (natural, natural/technological, technological – see also Section 5). Due to the challenging nature of this task, the inherent complexity of the processes involved and the overwhelming amount of expertise required, simplifications are necessary made, which are clearly stated throughout this section.

4.2 METHOD

4.2.1 Theory of earthquake interactions

The phenomenon of earthquake interaction is well established with the underlying process described by the theory of Coulomb stress transfer (e.g., King et al., 1994). In its simplest form, the Coulomb failure stress change is

$$\Delta\sigma_f = \Delta\tau + \mu'\Delta\sigma_n \qquad (4.1)$$

where $\Delta\tau$ is the shear stress change, $\Delta\sigma_n$ the normal stress change and μ' the effective coefficient of friction. Failure is promoted if $\Delta\sigma_f > 0$ and inhibited if $\Delta\sigma_f < 0$ (see King (2007) for a review).

Coulomb stress transfer is generally not considered in seismic hazard assessment except occasionally in time-dependent earthquake probability models where the “clock change” effect of a limited number of historical earthquakes is included (Toda et al., 1998; Field, 2007; Field et al., 2009). The conditional probability of occurrence of an earthquake is then expressed through a non-stationary Poisson process as

$$\Pr(\Delta t) = 1 - \exp(-N) \qquad (4.2)$$

where N is the number of events expected during Δt. Following Toda et al. (1998),

$$N = \lambda(\Delta t + \mathrm{A}_t) \qquad (4.3)$$

The first term in Eq. 4.3 represents the permanent stress change (so-called “clock change”) with

$$\lambda = \frac{1}{\frac{1}{\lambda_0} - \frac{\Delta\sigma_f}{\dot{\tau}}} \qquad (4.4)$$

where λ_0 is the rate prior to the interaction, $\Delta\sigma_f$ the stress change and $\dot{\tau}$ the stressing rate. The second term of Eq. 4.3 represents the transient stress change (Dieterich, 1994), here termed the “transient amplification”

$$A_t = t_a \log\left(\frac{1+\left(\exp\left(-\frac{\Delta\sigma_f}{A\sigma}\right)-1\right)\exp\left(-\frac{\Delta t}{t_a}\right)}{\exp\left(-\frac{\Delta\sigma_f}{A\sigma}\right)}\right) \qquad (4.5)$$

This transient phenomenon is described by $\Delta\sigma_f$, the constitutive parameter $A\sigma$ and the aftershock duration $t_a = A\sigma/\dot{\tau}$ (Dieterich, 1994) (see Parsons (2005) for a review).

4.2.2 Sensitivity analysis

The parameter set $\theta = \{\Delta\sigma_f, \dot{\tau}, A\sigma\}$ is defined over the intervals $10^{-3} \leq \Delta\sigma_f \leq 1$ bar, $10^{-4} \leq \dot{\tau} \leq 10^{-1}$ bar/yr and $10^{-2} \leq A\sigma \leq 10$ bar for sensitivity analysis. Figure 4.1 shows the influence of each one of the parameters on the conditional probability Pr(Δt = 1 yr, $\lambda_0 = 10^{-3}$, θ) (Eq. 4.2) averaged for the ranges of the two remaining free parameters. $\Delta\sigma_f$ represents the relative local triggering (static stresses decreasing with the inverse of the cubic distance) while $\dot{\tau}$ controls the absolute regional triggering (being related to the tectonic context).

We find that the parameter $A\sigma$ has a relatively limited influence on probability changes compared to $\Delta\sigma_f$ and $\dot{\tau}$, which show opposite effects compared to each other. A strong earthquake clustering requires a low stressing rate (region-dependent) and/or a high stress change (perturbing earthquake very close to the target fault) (e.g., Parsons, 2005). These characteristics remain similar for different values of λ_0. The role of Coulomb stress transfer on seismic risk is investigated in the application to the thrust fault system of Northern Italy, described in Subsection 4.3.

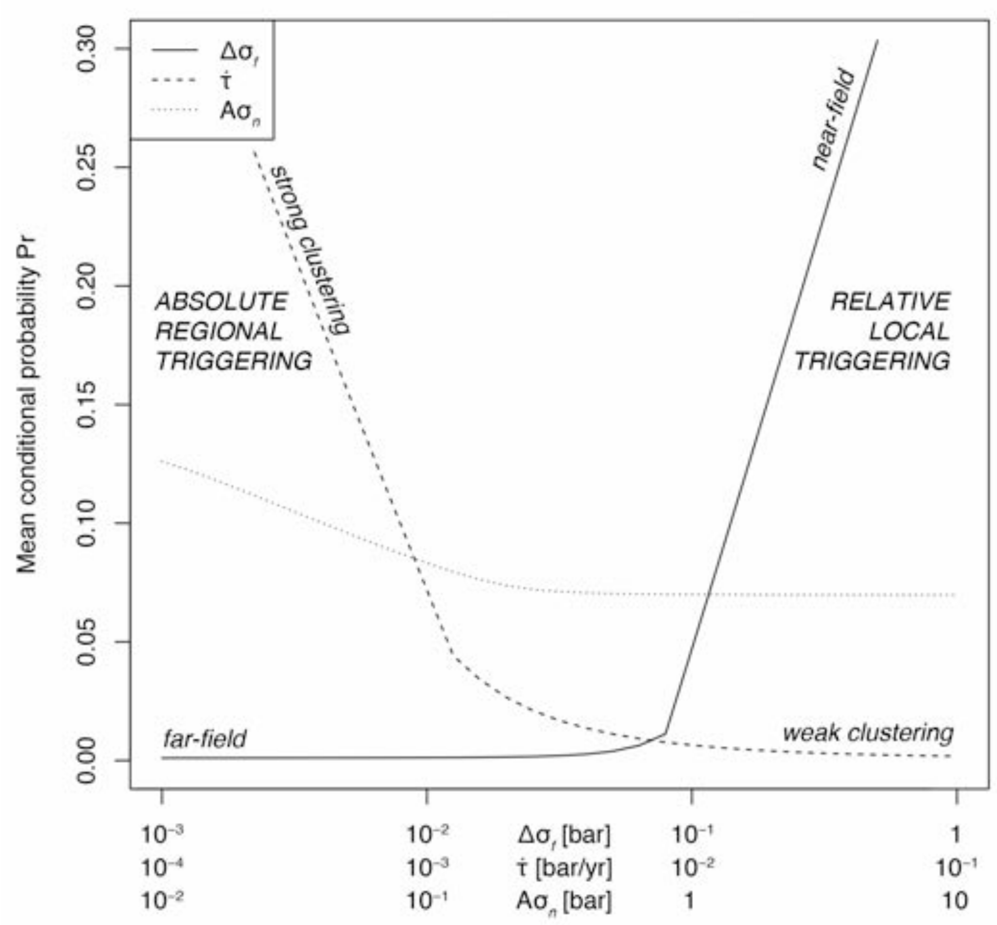

Fig. 4.1 Sensitivity of the mean conditional probability to the parameter set θ

4.2.3 GenMR implementation

GenMR simulates multi-risk scenarios based on the variant of a Markov chain Monte Carlo method (Mignan et al., 2014 – see Section 2). Each simulation generates a time series in the interval $\Delta t = [t_0, t_{max}]$ in which events are drawn from a non-stationary Poisson process. It requires as input (1) an n-event stochastic set with identifier Ev_i and long-term recurrence rate $\lambda_0(\mathrm{Ev}_i)$ and (2) an *n × n hazard correlation matrix* (HCM) with fixed conditional probabilities $\Pr(\mathrm{Ev}_j \mid \mathrm{Ev}_i)$ or time-variant conditional probabilities $\Pr(\mathrm{Ev}_j \mid \mathrm{H}(t) = \{\mathrm{Ev}(t_1), \mathrm{Ev}(t_2), \ldots, \mathrm{Ev}(t)\})$, H being the history of event occurrences up to time t.

Let us note λ(EQ$_j$, t_k) the non-stationary rate of target event EQ$_j$ at the occurrence time t_k of the kth event EQ$_i$, λ(EQ$_j$, t_0) the long-term rate of EQ$_j$ and H(t_0) = {}. Due to the accumulation of permanent stress changes after each earthquake occurrence,

$$\lambda(EQ_j, t_k) = \frac{\lambda(EQ_j, t_0)}{1-\lambda(EQ_j, t_0)\sum_{k=1}^{k}\frac{\Delta\sigma_f(EQ_i(t_k), EQ_j)}{\dot{\tau}(EQ_j)}} \tag{4.6}$$

with Δσ$_f$(EQ$_i$(t_k), EQ$_j$) the stress change on EQ$_j$ due to EQ$_i$ and $\dot{\tau}$(EQ$_j$) the stressing rate on the receiver fault of EQ$_j$. Combining Eqs. 4.2 and 4.3, we obtain the time-variant HCM with conditional probability of occurrence

$$\Pr\left(EQ_j \middle| EQ_i(t_k), \Delta t\right) = 1 - \exp\left\{\lambda(EQ_j, t_k)[\Delta t + \mathrm{A}_t]\right\} \tag{4.7}$$

The HCM for EQ-EQ interactions (hereafter referred to as HCM$_{\text{EQ-EQ}}$) thus depends solely on the matrix Δσ$_f$(EQ$_i$, EQ$_j$), the parameter set θ = {$\dot{\tau}$, Aσ} and the history of event occurrences H defined by the summation term in Eq. 4.6. Since a ratio Δσ$_f$/$\dot{\tau}$ ~ 50:1 is required to significantly skew occurrence probabilities with confidence great than 80-85% (Parsons, 2005), we only consider Δσ$_f$(EQ$_i$, EQ$_j$) values that fulfil this condition.

In any given simulated time series (e.g., Fig. 2.1a), the occurrence time of independent events is drawn from the uniform distribution with $t \in [t_0, t_{max}]$. If EQ$_j$ occurs due to EQ$_i$ following Eq. 4.7, its occurrence time is fixed to $t_j = t_i + \varepsilon$ with $\varepsilon \ll \Delta t$. If $t_j > t_{max}$, the event is excluded from the time series. A small ε represents temporal clustering within a time series. Its choice has no significance on dynamic risk analysis since damage-dependent vulnerability depends on the number of earthquakes in a cluster and not on their time interval (e.g., Iervolino et al., 2014; STREST WP4).

Let us define the null hypothesis H_0 (simulation set S_0) as the case where there is no interaction and the hypothesis H_1 (simulation set S_1) as the case where earthquakes interact with each other. If $\Delta t \ll 1/\lambda_0$ in simulation set S_0, time series with more than one earthquake would be much rarer than time series with only one event (i.e., Poisson process). As a consequence, the potential for clock delays (or removal of events) would be much lower than for clock advances (or additions of events) in S_1. With S_1 likely to produce more earthquakes than S_0, the seismic moment rate would not be conserved. If the sums of moment rates $\sum_i \dot{M}_{0i} = \sum_i M_{0i}\lambda_{0i}$ (Hanks and Kanamori, 1979) between S_0 and S_1 differ by more than 5%, we modify λ$_0$(Ev$_i$) of the stochastic event set, such that

$$\lambda_0' = \lambda_0 \frac{\hat{\lambda}(S_0)}{\hat{\lambda}(S_1)} \tag{4.8}$$

Simulation set S_0 and S_1 are then regenerated with the modified stochastic event set. This action is repeated until the 5% limit is reached. λ'$_0$ here represents the rate of trigger earthquakes, which is lower than the rate of trigger and triggered earthquakes combined.

4.2.4 Generic building & damage assessment

We need to assess the damage to estimate the potential impact of earthquake clustering. Indeed, it is simpler to consider the sum of damages due to a cluster of earthquakes than an equivalent to the sum of ground shaking footprints. Damage/risk is also the main output of GenMR and is the basis of the *risk migration matrix* (RMM) tool. In this section, we use the concept of Virtual City (see definition in Subsection 2.2.2) to build a generic building and matching generic fragility curves. Those are only used in the present report. Application to CI-C1 would require a more sophisticated approach, which is however out of the scope of this report (see STREST WP4/WP6).

We consider a fictitious n_b-story building with story height h_b and fundamental period

$$T_b = c_1 (n_b h_b)^{c_2} \tag{4.9}$$

with parameters c_1 = 0.08 and c_2 = 3/4, h_b in meters and T_b in seconds (e.g., Gülkan and Akkar, 2002). The building is subjected to the spectral displacement $S_d(T_b)$ due to earthquake occurrences. We determine the ground story drift ratio Δ_{EQ} as

$$\Delta_{EQ} = \frac{4}{\pi}\frac{S_d(T_b)}{h_b}\sin\left(\frac{\pi h_b}{2\left(\frac{T_b}{c_1}\right)^{\frac{1}{c_2}}}\right) \tag{4.10}$$

following the formulation proposed by Gülkan and Akkar (2002), assuming an idealized shear frame and only the first mode of oscillation.

We describe the generic capacity curve of the fictitious building by its stiffness K, yield strength Q and ductility μ_Δ (Fig. 4.2a). We define the mean damage δ as a function of the drift ratio (or shear deformation) Δ

$$\begin{cases} \delta(\Delta < \Delta_y) = \left(\frac{\Delta}{\Delta_y}\right)^3 \\ \delta(\Delta_y \leq \Delta \leq \Delta_{max}) = 1 + (n_{DS} - 1)\frac{\Delta - \Delta_y}{\Delta_{max} - \Delta_y} \\ \delta(\Delta > \Delta_{max}) = n_{DS} \end{cases} \tag{4.11}$$

where n_{DS} is the number of damage states, $\Delta_y = Q/K$ the yield displacement capacity and $\Delta_{max} = \Delta_y \mu_\Delta$ the maximum plastic displacement capacity. The relationship between δ and Δ is assumed linear within the plasticity range and saturates to the maximum damage state above. Within the elasticity range, δ decreases faster towards zero assuming a power-law behaviour. We fix n_{DS} = 5 with DS_1 to DS_5 representing insignificant, slight, moderate, heavy and extreme damage, respectively (Fig. 4.2b). Eq. 4.10 indicates that DS_1 is most likely at $\Delta = \Delta_y$ and DS_5 at $\Delta = \Delta_{max}$ (e.g., FEMA, 1998). We here assume that extreme damage corresponds to building collapse.

We then generate fragility curves from the cumulative Binomial distribution

$$\Pr(\geq DS_k | \Delta_{EQ}) = \int_0^{\Delta_{EQ}} \left(\frac{n_{DS}!}{k!(n_{DS}-k)!}\left(\frac{\delta(\Delta)}{n_{DS}}\right)^k \left(1 - \frac{\delta(\Delta)}{n_{DS}}\right)^{n_{DS}-k}\right) d\Delta \tag{4.12}$$

for each damage state DS_k with $0 \leq k \leq n_{DS}$ (e.g., Lagomarsino and Giovinazzi, 2006) (Fig. 4.2c). Other methods to develop building fragility curves conditioned on a ground motion intensity measure, whose hazard can be estimate, could be used.

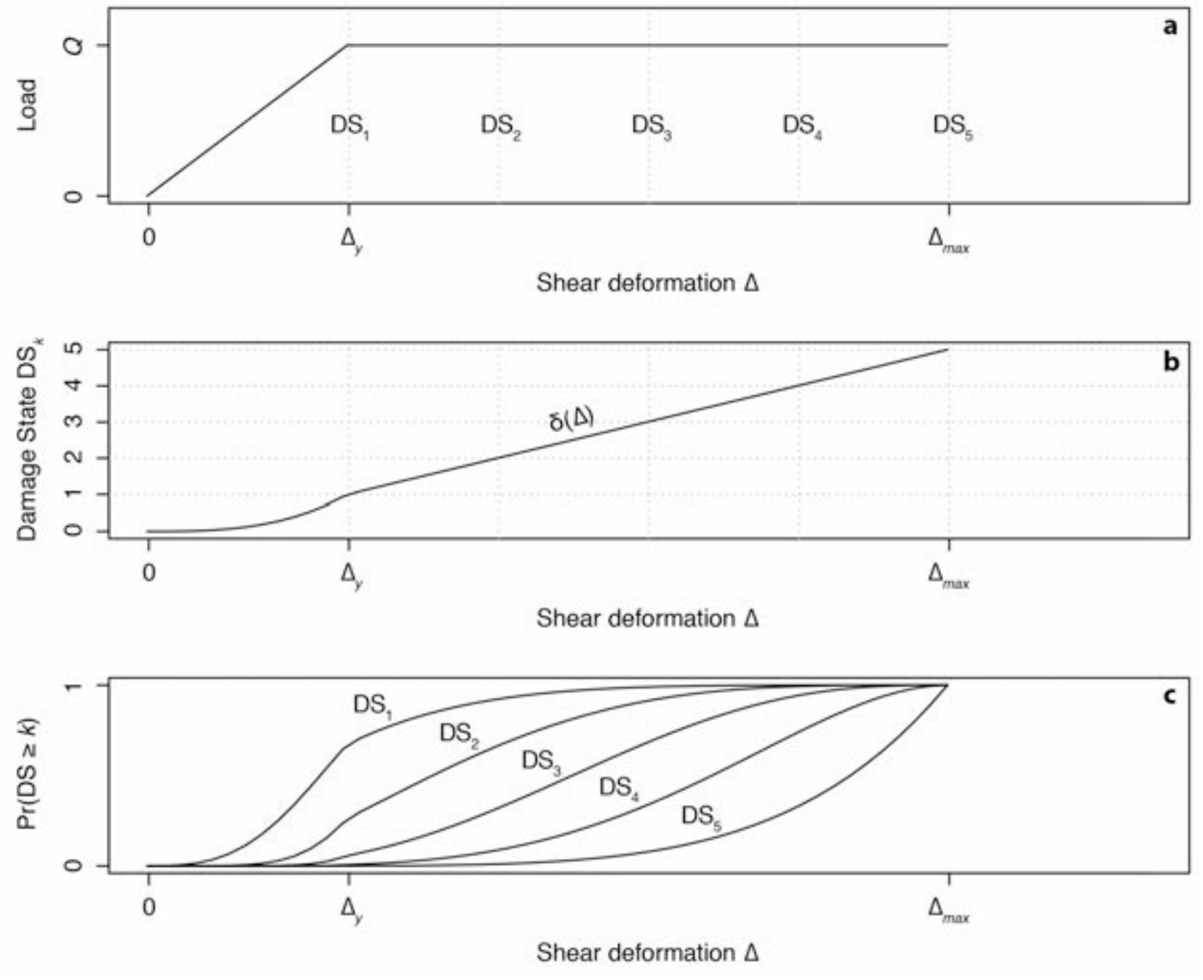

Fig. 4.2 Generic building capacity curve, matching damage states & fragility curves

4.3 APPPLICATION: NORTHERN ITALY (GENERIC BUILDING)

4.3.1 Stochastic event set

We defined a set of n = 30 stochastic events representing characteristic earthquakes on idealized straight fault segments. These segments are simplified versions of the 20 shallow thrust composite faults defined in the 2013 *European Seismic Hazard Model* (hereafter ESHM13) for northern Italy. This model represents the latest seismic hazard model for the European-Mediterranean region (Basili et al., 2013; Giardini et al., 2013), combining the up-to-date information about earthquakes, active faults and crustal deformation, including the quantification of model and data inherent uncertainties for Europe and Turkey without the limits of national borders. Table 4.1 lists the ESHM13 identifier, slip rate $\dot{s}$, dip, rake and maximum magnitude M_{max} of the 20 ESHM13 composite sources as well as the length L, width W, characteristic magnitude M_{char} and long-term rate $\lambda_0 = \lambda(t_0)$ of the 30 stochastic events. Figure 4.3 shows the map of northern Italy and the correspondence between the stochastic events EQ$_i$ and the ESHM13 sources. Only lateral triggering is considered on these simplified fault geometries. Potential interactions due to the possible rooting of different fault segments into a same deep structure are not considered.

M_{char} is derived from the seismic moment M_0 [dyn.cm]

$$\log M_0 = c + dM_{char} \tag{4.13}$$

with $c = 16.05$, $d = 1.5$ (Hanks and Kanamori, 1979) and

$$\log A = -13.79 + 0.87 \log M_0 \tag{4.14}$$

with $A = LW$ [m^2] (Yen and Ma, 2011; see Stirling et al. (2013) for a review). It follows that $M_{char} \in [6.1, 6.6]$.

The rate λ_0 is derived from the long-term slip rate $\dot{s}$ and fault displacement u following Wesnousky (1986)

$$\lambda_0(EQ_i) = \frac{u(EQ_i)\dot{s}(EQ_i)}{(\sum_{k=1}^{k=n} u(EQ_k))^2} \tag{4.15}$$

weighted by the number n of stochastic events EQ_k possible on a same ESHM13 source (Table 4.1). It yields the total rate $\sum\lambda_0 = 0.013$ or one M_{char} earthquake every ~77 years in northern Italy. The fault displacement u (also used in stress transfer calculations) is obtained from

$$u = \frac{M_0}{\mu LW} \tag{4.16}$$

with the shear modulus $\mu = 3.2\ 10^{11}$ dyn/cm^2 (Aki, 1966).

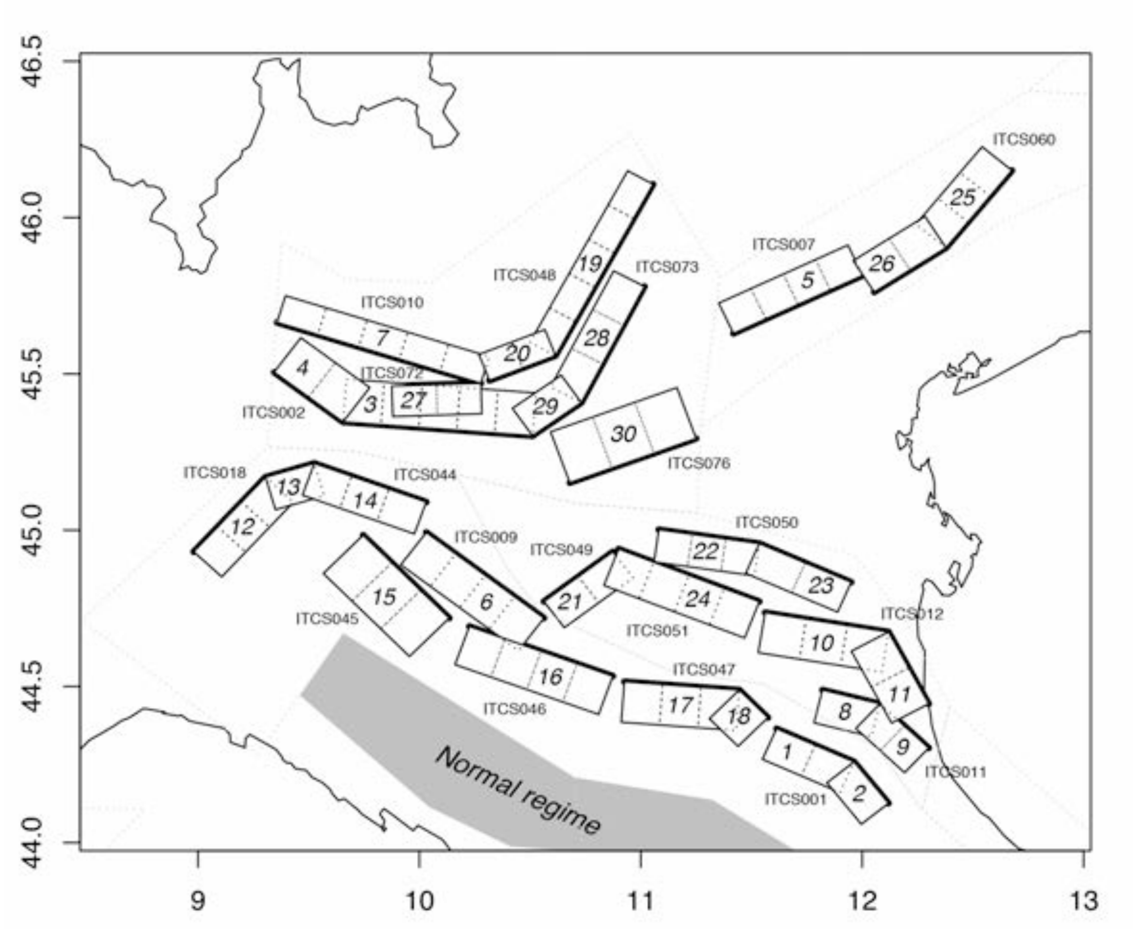
46.5
46.0
45.5
45.0
44.5
44.0
9
10
11
12
13
ITCS060
ITCS007
ITCS048
ITCS073
ITCS010
ITCS072
ITCS002
ITCS076
ITCS018
ITCS044
ITCS009
ITCS049
ITCS050
ITCS045
ITCS051
ITCS012
ITCS047
ITCS046
ITCS011
ITCS001
1
2
3
4
5
6
7
8
9
10
11
12
13
14
15
16
17
18
19
20
21
22
23
24
25
26
27
28
29
30
Normal regime

Fig. 4.3 Simplified surface projection of the 20 ESHM13 shallow thrust composite faults ITC*xxxx* in northern Italy

Table 4.1 Stochastic earthquake set

ESHM13 Id.	Slip rate (mm/yr)	Dip (°)	Rake (°)	M_{max}	EQ Id.	L (km)	W (km)	M	λ_0 (/10^{-3} yr)
ITC5001	0.300	35.0	90	6.8	1	21	10	6.3	0.205
					2	14	10	6.1	0.192
ITC5002	0.300	32.5	90	6.9	3	47	13	6.6	0.185
					4	21	13	6.3	0.164
ITC5007	0.900	35.0	90	6.8	5	35	10	6.4	2.133
ITC5009	0.500	30.0	105	6.9	6	36	12	6.5	1.155
ITC5010	0.300	35.0	90	6.7	7	53	9	6.5	0.688
ITC5011	0.300	30.0	90	6.8	8	15	10	6.1	0.200
					9	17	10	6.2	0.204
ITC5012	0.520	30.0	100	6.9	10	31	12	6.4	0.326
					11	21	12	6.3	0.308
ITC5018	0.175	32.5	75	6.7	12	26	11	6.4	0.430
ITC5044	0.510	30.0	90	6.8	13	13	10	6.1	0.311
					14	29	10	6.4	0.353
ITC5045	0.300	30.0	90	7.0	15	30	16	6.5	0.683
ITC5046	0.300	30.0	90	6.9	16	38	12	6.5	0.690
ITC5047	0.300	30.0	90	6.9	17	28	12	6.4	0.209
					18	10	12	6.1	0.179
ITC5048	0.300	35.0	85	6.7	19	50	9	6.5	0.201
					20	17	9	6.1	0.172
ITC5049	0.175	40.0	75	6.8	21	21	11	6.3	0.444
ITC5050	0.420	40.0	90	6.9	22	25	11	6.3	0.261
					23	25	11	6.3	0.260

ITC5051	0.375	35.0	90	6.9	24	37	12	6.5	0.861
ITC5060	0.650	40.0	80	6.9	25	26	12	6.4	0.405
					26	21	12	6.3	0.393
ITC5072	0.300	37.5	90	6.7	27	22	10	6.3	0.770
ITC5073	0.300	35.0	85	6.8	28	34	10	6.4	0.202
					29	15	10	6.1	0.178
ITC5076	0.300	30.0	90	7.1	30	33	16	6.6	0.673

4.3.2 $\mathrm{HCM}_{\mathrm{EQ\text{-}EQ}}$

The main input of the $\mathrm{HCM}_{\mathrm{EQ\text{-}EQ}}$ is the matrix of Coulomb stress changes $\Delta\sigma_f(\mathrm{EQ}_i, \mathrm{EQ}_j)$ here computed using the Coulomb 3 software (Lin and Stein, 2004; Toda et al., 2005; Toda et al., 2011). The inputs to the software are the effective coefficient of friction $\mu' = 0.4$, the fault segment characteristics (Fig. 4.3; Table 4.1) and the earthquake slip u (Eq. 4.16). $\Delta\sigma_f$ [bars] was computed on ~10 km-wide dislocation patches and then averaged over the full fault segments. Figure 4.4 shows the map of $\Delta\sigma_f(\mathrm{EQ}_1, \mathrm{EQ}_j)$, which indicates that triggering occurs principally at the tips of the trigger segment on segments of similar strike and mechanism (all reverse).

The impact of $\Delta\sigma_f$ on clustering patterns and of $\dot{\tau}$ on clustering levels is investigated in Subsection 4.3.4. It should be noted that the maximum stress changes, computed on segments closest to a rupture, rarely exceed 1 bar. The stresses released on ruptured segments are of the order of several bars. For central Italy, Catalli et al. (2008) obtained $7.10^{-5} \leq \dot{\tau} \leq 7.10^{-3}$ bar/yr based on seismicity rates and $A\sigma = 0.4$ bar. For the present application, we fixed $A\sigma = 0.1$ bar and tested $\dot{\tau} = \{10^{-4}, 10^{-3}, 10^{-2}\}$ bar/yr to represent strong, medium and weak clustering (see Fig. 4.1). Loose constraints on the regional value of $\dot{\tau}$ (e.g., Catalli et al., 2008) do not allow us to determine which clustering regime is the most likely in northern Italy.

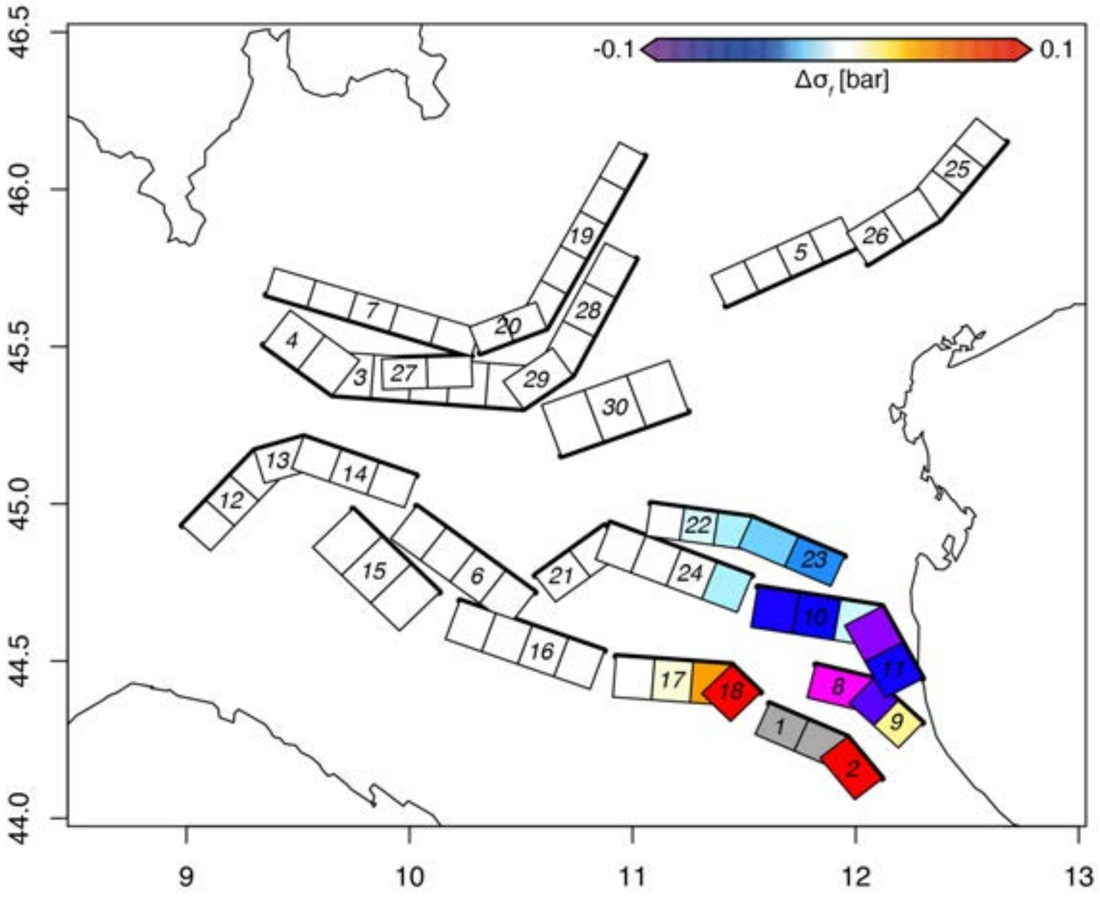

Fig. 4.4 Coulomb stress changes $\Delta\sigma_f(EQ_1, EQ_j)$ due to EQ_1 on receiver faults

4.3.3 Generic building and damage assessment in northern Italy

We consider a generic 1-story building of height h_b = 7 m (e.g., industrial building basic typology, ~ STREST CI-C1) and fundamental period T_b = 0.34 sec (Eq. 4.9). Following Gülkan and Akkar (2002), a yield drift Δ_y of 0.01 is adopted. We test three different building performances (poor, medium, high) represented by different ductility capacity values μ_Δ = {2, 4, 6}, which lead to drift capacities Δ_{max} = {0.02, 0.04, 0.06}.

The damage to the building is due to its drift. In turn, the building drift is estimated from the elastic spectral displacement $S_d(T_b)$ of the earthquake assuming that the equal displacement rule holds. Spectral displacement is derived from the spectral acceleration $S_a(T_b)$ by

$$S_d(T) = \left(\frac{T}{2\pi}\right)^2 S_a(T) \tag{4.17}$$

We compute $S_a(T_b)$ for each stochastic event using the ground motion prediction equation of Akkar and Bommer (2010)

$$\log(S_a) = b_1 + b_2 M + b_3 M^2 + (b_4 + b_5 M)\log\sqrt{R_{jb}^2 + b_6^2} + b_7 S_S + b_8 S_A + b_9 F_N + b_{10} F_R + n\sigma \tag{4.18}$$

with S_a in cm/s^2, $M = M_{char}$ the earthquake magnitude (Table 4.1), R_{jb} the distance to the fault surface trace in km, $S_S = 1$ and $S_A = 0$ (soft instead of stiff soil), $F_N = 0$ and $F_R = 1$ (reverse instead of normal faulting) and $n\sigma$ the number of standard deviations from the mean log(S_a) value. The fitting parameters $b_{1\text{-}10}$, which depend on period T, are given in Akkar and Bommer (2010). We computed earthquake hazard (i.e. ground shaking) on a regular grid of generic buildings spaced every 0.05° (~5 km) in longitude and latitude in northern Italy. Figure 4.5a shows the $S_a+1\sigma_{tot}$(0.35 sec) spatial footprint of EQ$_3$ ($M_{char} = 6.6$). Figure 4.5b shows one stochastic version – as defined in GenMR – taking into account the aleatory variability described by σ_{tot} (0.35 sec) = 0.32 in the lognormal distribution of S_a.

The damage state is then estimated as described in section 4.2.4. Figure 4.5c shows the mean damage δ footprint (Eq. 4.11 with $\mu_\Delta = 2$) expected for the $S_a+1\sigma_{tot}$ footprint of Figure 4.5a. Figure 4.5d shows one stochastic version – as again defined in GenMR – taking into account the aleatory variability of damage in the binomial distribution of δ (Eq. 4.12). In the present study, we consider as risk metric the number $N_{\text{DS4+}}$ of generic buildings with damage state $\text{DS}_k \geq 4$ (i.e., heavy to extreme damage). With the generic buildings distributed every ~ 5km, $N_{\text{DS4+}}$ is expected to remain small by construction. For the example of Figure 4.5d, $N_{\text{DS4+}} = 7$. Let us note that the results are subject to high epistemic uncertainties. These uncertainties (not quantified in the present report) propagate from the hazard layer (e.g., choice of Eq. 4.18, definition of the stochastic event set) to the damage layer (e.g., Eq. 4.10, definition of the building drift capacity curve).

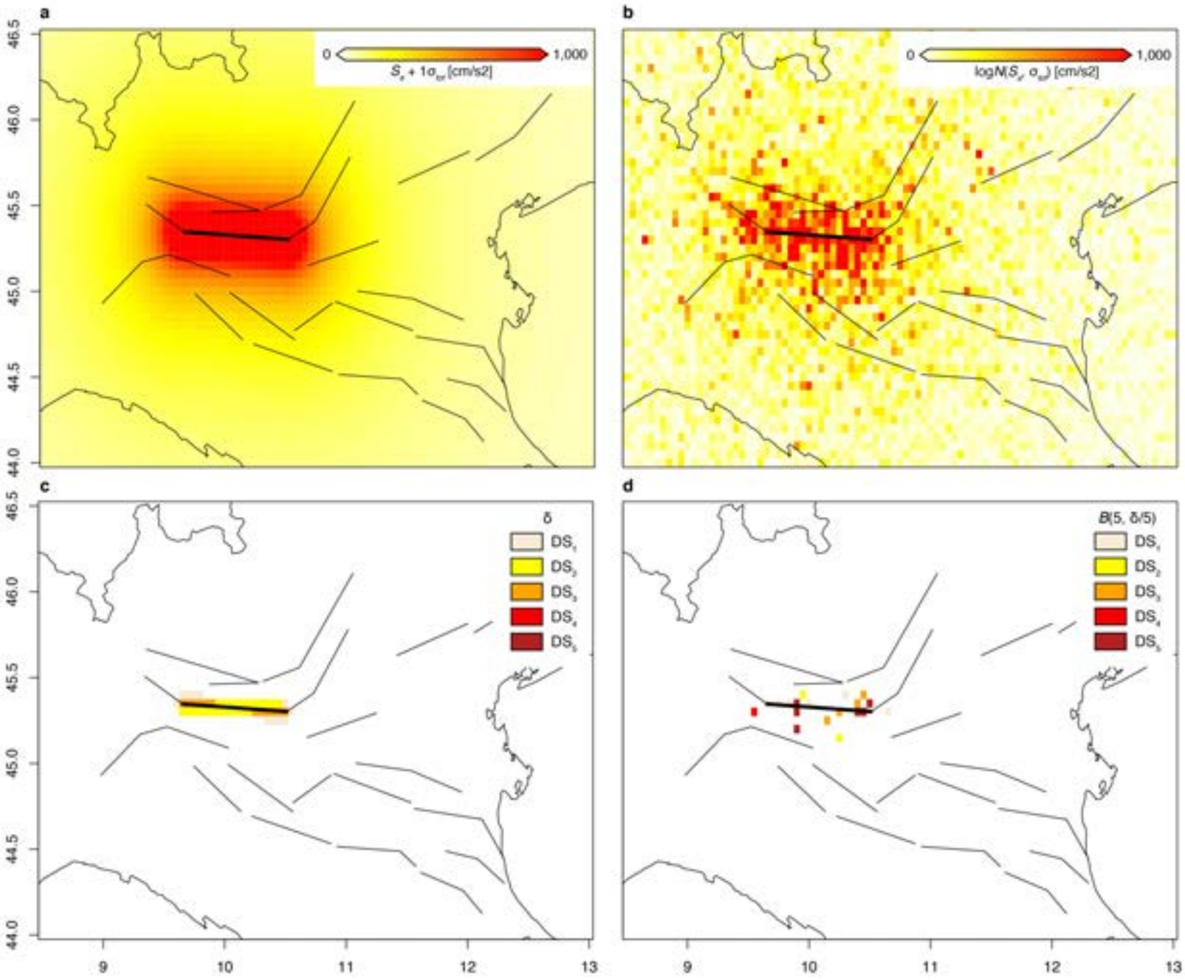

Fig. 4.5 Earthquake hazard & damage footprints (incl. aleatoric uncertainties) for EQ$_3$

4.3.4 Results

We ran $N_{sim} = 10^6$ simulations per hypothesis, with each hypothesis H_i leading to one GenMR simulation set S_i. With the tested parameters $\dot{\tau} = \{10^{-4}, 10^{-3}, 10^{-2}\}$ bar/yr and $\mu_\Delta = \{2, 4, 6\}$, representing respectively the level of clustering (strong/medium/weak) and the building performance (poor/medium/high), a total of 9 simulation sets was obtained (i.e., sensitivity analysis on the role of 3 earthquake clustering levels to 3 building performances). In addition, 3 additional simulation sets were produced, corresponding to the null hypothesis of no earthquake interaction for each one of the 3 building performances.

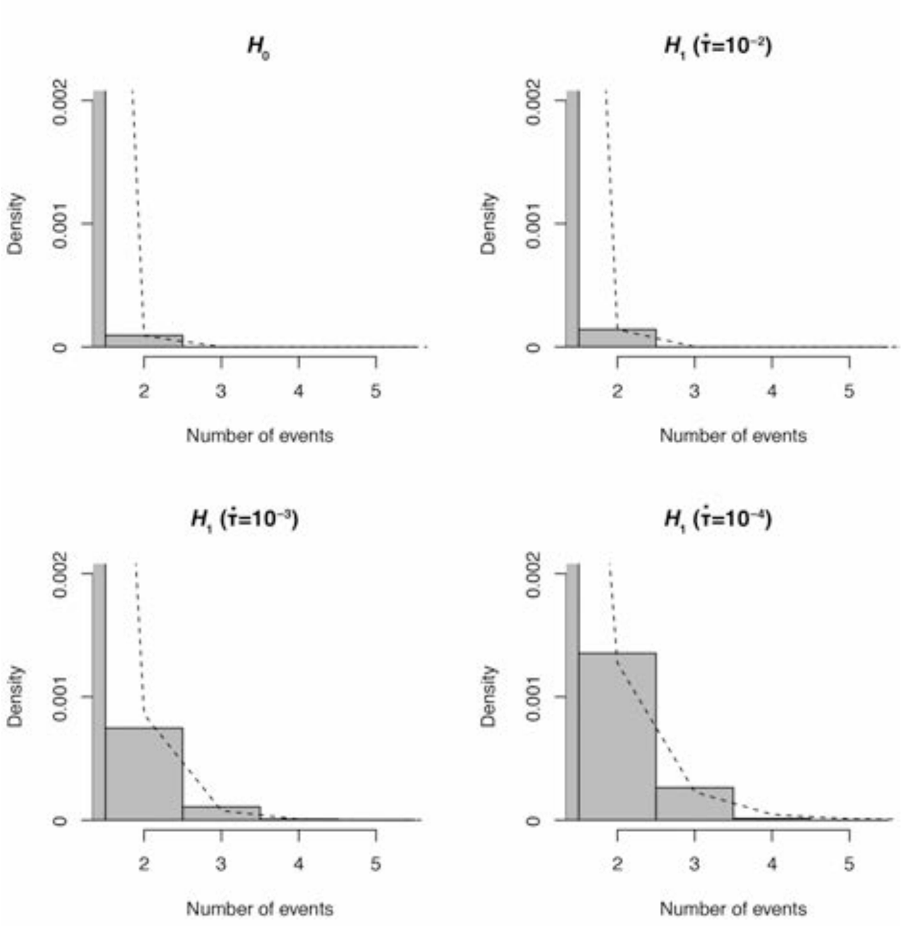

Fig. 4.6 Distribution of the number of earthquakes per simulated year

Figure 4.6 shows the distribution of the number of earthquakes per simulated year. The null hypothesis H_0 (no earthquake interaction) is well fitted by a Poisson distribution while the other hypotheses including different levels of clustering are all better fitted by a negative Binomial distribution (i.e., lower Akaike Information Criterion AIC). The fits to the data are represented by the dashed curves in Figure 4.6. Based on the stochastic event set of Table 4.1 / Figure 4.3 and N_{sim}, the largest simulated earthquake cluster is composed of five consecutive events. For $\dot{\tau} = \{10^{-4}, 10^{-3}, 10^{-2}\}$ bar/yr, the index of dispersion

$$\phi = \frac{\sigma^2}{\mu} \tag{4.19}$$

with μ the mean and σ^2 the variance of the distribution equals to {1.36, 1.15, 1.01}. It allows us to quantify the degree of clustering, with the clustering verified to increase with decreasing stressing rate $\dot{\tau}$. For the highest stressing rate considered, the clustering is almost non-existent. These results represent an instance of “migration”, as predicted at an abstract level by Mignan et al. (2014) (see Fig. 2.5). Let us note that most earthquake clusters correspond to combinations of segment ruptures on a same fault or on several nearby faults. Examples include EQ_1-EQ_2, EQ_5-EQ_{26}-EQ_{25}, EQ_{12}-EQ_{13}-EQ_{14}, *etc.* (Fig. 4.3).

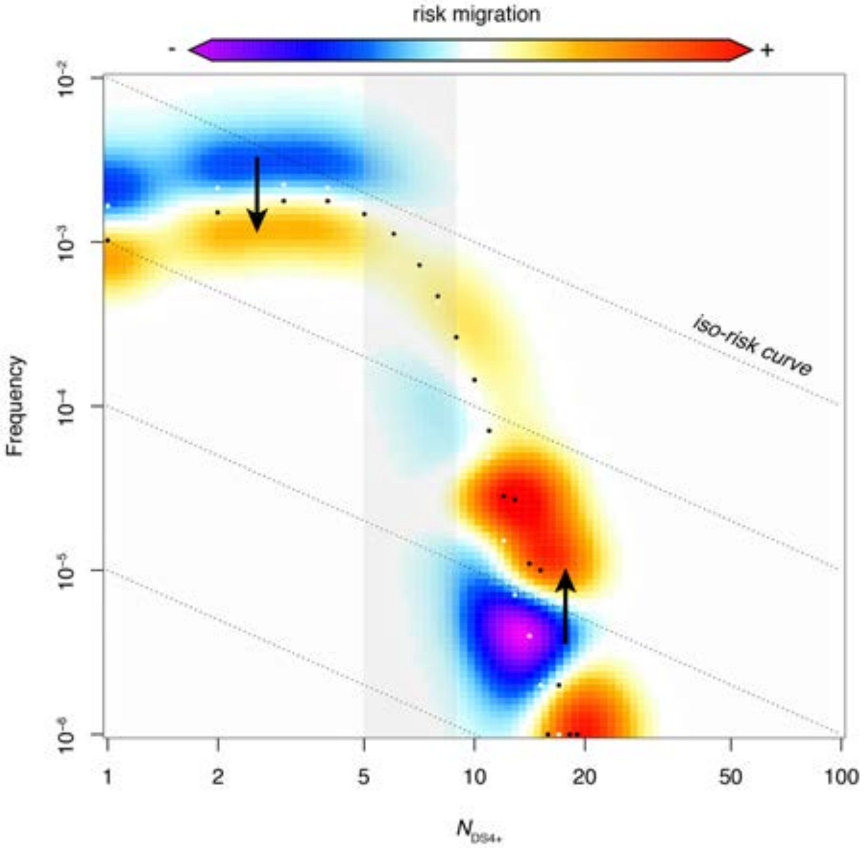

Fig. 4.7 Risk migration matrix (RMM) for strong earthquake clustering & poor building performance

Figure 4.7 shows the RMM for the simulations with/without interactions for fixed parameters $\dot{\tau}$ = 10^{-4} bar/yr (strong clustering) and μ_Δ = 2 (poor building performance). Risk scenarios from the null hypothesis H_0 are represented by white dots and earthquake clustering risk scenarios from H_1 by black dots. The risk metric is N_{DS4+} (see section 4.3.3). Red represents an increase of risk at a specific frequency-loss domain, and blue a decrease (see Mignan et al., 2014 and Section 2 for other examples of RMMs). The present RMM shows that the risk of high-probability–low-consequences events decreases while the risk of low-probability–high-consequences events increases when interactions between earthquakes are considered. A “high-probability–low-consequences” event here refers to one M_{char} earthquake and a “low-probability–high-consequences” event to a cluster of at least two M_{char} earthquakes. While the combined effects of several earthquakes simply sum up, N_{DS4+} could be further increased due to increasing building vulnerability. This is however not considered in the present study (see discussion of Subsection 4.4 “implications for stress tests”). The migration of risk from short return intervals to longer ones is also illustrated in Figure 4.8, which shows the difference (H_1 - H_0)/H_0 between the two loss curves (or exceedance probability - N_{DS4+} curves).

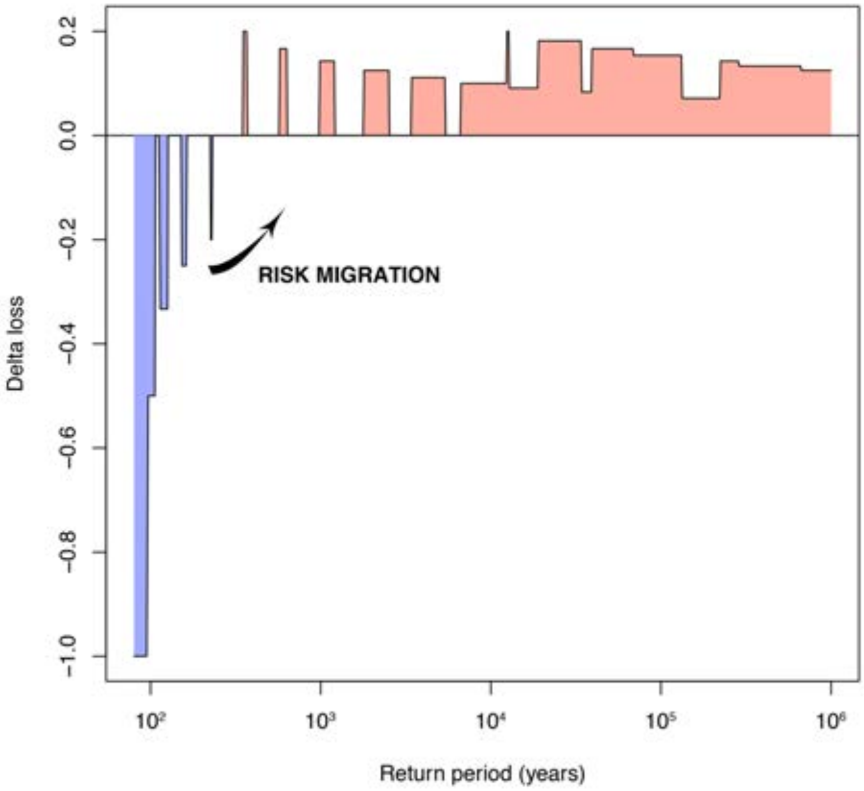

Fig. 4.8 "Delta-loss" curve matching the RMM of Figure 4.7

Let us note that the risk migration shown in the RMM of Figure 4.7 disappears for higher $\dot{\tau}$ values as well as for higher μ_Δ values (Fig. 4.9). The first case is trivial as it represents a lowering of clustering (Fig. 4.6). The second case is explained by the fact that better performing buildings yield less damage, which means that the cumulative effects of several earthquakes are also smaller than for buildings of poor performance (again, without considering damage-dependent vulnerability, STREST WP4 topic). Red and blue patches are visible on all the RMMs of Figure 4.9 but a migration pattern is only clearly observed in the case $\{\dot{\tau} = 10^{-4}$ bar/yr, $\mu_\Delta = 2\}$ (Fig. 4.9 bottom left; Fig. 4.7). The "tiling" pattern observed elsewhere is due to the discretized nature of the risk metric with N_{DS4+} here defined by low integers.

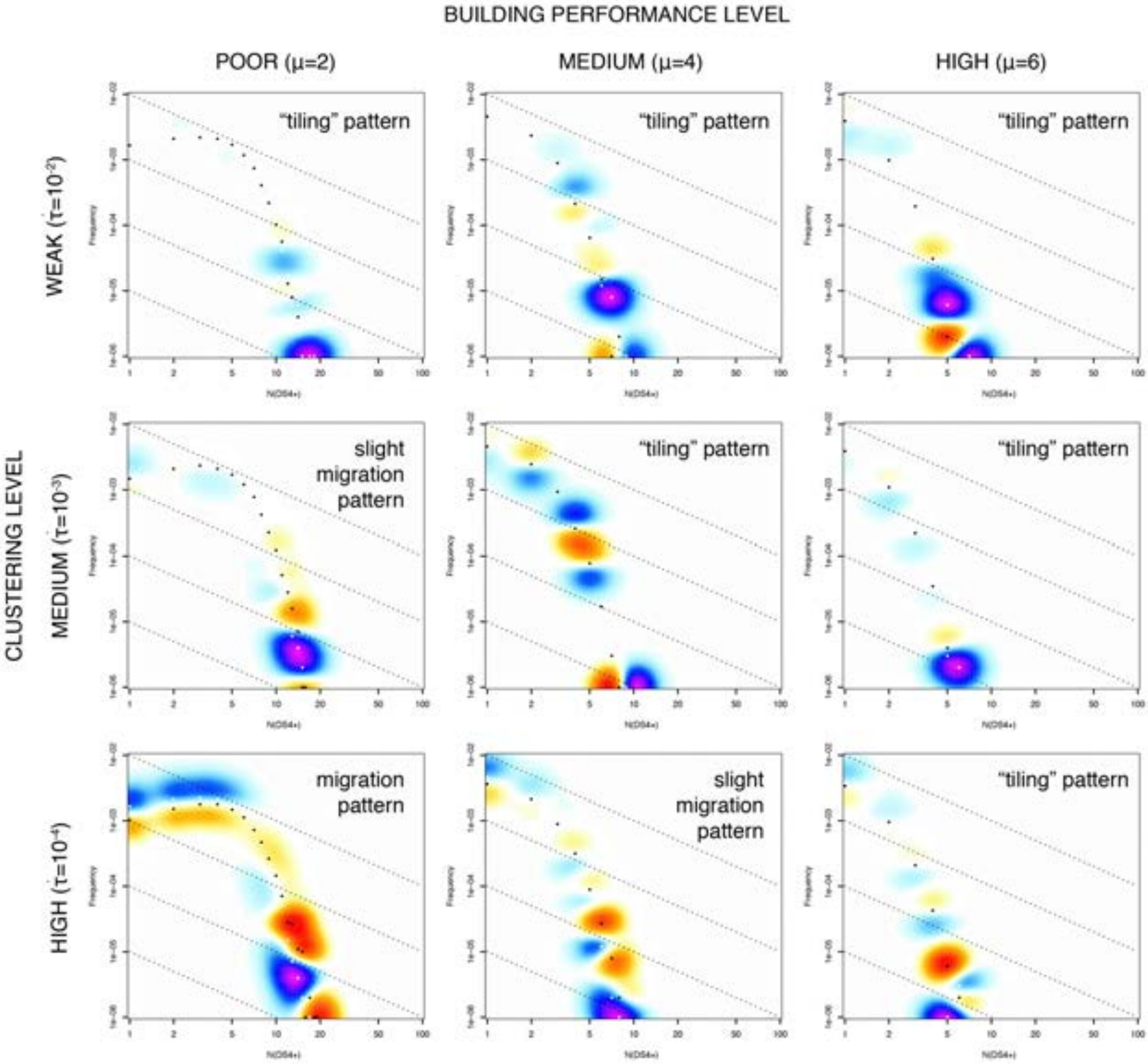

Fig. 4.9 RMM for different clustering and building performance levels

The impact of earthquake clustering is also blurred by the high aleatoric uncertainties (e.g., Fig. 4.5). Indeed, one “severe” earthquake may yield a higher N_{DS4+} than several “mild” earthquakes combined. This is verified in Figure 4.10, which shows the N_{DS4+} distribution for one characteristic earthquake. For a building of poor performance (μ_Δ = 2), a severe earthquake can be more damaging than the sum of 3 earthquakes producing average damage (case of no damage-dependent vulnerability - dotted lines representing once, twice and three times the median risk value N_{DS4+} in Figure 4.10). For a building of high performance (μ_Δ = 6), no damage is produced on average, which means that a cluster of earthquake is also likely to produce no damage, as already indicated above (again, in the present case without damage-dependent vulnerability).

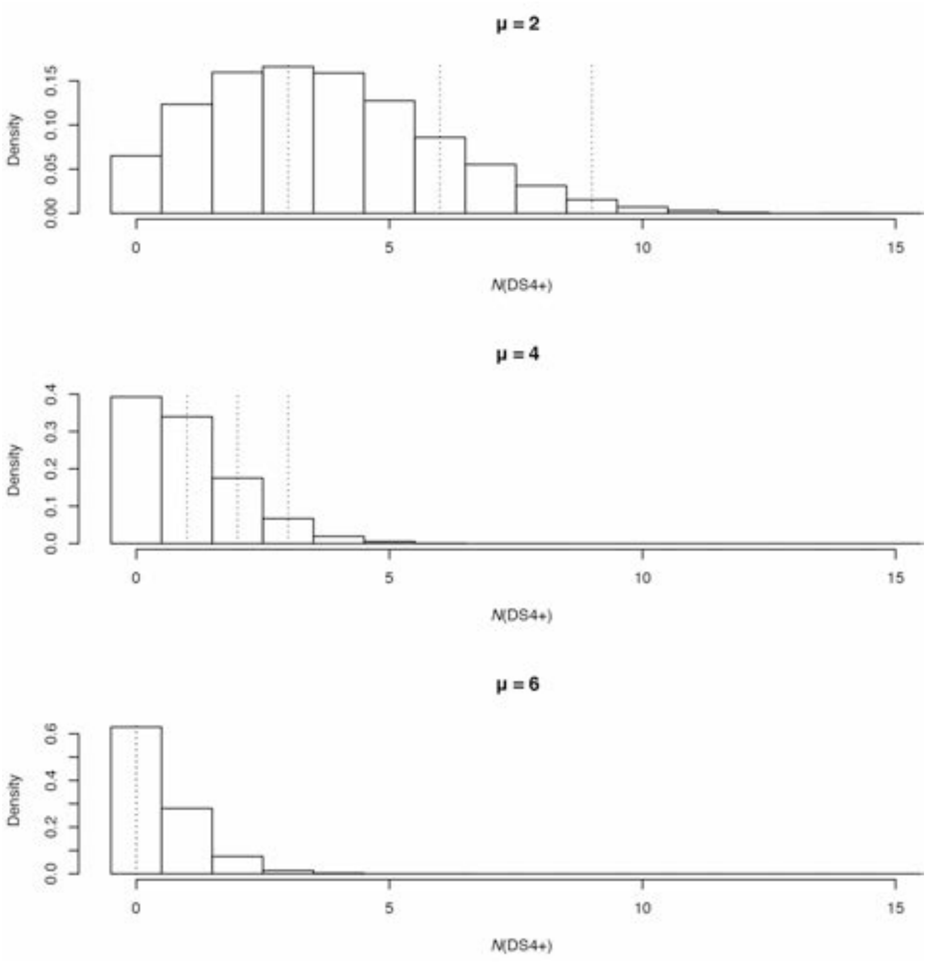

Fig. 4.10 N_{DS4+} distribution for one characteristic earthquake

4.4 IMPLICATIONS FOR STRESS TESTS

We have implemented earthquake-earthquake interactions within the GenMR framework and applied it to generic buildings in northern Italy (where STREST Ci-C1 is located). We have verified that earthquake clustering leads to risk migration, meaning that while the overall risk remains the same, the risk of high-probability–low-consequences decreases and the risk of low-probability–high-consequences events increases. Such a migration is of interest in stress test design where the role of extremes is considered. Such a migration can be approximated by a negative binomial distribution (Figs. 4.6, 4.11a). Site-specific analyses however require an in-depth investigation of stress interactions within a fault network to identify if clustering is possible and if so, where it is maximal. For northern Italy, lack of knowledge on the tectonic stressing rate does not allow us to conclude which clustering level is most likely. In a stress test framework, we therefore recommend considering strong earthquake clustering ($\dot{\tau} = 10^{-4}$ bar/yr) as well as no clustering. In the case of generic buildings, the combination of high aleatoric uncertainties on both hazard (GMPE sigma, Eq. 18) and damage (binomial distribution, Eq. 12) (Figs. 4.5, 4.10) make the role of earthquake clustering on risk difficult to assess (i.e. blurred clustering signal). Overall, the role of earthquake clustering alone does not seem critical in the present case in a stress test framework. However addition of damage-dependent vulnerability should amplify the risk associated to earthquake clustering, which could have an impact in stress tests (Fig. 4.11b). This is investigated in other WPs of the STREST project.

As a general comment, the RMM (combined to the GenMR framework) seems to be a promising tool for stress test design (for STREST WP5). For instance, the RMM of Figure 4.11b shows how a stress test passes or fails depending on the degree of risk migration and risk amplification due to hazard interactions and other dynamic aspects (Mignan et al., in press, b).

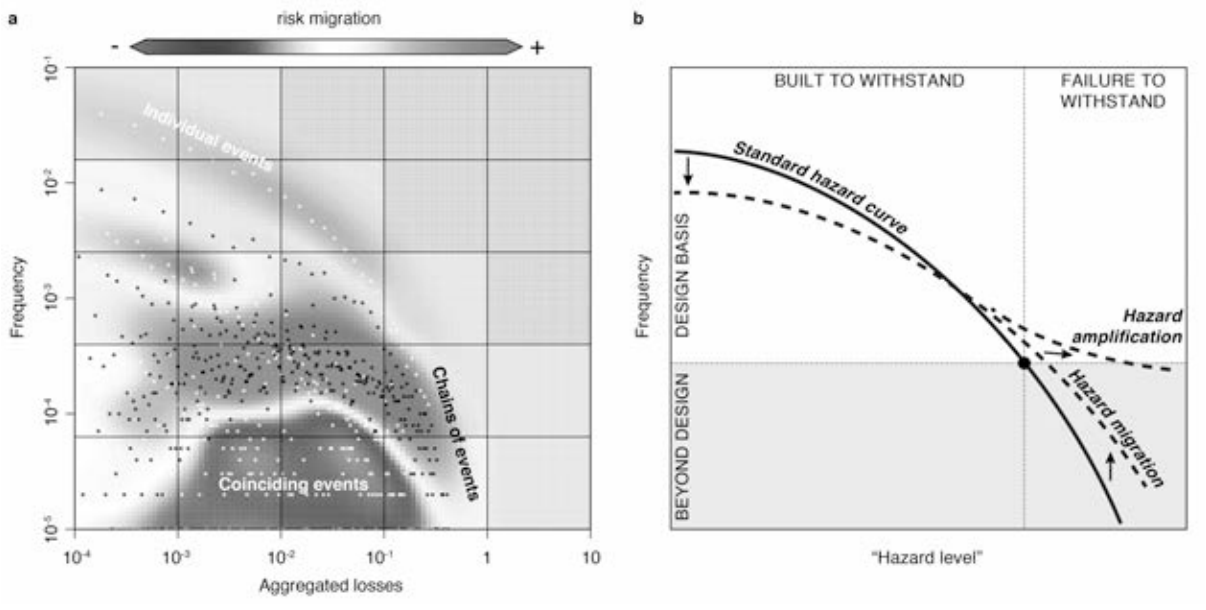

Fig. 4.11 Stress test design using the RMM (Mignan et al., in press, b)

5 Inter-Hazard Interactions: Case of Large Dams

5.1 OVERVIEW

5.1.1 Introduction

Dams can be impressive structures, ranking amongst the largest built by man. Between other uses, they are crucial to address water consumption, energy supply, and flood protection concerns.

They operate by modifying the natural flow of water, temporarily retaining it in an upstream reservoir. Reservoirs can vary substantially in terms of capacity, being that some can store staggering volumes, well beyond 1 000 million m^3 of water. The potential energy content that large dams can hold is enormous.

In case of failure, there are important consequences associated with the dam body, yielding losses of direct (e.g. the value of the infrastructure, affected workers) and indirect (e.g. disruption of energy supply) nature. More relevant still is the role the water plays when the reservoir is abruptly released. Following such an event the dam-break wave propagates fast, likely with swift and devastating consequences to downstream areas.

Dams can be affected by natural, internal, operational, and societal hazards. Among the first are earthquakes, floods, landslides, rock falls, avalanches, ice, and meteor strikes. Internal hazards relate to a deterioration of the dam, foundation, or key operational elements such as spillways. They can come in the form of seepage, piping, sediment accumulation, instability on the foundation or abutments, embankment erosion, embankment settlement, or concrete deterioration, for example. Operational hazards can be related to human errors and equipment malfunction (e.g. gate jamming or loss of power). Finally, societal hazards can take the form of acts of war, terrorism, vandalism, and others (Darbre, 1999).

Dams and their appurtenant structures are adapted to the surrounding landscape, thus displaying a wide variety of types and forms. Adding to the pivotal role of the reservoir, this specificity naturally poses challenges when adopting a general risk assessment framework. In a detailed risk analysis context each dam system – if not each of its elements – should be described individually.

As a result of the awareness to the potential dangers posed by dams that is displayed by regulators, dam owners, designers, and society in general, design and safety criteria guidelines are regularly updated in national regulations and in the documentation issued by the International Commission on Large Dams (ICOLD).

Most countries promote a deterministic approach to dam safety assessment. According to it, it must be proven that the system can withstand extreme events, but the evaluation of the actions that would lead to failure is not necessarily undertaken. As a result, the actual probability of a dam failure remains in many cases unknown and, consequently, so does the associated residual risk.

Although there have been attempts to prepare generic frameworks for the classification and prioritization of the risks associated with dams, their quantification constitutes a much more difficult problem to address. This is true particularly for large dams, whose structural responses are typically simulated by detailed 3-D finite element models considering fluid-structure interaction, very hard to integrate in probabilistic frameworks. In what dam-break waves are concerned, modelling is also hard to integrate due to the required resources (time and cost) and assumptions made. On the one hand, statistical approaches are impaired by the lack of information, which results from the extraordinary nature of the events that can pose a threat to well-designed large dams. On the other hand, detailed probabilistic risk assessments for dams are rare and costly procedures, mostly justified only when particularly sensitive assets can potentially be affected by a dam failure (e.g. nuclear power plants). Because of the specificity of each infrastructure, the findings of the limited number of detailed probabilistic risk assessments carried out to date are not easily transposed to other systems.

Because large dams differ widely in their characteristics and due to the fact that their safety is commonly evaluated against a set of deterministic scenarios, a sufficiently encompassing pool of knowledge on fragility and vulnerability functions for key dam components is still lacking in literature.

The work described in the present section explores the application of the GenMR framework (Section 2, Mignan et al., 2014) to large dams. Particularly, it was sought to integrate the modelling of the reservoir – pivotal to the simulation and understanding of the system – in the framework. To that end, a conceptual infrastructure, inspired on the many large dams located on the Swiss Alps, was devised.

In the light of the existing knowledge gaps and the goals of the work, the description of hazards and elements of the system was simplified and, to large degree, based on expert judgement (related to the concept of Virtual City). Notwithstanding, this description has been bound to observations whenever possible.

This chapter focuses exclusively on hazard interactions in the dam system and does not cover loss estimation. In fact, although dams are valuable infrastructures on their own and damages to their components are costly, a major part of the losses associated with dam failure can be expected downstream, in the areas potentially affected by the dam-break wave. Because the assessment of such losses requires the propagation of the dam-break wave, the identification of vulnerability functions of downstream assets to large floods, and the estimation of these assets' values, its inclusion on the GenMR framework is a complex task that should, however, come as a follow up to the present work.

When evaluating the contents of this section, it is important to keep in mind that the representation of the system is simplified and that the description of the generic hazards, elements, and interactions that characterize it are approximate. As a consequence, an acknowledgeable epistemic uncertainty is associated with all simulations.

5.1.2 Brief account of a dam's main components and operation

There are a number of potential uses for a dam. Notably, large dams are employed for hydropower production, regularization of seasonal water availability, and flood protection, among other activities. Regardless of the particular purpose of a dam, it operates by temporarily storing water in the reservoir upstream of the structure and controlling its outflow.

As mentioned previously, several types of large dam structures exist. On the most basic level and excluding unusual designs, these can be classified into concrete (or masonry) and embankment dams. In the first group one can include gravity, buttress, and arch dams. The second group includes earth- and rock-filled dams.

The volume of the reservoir is of the greatest importance for the operation and safety of the system. The hydrostatic pressure exerted on the dam structure by the water upstream, as well as interstitial pressures created as water percolates through the dam and its foundation, are, in fact, responsible for some of the main forces acting on the system.

The evolution of the reservoir's contents is a function of inflows (mainly in the form of contributions from rivers and rainfall) and outflows (a sum of evaporation, infiltration, and controlled discharges at the dam). The mass balance or retention equation that represents the process is transcribed below:

$$V_{t+1} = V_t + Q_t^{in} + P_t - Q_t^{out} - E_t - I_t \tag{5.1}$$

where V_t is the reservoir volume at time t, Q_t^{in} are the inflows, P_t is the direct contribution of precipitation over the reservoir, Q_t^{out} are the outflows controlled by the dam, E_t represents evaporation, and I_t is the infiltration component.

In most situations, inflows to the reservoir vary substantially according to season. In opposition, for economic reasons it is desirable that the hydropower system is used at a more or less constant rate throughout the year, provided that sufficient water is available. The reservoir volume is therefore pivotal in order to transfer water from "wet" to "dry" seasons.

Also, it is customary that the reservoir's volume is used to laminate floods, thus reducing peak discharges and mitigating their impacts. In fact, for many dam systems, extreme inflows can surpass the spillway's outflow capacity. When this is the case, it is expected that the excess volume accumulated during the peak of the flood is safely stored in the reservoir, being progressively released thereafter. This translates into a reduction of the maximum flood discharge, but also imposes a minimum volume available in the reservoir at all times.

As a system, the key features of large dams can be conceptually simulated resorting to a relatively small number of key components. These are the dam structure itself, its foundation and abutments, and the components responsible for controlling outflows from the reservoir:

- The spillway, typically with a large discharge capacity and responsible for maintaining the volume of the reservoir within safe margins during floods;
- The bottom outlet, which provides added outflow capacity and can at times be used to lower the reservoir or flush sediments;
- The hydropower system, which albeit being the preferential outlet due to economic reasons, commonly displays a limited outflow capacity; and
- The dam crest, over which water eventually flows if the reservoir's contents rise abnormally.

Naturally, accounting for the specificities and numerous subcomponents of these elements can increase the system's complexity substantially. Albeit, in the scope of a full probabilistic risk assessment, such an endeavour would be worthwhile to some extent, a high degree of detail in the system's representation was not deemed necessary here.

In this chapter a conceptual embankment dam system is analysed. Compared to their concrete counterparts, embankment dams can be regarded as more resilient to some seismic actions, particularly when faults are present. They are, however, more vulnerable to episodes of overtopping and internal erosion, both with the potential to lead to the progressive removal of aggregate material at the dam's structure and foundation and, eventually, lead to its failure by breach formation.

5.1.3 Historical perspective

Much knowledge on the risks associated with dams has been amassed to date. Today, following a number of catastrophic events and averted disasters, experts have a solid grasp of the mechanisms that can lead to dam failure.

Historically, dams have been most vulnerable during the initial filling of the reservoir with an acknowledgeable number of the recorded failures having taken place at this stage. Beyond the initial phase, the largest share of failures has been associated with embankment dams. In past records, floods have been the main natural hazard triggering dam collapse. Notwithstanding, internal erosion, aging, upstream dam break waves, and earthquakes are other examples of important hazards (Lemperiere, 1999). Bellow, a shortlist of paradigmatic cases of dam failure or near-failure is presented.

The failure of the Banqiao embankment dam (Ru River, Henan Province, China) in August 1975, was caused by overtopping following high inflows during a large storm (Xu and Zhang 2009). While the combined design outflow capacity of the dam was of 1 742 m^3/s, the peak inflow to the reservoir was estimated at 13 000 m^3/s (Gee 2009). Following the dam breach, a maximum discharge of 78 000 m^3/s is believed to have been released (ICOLD 2012). As a direct result of the flood, including the dam break wave, 30 000 lives were reported lost (ICOLD 2003). In an arguably biased publication, which is however valuable in order to gain insight into the disaster, a range of numbers departing from the official 26 000 drowned to an unofficial total of 230 000 deaths (encompassing ensuing epidemics and famine) are given. Along with the Banqiao Dam, other 61 dams collapsed during the storm (Si and Qing 1998). The catastrophe resulted from a number of coinciding events. Firstly, from an unusually high flood and poor design and construction, but also from failure in telecommunication lines and cascading effects between impounded areas.

The double-arched concrete Vajont Dam, in Italy, provides another example of a paradigmatic event. In October 1963, a major landslide took place on the slope of Mount Toc, leading to the abrupt collapse of over 270 Mm^3 into the partially filled reservoir (Hendron Jr and Patton 1987, Müller-Salzburg 1987, ICOLD 2000). Due to concerns with the stability of the slope motivated by earlier slides, the Vajont Reservoir's operational level was revised and filling operations conditioned. Although displacements on the slope were being monitored and the possibility of a large landslide was acknowledged, both the scale and the speed of the event were unforeseen (Müller-Salzburg 1987). In addition to the reservoir filling, previous rainfalls contributed to the instability of the slope (Hendron Jr and Patton 1987, ICOLD 2000). As the landslide hit the reservoir, a large mass of water was displaced, reaching the village of Casso, in the opposite margin of the reservoir. Additionally, a wave of over 100 m (ICOLD 2000) overtopped the dam and propagated through the valley downstream, affecting the villages of Longarone, Pirago, Villanova, Rivalta, and Fae (Müller-Salzburg 1987). Although the dam structure resisted the event, 1925 people were killed.

The Teton earthfill dam (Teton River, Idaho, USA) collapse, in 1976, is a well-documented case of internal erosion. An earthfill dam is usually comprised of several layers of material; relevantly, at least one of these layers must be comprised of impervious material that reduces water percolation downstream. Also at the level of the foundation and its interface with the dam body, it is important that percolation is minimal. If this is not guaranteed, there is a risk of fine material being progressively washed away. During the first filling of Teton Dam, two days prior to its failure, small springs were identified at the riverbed level downstream of the dam. Two days later water was observed at the downstream face of the embankment and near the dam toe. Efforts to stop the erosion process failed and, in a matter of hours, the erosion process led to a full breach reaching the dam crest and the consequent release of the reservoir (Seed and Duncan 1981). The disaster killed 11 people. Being a consequence of geological and construction factors, the analyses following the collapse of the dam provided valuable knowledge to dam designers. Notably, they raised awareness to the speed at which internal erosion processes may develop (Seed and Duncan 1981).

In the past, earthquakes have affected a substantial number of dams. The Loma Prieta earthquake (October 1989, California, USA) induced strong shaking in about twelve embankment dams (ICOLD 2001). The so-called Austrian earthfill dam, located approximately 12 km from the epicentre, was the only one significantly affected, with a maximum crest settlement approaching 1 m and some cracking in the abutments. Fortunately, at the time of the event and following a prolonged draught, the reservoirs of the affected dams were far below their full supply levels. This is considered to have played a substantial role regarding the Austrian Dam withstanding the event. The deformations observed in the embankment were larger than expected for an equivalent loading, prompting the need for yet more performing engineering models. Overall, the Loma Prieta earthquake evidenced the impact that the reservoir can play in the response of dams to seisms and that, if well designed, embankment dams can withstand well seismic actions (ICOLD 2001).

The near collapse of the Lower Van Norman Dam following the San Fernando earthquake (February 1971, California, USA) provided independent evidence of the important role of reservoir levels. Having the embankment dam experienced liquefaction and major slope failures, it was only due to the fact that the reservoir's level was lower than usual that a large area, with approximately 70 000 residents, was not flooded (ICOLD 2001).

Beyond the cases mentioned above, many more accounts of the response of dams to natural hazards can be found in literature. With relevance to the application of the GenMR framework to dams, it can be inferred from such accounts that the reservoir initial state at the time of the trigger event is of paramount importance, as is the evolution of its volume. Also, the study of combinations of hazards and/or cascades of events is important, as these can account for a significant share of the risk associated with dam systems.

5.2 THEORY

5.2.1 On current design practices and safety criteria for large dams

Although the work described in this section is not directly related to current design standards for large dams, it is useful to briefly mention these in order to put into perspective the responses of the simulated system.

A risk-based approach to dam safety and decision-making has been a topic of debate for at least two decades, but most regulators refrain from specifying thresholds of acceptable or tolerable risk, adopting deterministic criteria for design standards instead. These standards envisage that failures do not occur. To that end, it must be demonstrated that, even under extreme scenarios, the structures are able to guarantee the integrity of the reservoir. Although all major hazards that might affect a large dam project should be accounted for, the extreme scenarios that are generally preconized for large dams focus mainly on earthquakes and floods – a precise definition depending substantially on national regulations. Typically they include the Maximum Credible Earthquake (MCE, or an event of very low occurrence probability, e.g. 10^{-4} to 10^{-7}) (ICOLD 2014) and the Probable Maximum Flood (PMF, or, again an event of very low occurrence probability) (ICOLD 1992).

Several scenarios should be considered for both flood and earthquake hazards during large dam design. An example are ICOLD's guidelines (ICOLD 2014, Wieland 2014), which promote the evaluation of:

- An operating basis earthquake, with a return period of 145 years, that must not translate into structural damage or loss of service in either the dam or its appurtenant structures;
- A design basis earthquake, with a return period of 475 years, which is the reference earthquake for the appurtenant structures. Limited damages to the dam are tolerated as long as its stability is guaranteed and no substantial water release takes place;
- A safety evaluation earthquake, with a deterministic (MCE) or probabilistic definition (maximum design earthquake, MDE; return period of 10 000 years), to which the dam must resist without an uncontrolled water release from the reservoir. Also, all major safety elements should remain operational.

Although MCE and PMF actions are not evaluated simultaneously, coincident design scenarios of earthquake and flood are often taken into account. As an example, dams may still be required to accommodate flood events following extreme earthquakes (Wieland 2014). In other cases, in particular when spillways are controlled by mechanical equipment, extreme flood scenarios should be assessed assuming a reduced outflow capacity (Federal Office for Water and Geology 2002).

Because the critical infrastructure, which the GenMR framework was applied to, is inspired from Swiss Alpine dams, Swiss safety regulations are of particular interest. For large dams, two types of flood must be evaluated. These are (Federal Office for Water and Geology 2002):

- The design flood (T=1 000 yr), which must be routed under normal conditions without any damage to the system and while guaranteeing a given safety margin (freeboard); and
- The security flood (PMF, but with peak discharge not inferior to 1.5 times that of the design flood), which must not lead to the failure of the dam. The level of water in the reservoir must be such that no risks are posed by it (for embankment dams always below the crest level, as no overtopping is accepted; for concrete dams limited overtopping is allowed as long as the foundation is not endangered).

The reservoir is admitted at full supply level at the beginning of both evaluations. Also, in the case of mobile parts in discharge structures, it must be assumed that the one with the

---

largest outflow capacity is out of operation (except for concrete dams under the security flood).

Regarding seismic security for large dams, Swiss safety regulations demand the assessment of the dynamic and static responses of the structure to an earthquake with a return period of 10 000 years. This earthquake must not lead to the uncontrolled release of water from the reservoir. For embankment dams, eventual settlements and deformations must not surpass an admissible threshold. Also, any eventual overflow has to be avoided though the maintenance of an adequate freeboard. In concrete dams the appearance of local instabilities is inadmissible, as is the possibility of erosion phenomena potentially leading to the uncontrolled release of the reservoir (Federal Office for Water and Geology 2002).

5.2.2 Brief overview of relationships between natural hazards affecting dams

There are a number of natural hazards with the potential to affect dam systems. As argued in the following, they are interrelated to some degree, justifying an inter-hazard approach to dam risk assessments.

Earthquakes pose a threat to the dam body, foundation, and appurtenant structures. They can, as such, condition the normal operation and outflow capacity of the system. It is reasonable to assume that earthquakes can directly trigger other relevant hazards such as mass slides or internal erosion (in the case of embankment dams). Beyond direct stresses and displacements induced by the earthquake, hydrodynamic pressures prompted by the instability of the dam and reservoir might be produced. In embankment dams and on granular material foundations liquefaction processes might be relevant. By excessive settlement of the crest or compromise of the outflow capacity prior to a major flood, overtopping can also ensue.

As seen before, floods should be a major source of concern to dam designers, operators, and decision makers. Besides the danger of overtopping they represent, the rise of the reservoir to abnormal levels can contribute to increased hydrostatic loads on the dam structure and to the build-up of interstitial pressures. In many cases, flood events are also correlated with extreme rainfall over large areas, which hint potential correlations with dam failures within the same watershed. Also, as evidenced in the aftermath of the Vajont disaster, high rainfalls can yield increased probabilities of mass slides.

Mass slides in the form of landslides, rock falls, avalanches, glacier calving, or debris flows can displace a large volume of water within the reservoir. Following a major impact, a tsunami wave can be generated and, eventually, exert added pressure on the dam structure and/or lead to its overtopping. Meteor strikes, though unlikely, can have consequences of the same type.

Weather can also play a role in dam safety. As an example, ice can contribute to the jamming of mobile equipment and apply substantial stresses to the structure.

Internal erosion processes are very relevant, particularly, but not exclusively, in regard to embankment dams. They can occur within the dam body, in the foundation, or on the interfaces between layers of different characteristics. Although they can be argued not to constitute a natural hazard, the difficulty in their prediction – especially in older structures, possibly equipped with little monitoring equipment – justifies their inclusion in this section.

While internal erosion can follow earthquakes or be caused in the wake of a large flood, it can also be initiated during normal reservoir operation cycles.

5.2.3 Evaluating risks associated with dams using the Multi-Risk (GenMR) framework

The implementation of the GenMR framework in the evaluation of risks associated with a large embankment dam was based on basic set of elements that can be used to describe a dam system (dam and foundation, spillway, bottom outlet, and hydropower system) and on the main natural hazards that might affect it (earthquakes, floods and internal erosion). In addition to these hazards, the possibility of malfunctions of the bottom outlet and hydropower system were accounted for.

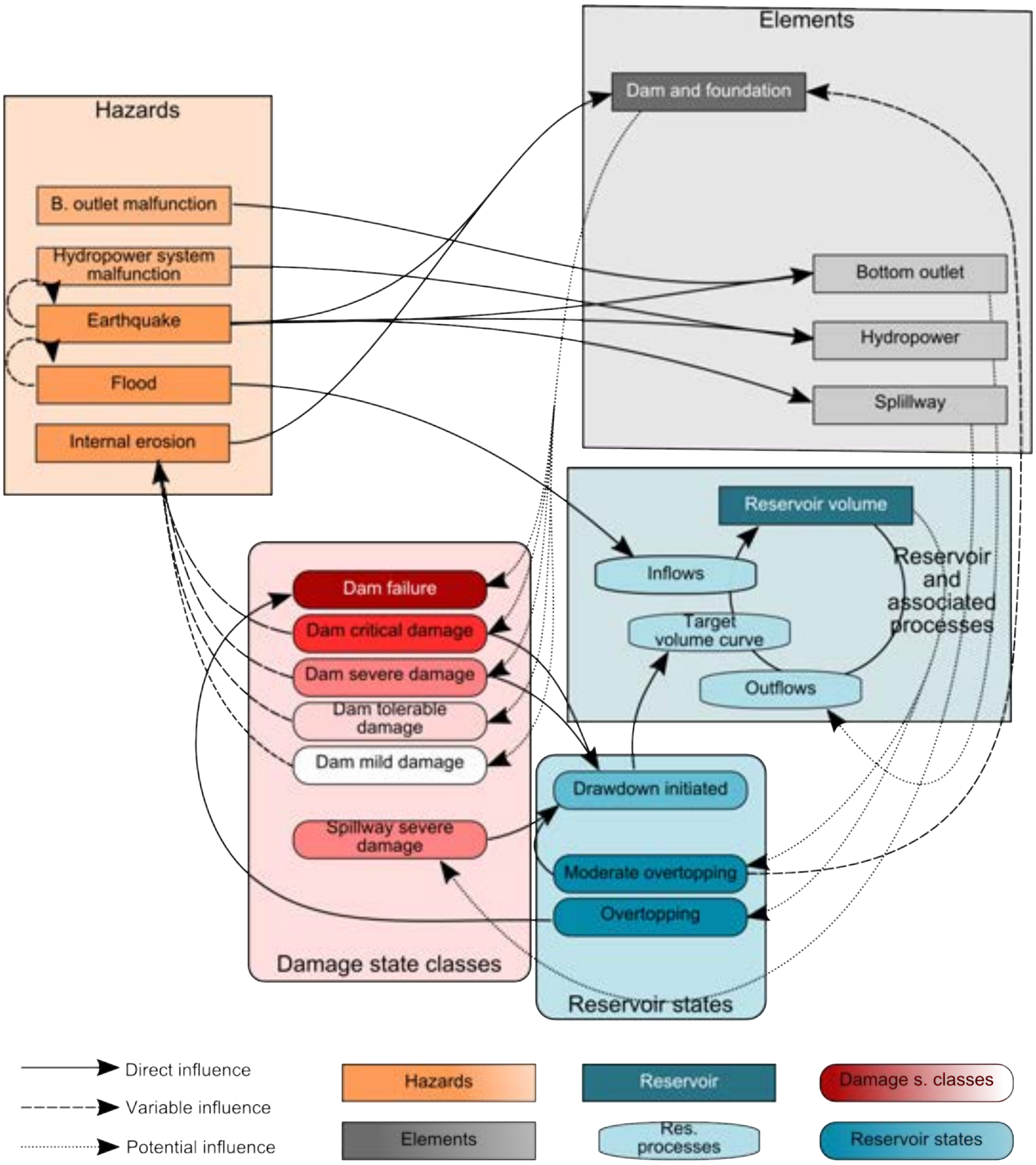
Elements
Dam and foundation
Hazards
B. outlet malfunction
Hydropower system malfunction
Earthquake
Flood
Internal erosion
Bottom outlet
Hydropower
Spillway
Reservoir volume
Inflows
Target volume curve
Outflows
Reservoir and associated processes
Dam failure
Dam critical damage
Dam severe damage
Dam tolerable damage
Dam mild damage
Spillway severe damage
Damage state classes
Drawdown initiated
Moderate overtopping
Overtopping
Reservoir states
Direct influence
Variable influence
Potential influence
Hazards
Reservoir
Damage s. classes
Elements
Res. processes
Reservoir states

Fig. 5.1 Scheme of hazards, elements, system states, and interactions considered in the application of the GenMR framework to large dams

The base concept was extended in order to allow for the simulation of the reservoir through a mass balance equation. Taking full advantage of the GenMR framework, intra- and inter-hazard relationships were represented. In addition, through the specification of a number of “state” events, the complex interdependencies between hazards, system elements, and reservoir were modelled. A scheme of these interdependencies is presented in Fig. 5.1.

The reservoir processes and system states are of particular interest. Expected inflows, with seasonality characteristic of alpine watersheds, were accounted for. In the event of floods, those inflows are increased according to a synthetic flow hydrograph for the duration of the event. Once the reservoir is disturbed, outflow operations endeavour to gradually return it to the “target” volume curve. The outflows are, however, limited by the integrity of the outlet structures and their discharge capacity (function of the damages potentially endured and the reservoir level).

The dam and foundation element can be associated with four distinct damage states prior to failure. As the severity of the damage increases, so does the associated probability of internal erosion events.

In order to avert a possible dam failure and control effects downstream, operators can take the decision of attempting the drawdown or release of the reservoir. It is assumed that the drawdown is initiated once severe or critical dam and foundation damages are present. Also, severe damages to the spillway prompt the drawdown.

Finally, if the reservoir level rises over the dam’s crest, a moderate overtopping effect takes place. The moderate overtopping leads to the partial damaging of the dam structure, but by itself it does not provoke a breach formation. If water continues to rise, a “critical” overtopping of the dam is simulated. Now it is assumed a breach is formed. Its direct consequence is the progressive collapse of the dam through erosion of its body.

5.3 EXPLORATORY APPLICATION TO A REPRESENTATIVE DAM

5.3.1 Introduction

As mentioned previously, the GenMR framework was adapted in order to represent a conceptual embankment dam inspired on the many infrastructures situated on the Swiss Alps. It can be regarded as a large storage dam whose main purpose is hydropower production. It is not influenced by significant hydraulic structures upstream.

In the following subsections, the hazards that potentially affect the system will be quantified and its physical elements described. Albeit the system is conceptual, it was endeavoured that hazards, physical elements, and their interactions are realistic.

5.3.2 Characterization of hazards

5.3.2.1 Earthquakes

The earthquake hazard was quantified with basis on the Swiss dam safety regulations (OSOA*, Ordonnance sur la Sécurité des Ouvrages d’Accumulation*) (Federal Office for Water and Geology 2002). In order to do so, Medvedev-Sponheuer-Karnik (MSK) intensities of ground shaking for return periods of 1 000, 5 000, 10 000 were quantified and used to fit a law in the form of equation (5.2) where I_{MSK} represents the ground shaking intensity, T stands for the return period, and a and b are constants.

$$I_{MSK} = \left(\frac{\ln T}{b}\right)^{a} \tag{5.2}$$

From the ground shaking intensity, the Peak Ground Acceleration (PGA) was derived using equation (5.3), preconized in the OSOA.

$$PGA = 10^{[0.26 \cdot I_{MSK} - 1.81]} \tag{5.3}$$

The resulting laws are illustrated in Fig. 5.2 and Fig. 5.3 as a function of the return period of the earthquake.

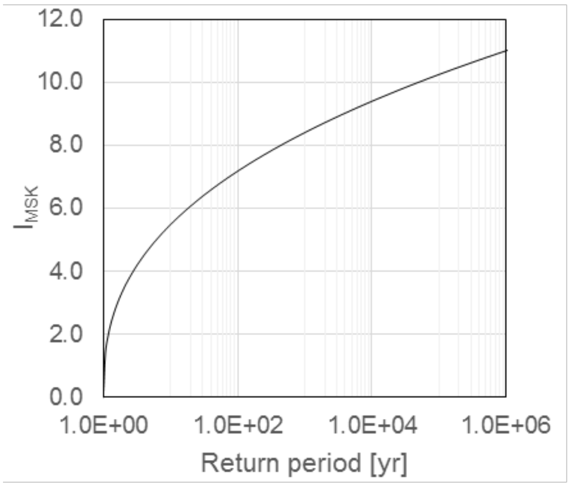

Fig. 5.2 Medvedev-Sponheuer-Karnik (MSK) intensities of ground shaking admitted for the area under study

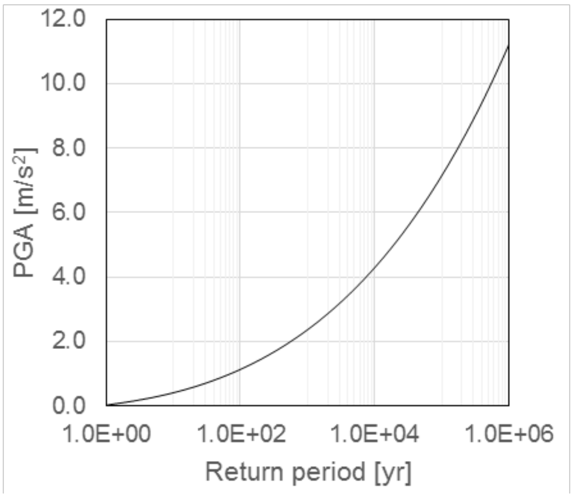

Fig. 5.3 Peak ground accelerations (PGA) admitted for the area under study

Although the method proposed in the OSOA documentation is aimed at dam design, not necessarily being the best option for a risk assessment effort, at the present state its adoption is enticing as large dams in Switzerland have been evaluated in regard to it. Facing present the lack of accurate vulnerability functions generically applicable to large dams, the possibility of comparing the vulnerability curves put forward below with a reference earthquake that the system was designed to withstand is interesting.

Interactions between earthquake events of different frequency were modelled resorting to equation (2.6). The time shifts induced by event i on event j, ΔT_{ij}, were assumed proportional to the return period of event i such that $\Delta T_{ij} = \pm 0.01 T_i$. For a more physical approach to earthquake interactions, see Section 4.

5.3.2.2 Floods

Flood hazard was quantified assuming a high altitude catchment of 50 km^2. The probability of the peak discharge was modelled using the Generalized Extreme Value (GEV) distribution, described by equation (5.4). The GEV distribution is a common option to probabilistically represent peak discharges.

$$F(x|\mu,\sigma,\xi) = e^{\left(-\left[1+\xi\left(\frac{x-\mu}{\sigma}\right)\right]^{-1/\xi}\right)} \tag{5.4}$$

The parameters of the distribution are μ (location), σ (scale), and ξ (shape). The admitted extreme discharge distribution is presented in Fig. 5.4.

Beyond the peak discharge, a time distribution must be associated with the flood event in order to allow for the computation of flood volumes and their influence on reservoir levels.

Peak discharges and flood duration can display very low correlations. As such, the duration of the flood was considered independent from its peak discharge. Based on historical records of floods in an alpine catchment of similar characteristics to the one envisaged in this conceptual case, a probability density for the flood's duration was approximated using the lognormal distribution (Fig. 5.5). Based on the same record, a normalized hydrograph, specifying the time distribution of the flood event, was computed (Fig. 5.6).

Finally, it was assumed that the probability of a flood event taking place is not constant throughout the year. In a simplified manner, it was assumed that the distribution of flood events throughout the year follows roughly the distribution of discharges inflowing to the dam. This distribution is represented in Fig. 5.7.

Interactions between flood events of different return periods were also modelled resorting to equation (2.6). Interactions for floods were, however, constrained from lower to higher probability events. The time shifts induced by event i on event j, ΔT_{ij}, were now assumed proportional to the return period of event i such that $\Delta T_{ij} = -0.001 T_i$ if $T_i > T_j$ and 0 otherwise.

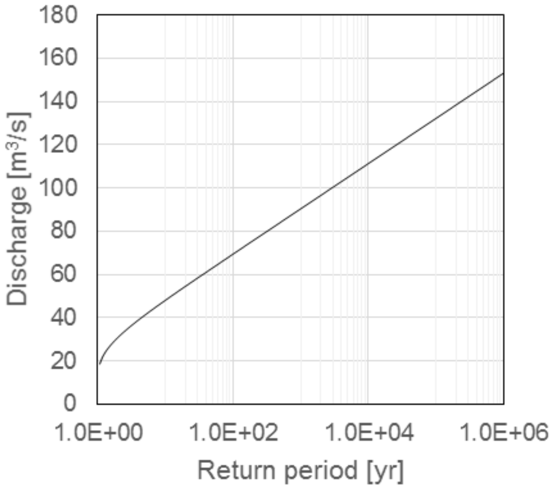

Fig. 5.4 Peak flood inflows to the reservoir

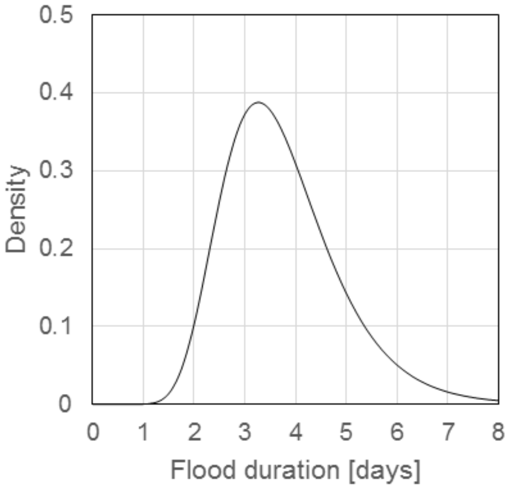

Fig. 5.5 Probability density of a flood's duration

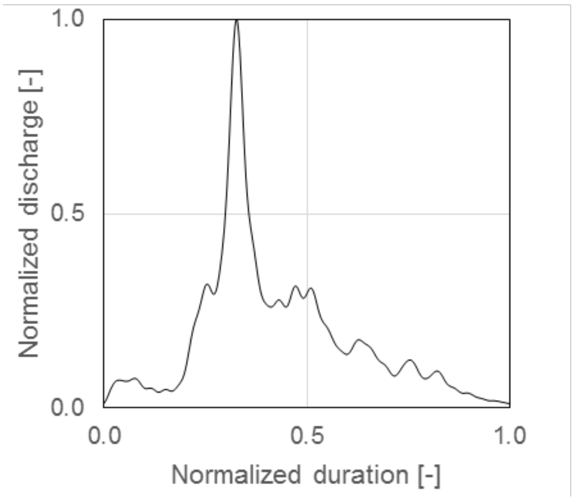

Fig. 5.6 Normalized hydrograph of flood inflows

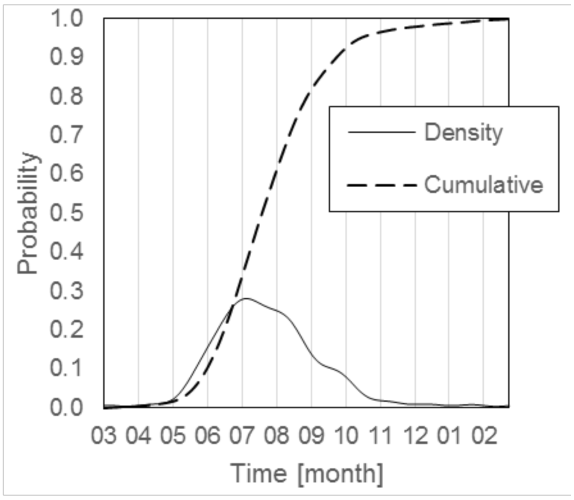

Fig. 5.7 Admitted probability of occurrence of a flood throughout the year

5.3.2.3 Internal erosion and seepage

The quantification of the internal erosion hazard in embankment dams is complex due to the multiple factors that affect its occurrence (e.g. foundation material, dam composition and design, quality of the construction, reservoir levels, or maintenance standards) and the relatively small historical record of internal erosion episodes in large dams (conditioning the employment of statistical approaches). Frameworks for its inclusion in probabilistic risk assessments have, however, been developed (Altarejos-Garcia et al. 2014)

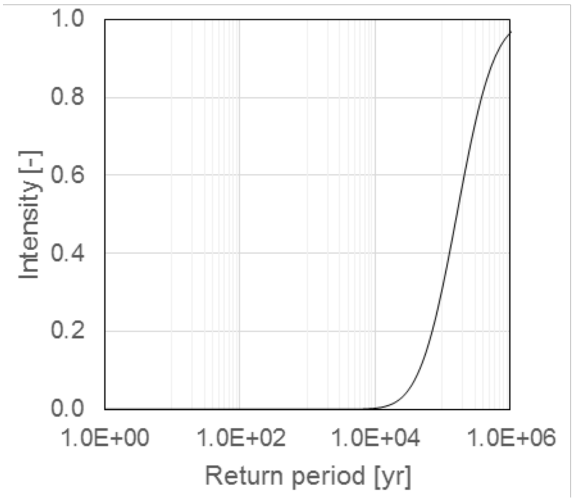

Fig. 5.8 Intensity of internal erosion events admitted for the dam under study

Expert judgement was used to quantify the phenomenon resorting to the cumulative lognormal distribution. The resulting law is illustrated in Fig. 5.8. In its derivation it was assumed that the conceptual dam structure and foundation present a large factor of safety regarding internal erosion and that it was designed, built and operated following state-of-the-art practices.

5.3.3 Characterization of system elements

5.3.3.1 Dam and foundation

Within the customized GenMR framework elements are represented by a number of attributes. Relevantly, these attributes should include the vulnerability functions of the element to different hazards, its recovery rate when damaged, and the definition of associated damage states.

For the dam and foundation element, the vulnerability to earthquake events was assumed to be only a function of PGA. Plotted against the return period of the earthquake, the resulting damage to the element is modelled according to a cumulative lognormal distribution function and presented in Fig. 5.9. As can be seen, 10% damage was assumed for a 10 000 return period earthquake, which is coherent with design standards.

The vulnerability to internal erosion was considered proportional to the hazard intensity as a simplification.

The recovery rate of the dam and foundation element is of 30% damage per year (in other words, a dam with a damage of 30% would take one year to be fully repaired).

Damage states of the dam were quantified as following: mild damage]5, 10%], tolerable damage]10, 20%], severe damage]20, 30%], critical damage]30, 50%], and failure >=50%. Possible split lines associated with these are exemplified in Fig. 5.10. The damage states induce shifts, ΔT_{ij}, on the return periods of internal erosion events. The shifts range from $-0.2T_j$, in the case of mild damage, to $-0.9T_j$, in the case of critical damage.

Finally, moderate overtopping events lead to random damages to the dam and foundation element. These are uniformly distributed from 5 to 20%.

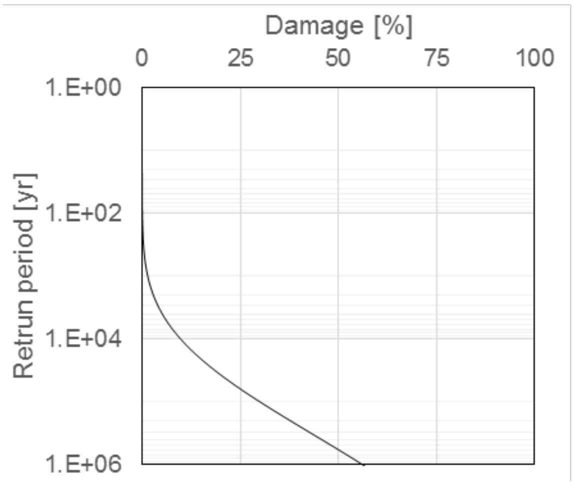

Fig. 5.9 Vulnerability curve of the dam and foundation to earthquakes

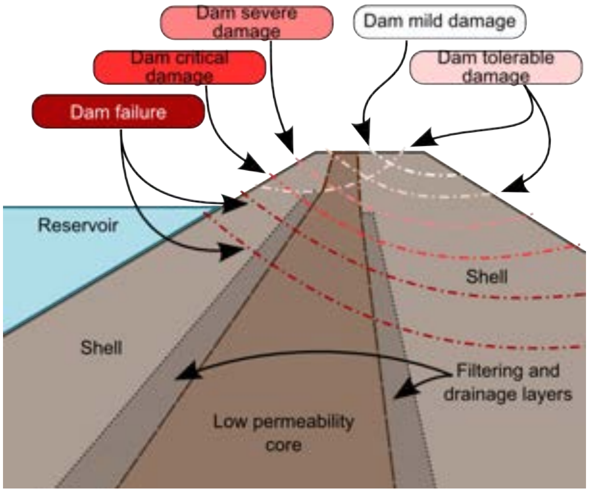

Fig. 5.10 Illustration of possible slip lines corresponding to the admitted dam damage states

5.3.3.2 *Spillway*

Without moving parts, the spillway was considered to be solely affected by earthquakes. Its vulnerability curve, illustrated in Fig. 5.11, is also based on a cumulative lognormal distribution function. The recovery rate of the spillway is of 67% per year (full reparation of the spillway is assumed to require 1.5 years).

Initially, the discharge capacity of the spillway is linearly reduced in proportion to the damage it displays. For damages over 15%, it was arbitrarily considered as no longer functional.

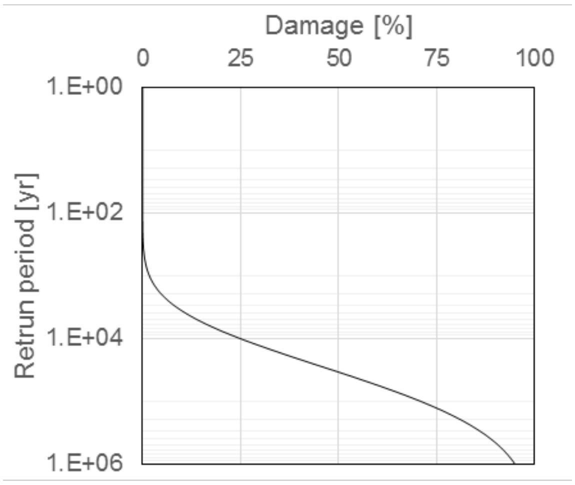

Fig. 5.11 Vulnerability of the spillway element to earthquakes

5.3.3.3 *Bottom outlet*

The bottom outlet behaves similarly to the spillway. Its vulnerability curve to earthquakes is depicted in Fig. 5.12. Being comprised of moving parts, the bottom outlet can suffer from malfunctions that impair its operation (Fig. 5.13).

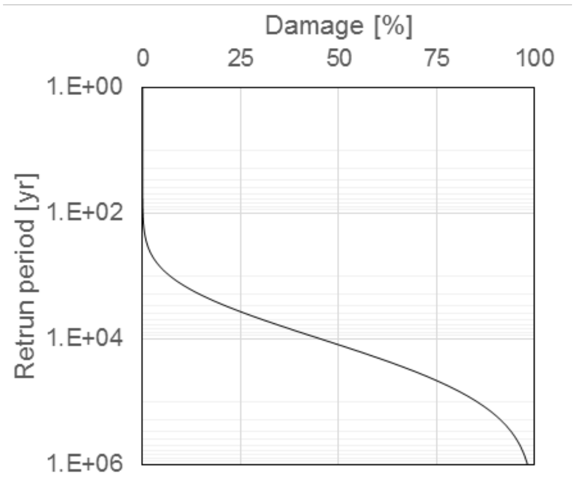

Fig. 5.12 Vulnerability of the bottom outlet element to earthquakes

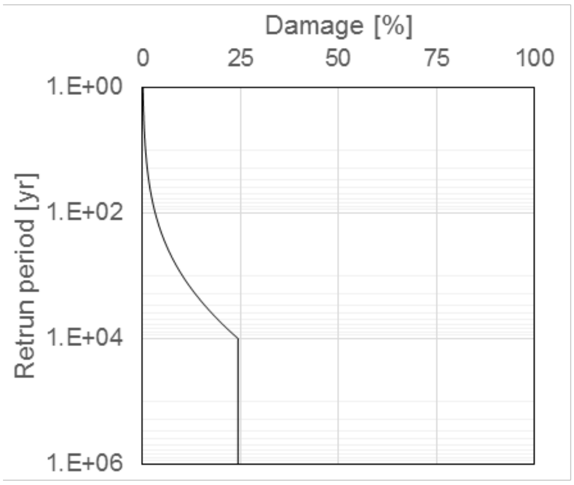

Fig. 5.13 Distribution of the damage induced to the bottom outlet element by equipment malfunction

Malfunctions can take place without the need for a triggering event. They were estimated based on the analyses of failure frequencies observed for gates and valves at dams (Pohl 2000).

The recovery rate of the bottom outlet was arbitrarily fixed at 400% per year. The element's outflow capacity is also reduced proportionally to the damage. It was assumed that no outflow is possible while the element remains damaged beyond 10%.

5.3.3.4 Hydropower system

The hydropower system's representation is conceptually similar to that of the bottom outlet. Its vulnerability curves evidence, however, slightly less resistance to earthquakes (Fig. 5.14), and a higher propensity for equipment malfunctions (Fig. 5.15).

The recovery rate of the hydropower system was set at 100% per year. Its outflow capacity is gradually diminished as damage amounts to 50%, value over outflows stop.

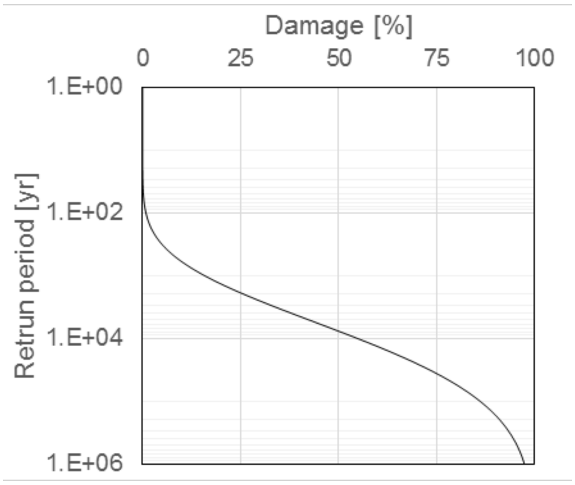

Fig. 5.14 Vulnerability of the hydropower system to earthquakes

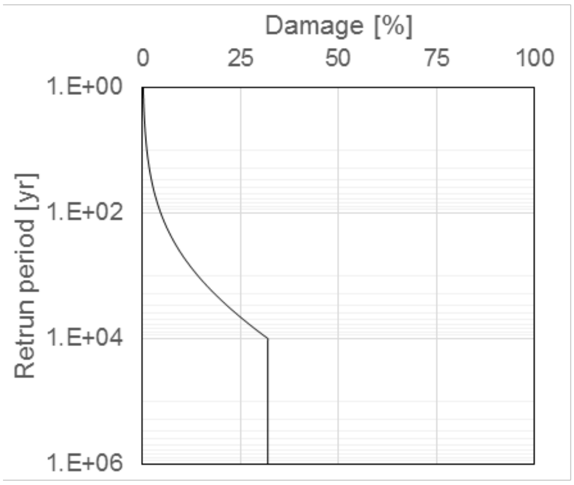

Fig. 5.15 Distribution of the damage induced to the hydropower system by equipment malfunction

5.3.3.5 Reservoir

The reservoir is represented by a particular type of element. Its response to hazards is not modelled using vulnerability functions, being instead simulated as a dynamical system according to equation (5.5). At each time step, t, the variation of the reservoir volume, V, is equal to the difference between gross inflows, $I(t)$ – a function of the time of the year –, and gross outflows, $O(\delta,\omega,V)$ – dependent on the damage state of relevant elements, δ, operational decisions, ω, and V.

$$\frac{dV}{dt} = I(t) - O(\delta,\omega,V) \tag{5.5}$$

The conceptual reservoir was assumed to display an operational storage volume of 100 Mm^3. Expected inflows, from March to February, are illustrated in Fig. 5.16.

A target volume curve is followed whenever inflows and outflow capacities allow it. When the simulated volume, V_{sim}, departs from the target volume, V_{tar}, at a given time step, the dam operation will attempt to outflow O_{att} according to equation (5.6). In the same equation α is the number of days to meeting for V_{sim} to match V_{tar} from the end of the inflow perturbation. Δt represents the time step used in the calculations.

$$O_{att} = \frac{V_{sim} - V_{tar}}{\alpha} \cdot \Delta t \qquad (5.6)$$

The adopted target volume curve is represented in Fig. 5.17. Values are normalized by the volume at which the spillway begins its operation. Moderate overtopping starts to take place at a normalized volume of 107%. The overtopping event, directly leading to dam failure, starts at a normalized volume of 107.2%.

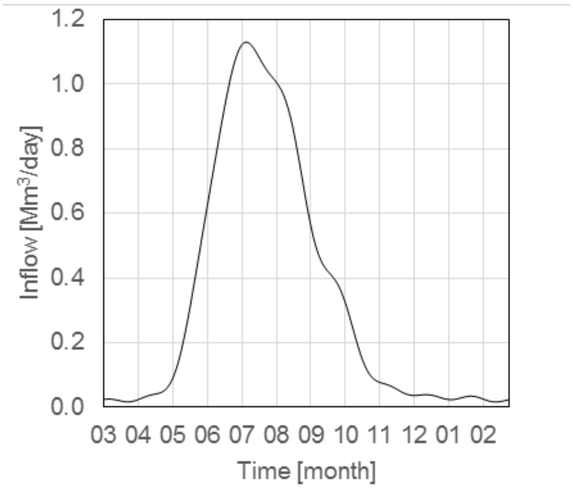

Fig. 5.16 Expected inflows into the reservoir

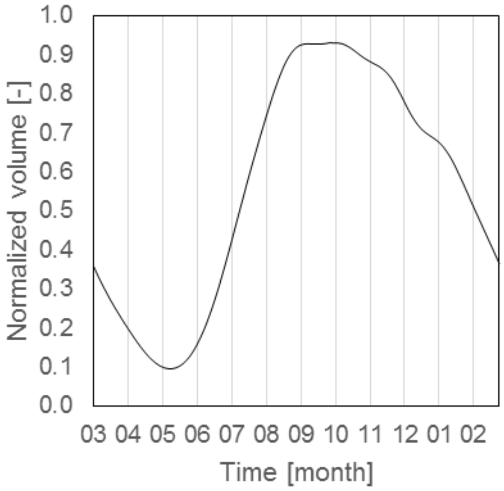

Fig. 5.17 Target volume of the reservoir throughout the year. Normalized in respect to the volume of the reservoir at the spillway level

The simulated outflow is not always equal to O_{att}. On the one hand it is constrained by the maximum outflow capacity of the system and, on the other hand, it is subject to minimum outflows over the spillway and dam crest (which are considered uncontrolled).

The flow through the hydropower system is controlled by hydraulic machinery and electricity demand. The maximum discharge, however, was admitted to be mostly driven by continuous headlosses throughout the system.

In very simplified terms, the bottom outlet's discharge was modelled according to equation (5.7), where C is a coefficient, A is the cross-section area of the outlet, g is the gravity acceleration, and H is the water head over the outlet.

$$Q = CA\sqrt{2gH} \qquad (5.7)$$

Spillway and crest discharges were modelled following equation (5.8), where C is another coefficient, b represents the width of the flow, and H is the water head of the spillway or crest.

$$Q = Cb\sqrt{2gH^3} \tag{5.8}$$

H can be related to the height of water in the reservoir. In order to compute it for any reservoir volume, a quadratic law was admitted (5.9). In it a, b, and c are constants.

$$V = a \cdot h^2 + b \cdot h + c \tag{5.9}$$

The maximum discharges associated with each element for a given reservoir volume can be inspected in Fig. 5.18.

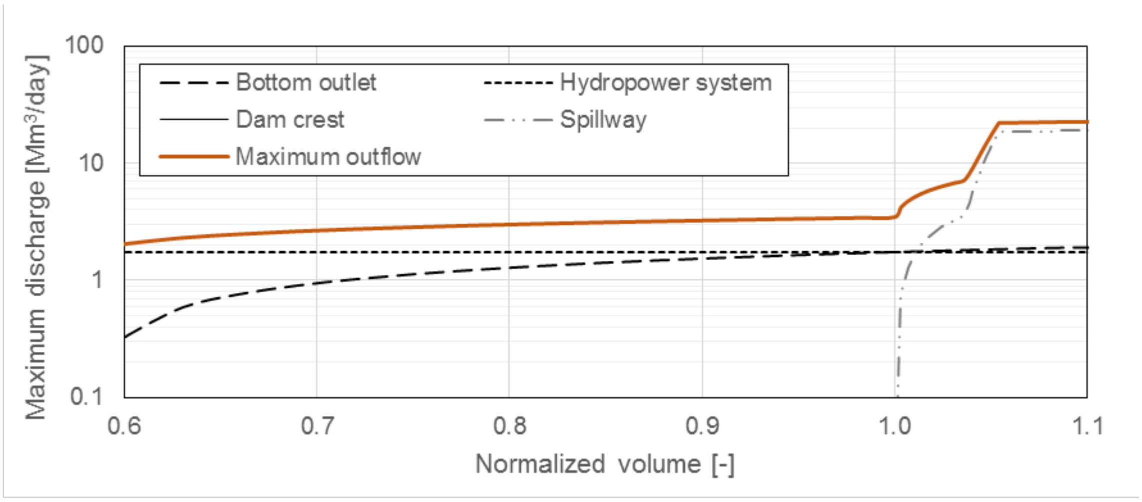

Fig. 5.18 Maximum outflows of the reservoir as a function of the normalized volume of the reservoir

5.4 RESULTS AND DISCUSSION

5.4.1 Analysis of system responses

Having specified all the information needed in order to define the dam system, a large number of simulations were carried out. These included both randomly generated sequences of events and examples of particular importance. Below, the results of three revealing simulations are discussed.

One interesting simulation to inspect roughly reproduces the deterministic verification of the system's response to an extreme earthquake (t=10 000 yr), followed by a rare flood (arbitrarily set at T=316 yr). The simulation results can be seen in Fig. 5.19. On top, the time series of reservoir target and simulated volumes can be compared. Also, the timing of events is indicated. In the middle, the time series of damages to the different physical elements are plotted. Finally, on the bottom, maximum, expected, and simulated discharges are shown.

As can be seen, a drawdown attempt followed the initial earthquake due to substantial damages on the spillway, bottom outlet, and hydropower system, however, the drawdown was delayed. Natural inflows, to which the rare flood was added, contributed to raise the reservoir volume to alarming levels, near the crest. The progressive recovery of the elements, however, eventually restored the outflow capacity needed to accomplish the reservoir drawdown.

Among the simulations there were some that led to dam failure. One such case is presented in Fig. 5.20.

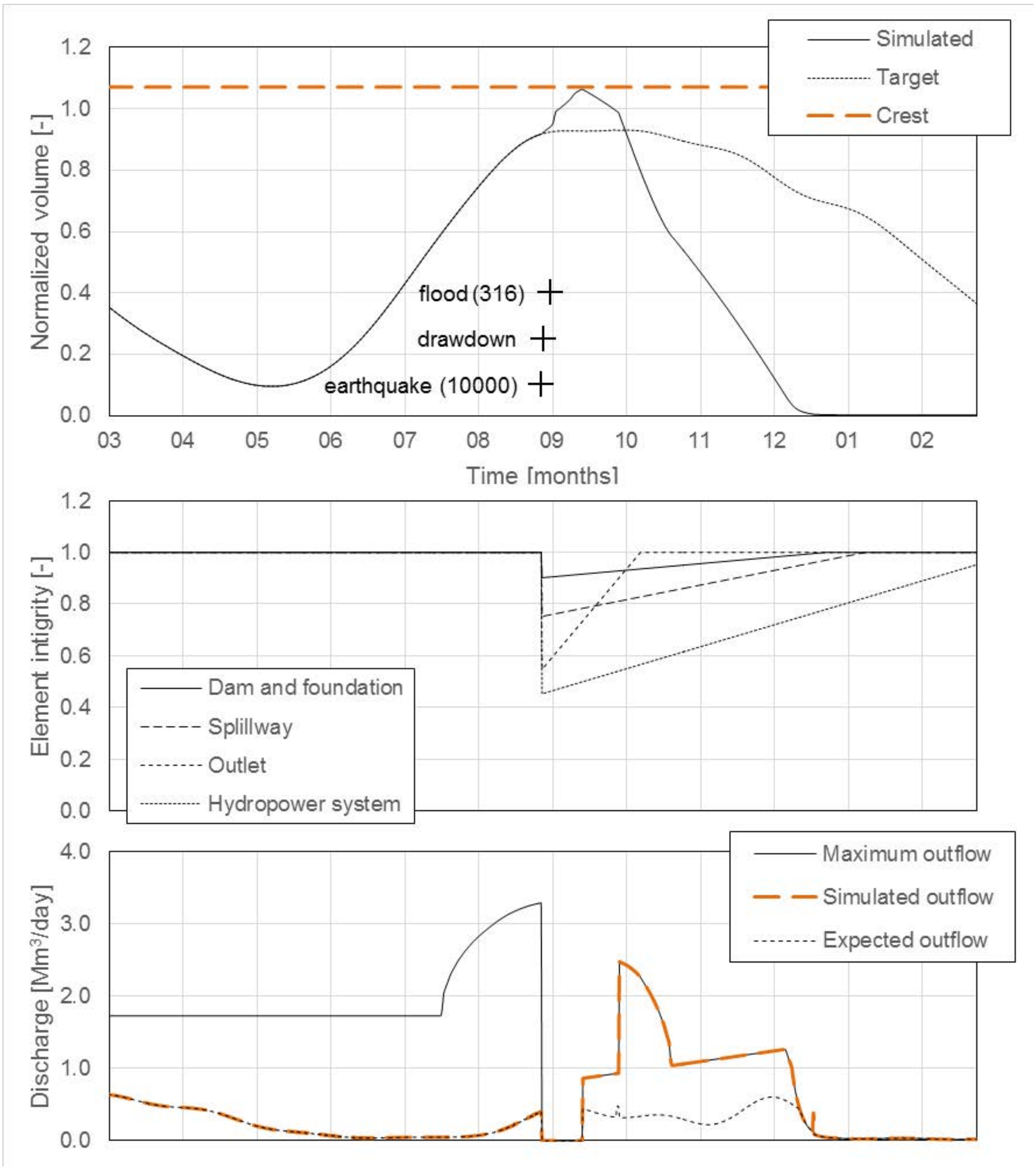

Fig. 5.19 Illustrative response of the system to a design earthquake (T=10 000 yr) and associated flood (T≈316 yr).

In this case, an extreme earthquake with return period of 31 600 years occurred in late August, as the reservoir attained its maximum volume. The damage suffered by the appurtenant structures led, again, to the reduction of the outflow capacity and a drawdown attempt failed to avert, first, a moderate overtopping (which caused some damage to the dam and foundation element) and, eventually, to a critical overtopping that prompted the failure of the dam.

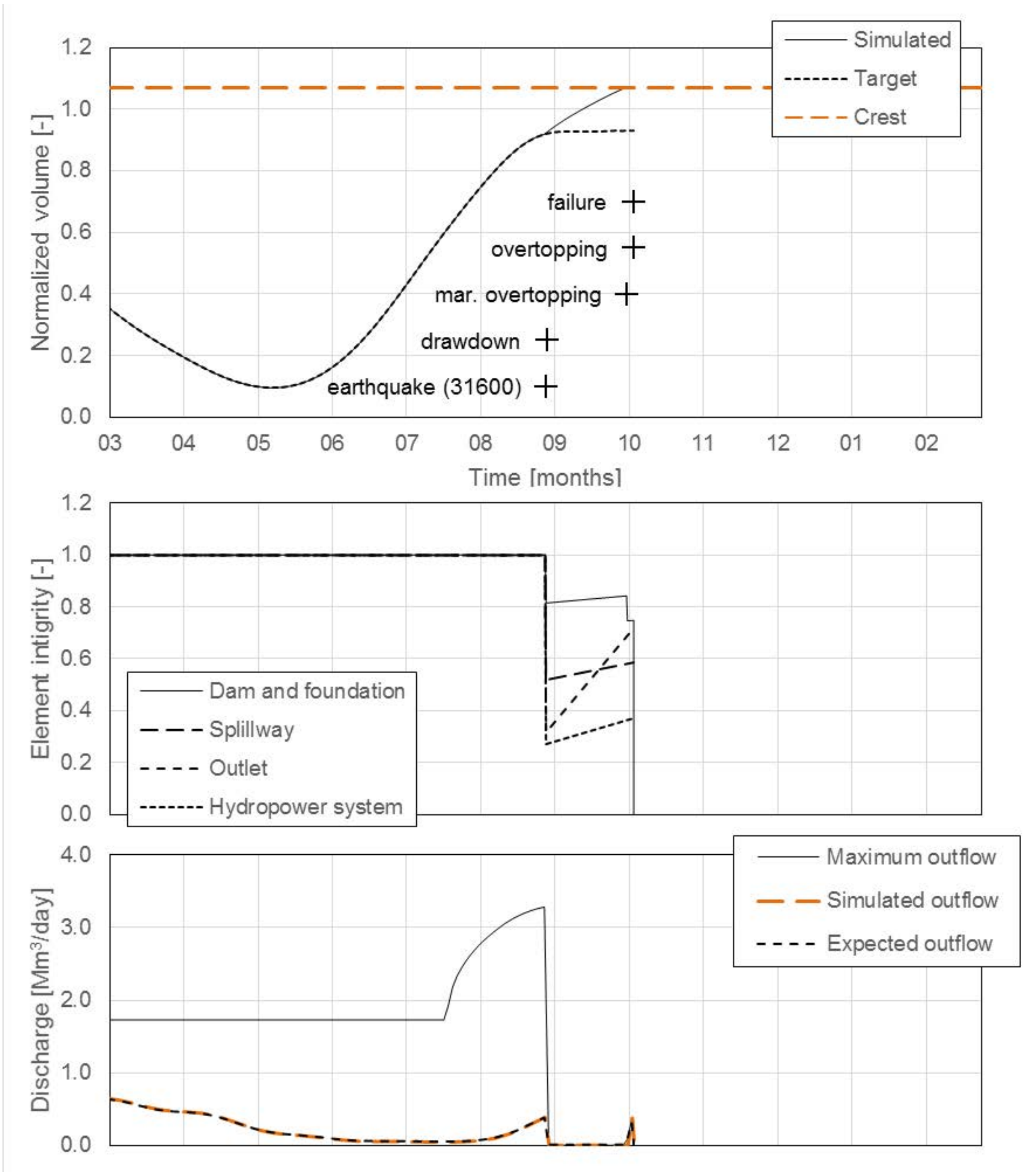

Fig. 5.20 Illustrative response of the system to an extreme earthquake (T≈31 600 yr), leading to overtopping and consequent dam failure

A final example, shown in Fig. 5.21, illustrates a case where the failure mechanism is not overtopping, but damage brought about by internal erosion. Again, it is a 31 600 years return period earthquake that serves as a trigger. Following that event, two related earthquakes, with return periods of 316 and 1 000 years, affected the system. Finally, an internal erosion event with return period of 31 600 (whose probability of occurrence had been increased by the previous earthquakes) led to the failure of the structure.

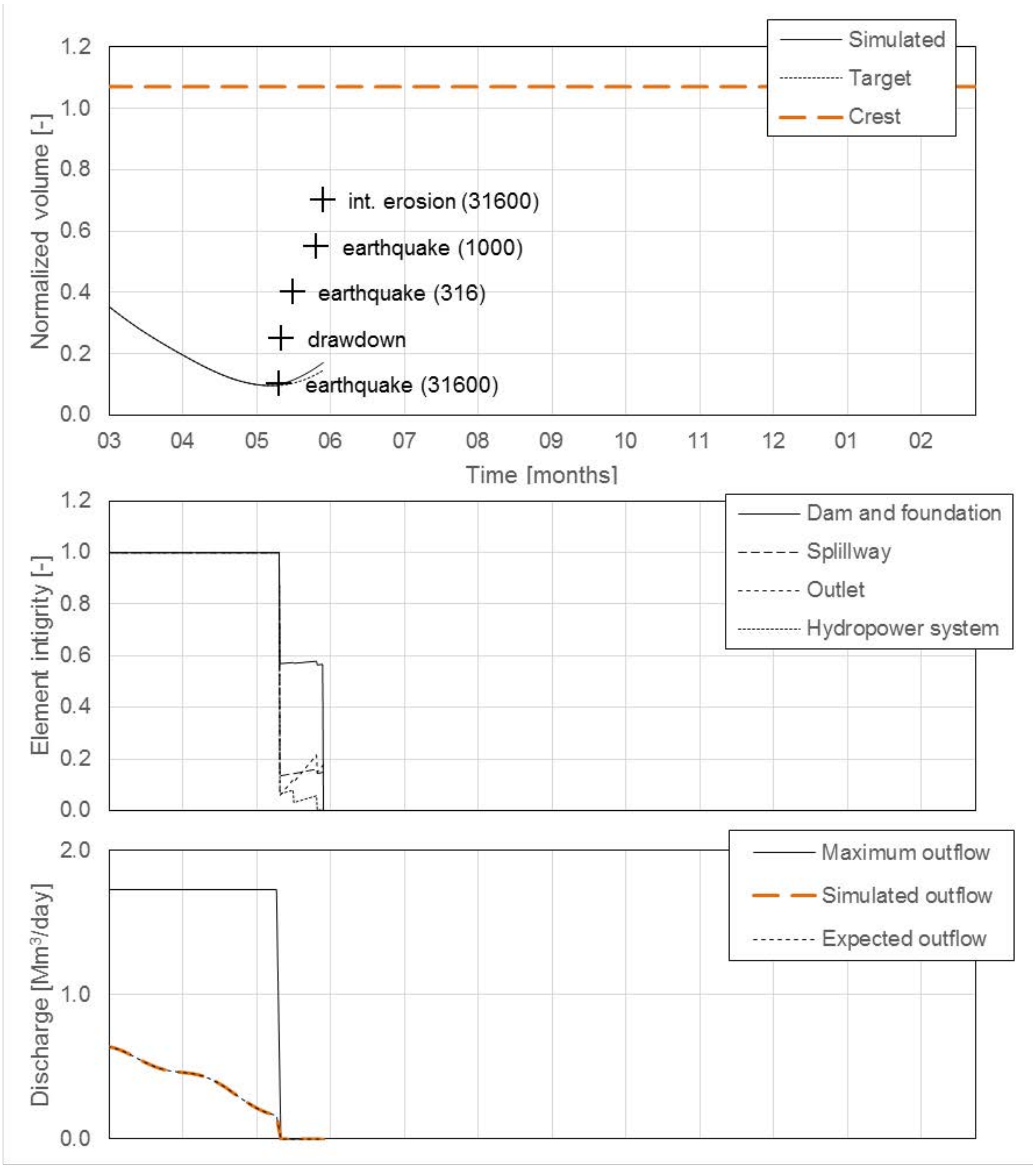

Fig. 5.21 Illustrative response of the system to clustering of extreme earthquakes (trigger with T≈31 600 yr), leading an event of internal erosion and dam failure

5.4.2 On the influence of hazard interactions

The results presented herein correspond to a conceptual system. While interpreting results, it is essential to acknowledge that the system modelled here does not correspond to a real infrastructure. It represents no more a conceptual dam created in order to illustrate a practical application of the GenMR framework. In comparison to a real case, some of the assumptions that were made might, therefore, be exaggerated or skewed.

In total, over 12 million simulations encompassing one year of the dam's operation were conducted. One half accounted for hazard interactions while the other half did not.

When comparing aggregated results from the simulations that accounted for hazard interactions and the simulations that did not, the system failure probabilities increased (from 7.9×10^{-6} without, to 1.2×10^{-5} with hazard interactions). Despite the increase in risk that is prompted by accounting for hazard interactions, both failure probabilities appear comfortably beyond the safety criteria recommended for large dams which, for single hazards, approach probabilities of occurrence of 10^{-4}.

While earthquake and flood events' probabilities have not changed appreciably between both cases, the rates of extreme internal erosion episodes where significantly higher when hazard interactions were accounted for. This difference was only evident for return periods well over 10 000 years (see Table 5.1). Notwithstanding, changes in the occurrence rate of extremely low probability internal erosion events prompted a significant increase in the overall failure probability of the system.

In fact, an analysis of events leading to failure highlighted that, for the conceptual system as it was set up, earthquakes were the main hazard leading to dam failure (present in nearly 60% of the failure events). Triggered by earthquakes, episodes of internal erosion, individually responsible for approximately 30% of the failures, gained relevance.

Table 5.1 Comparison between theoretical and simulated return periods for internal erosion events.

Theoretical	No interactions	Interactions
1.00E+02	9.99E+01	1.01E+02
3.16E+02	3.14E+02	3.15E+02
1.00E+03	1.00E+03	9.98E+02
3.16E+03	3.04E+03	3.20E+03
1.00E+04	9.66E+03	9.60E+03
3.16E+04	3.18E+04	2.69E+04
1.00E+05	9.55E+04	7.41E+04
3.16E+05	3.71E+05	1.54E+05

The analysis conducted herein needs to be refined with respect to the underlying hazard, damage, and functionality loss assumptions prior to future application to real infrastructures. Despite this, the findings from this conceptual system analysis point towards the fact that dams are extraordinarily safe structures with very low failure rate.

5.5 CONCLUSIONS

The GenMR framework provides a computationally performing, general, and conceptually elegant way to simulate multi-hazard interactions affecting large dams.

Here, but a fraction of the possible interactions and processes that might take place during the lifetime of a large dam were included. Even the features of the system that were accounted for, were so in a simplified manner. On the one hand, this simplicity can be considered desirable in the light of the uncertain information on vulnerability curves and hazard characterization (particularly when interactions come into play and when a significant share of the risk can be associate with very low occurrence probability events). On the other hand, by oversimplifying one can inadvertently underrepresent important phenomena and thus prepare an intrinsically flawed depiction of the system.

In the conceptual system studied here, but also in an application to a real large dam, uncertainties stemming from the GenMR simulations will be very large. In order to render absolute results reliable, a substantial investment should be made in order to quantify the main hazards (including the ones with extremely low occurrence probabilities) and their interactions. Additionally, the range of physical elements that play a relevant role in the system should be adequately individualized and described.

Even when accurate quantifications of hazards or detailed information on system components is not available, the GenMR can potentially be useful. In fact, even a relatively coarse representation of system such as the one reported in this section can be used in order to gain insight on preferential failure mechanisms.

Next steps on the application of the framework to dams should include the possibility to specify relationships dependent on more than one parameter (e.g. internal erosion occurrence rates should be influenced at least by reservoir levels and prior earthquakes). Also, the inclusion of additional hazards (e.g. mass slides) in the analysis ought to be pursued. Finally, an enticing development would be to extend the simulation in order to account for losses; not only the ones associated with the dam system, but also with the potentially affected areas downstream, where a large share of the risk is known to lie.

6 General Conclusions

We showed in the present report three examples of hazard interactions potentially leading to low-probability–high-consequences risk scenarios. The three cases illustrated the variety of possible interaction processes, such as earthquake rupture cascading (Section 3), earthquake clustering (Section 4) and combinations of natural and operational hazards at a dam (Section 5). We integrated two of these cases within the Generic Multi-Risk (GenMR) framework (Mignan et al., 2014) using the concept of hazard correlation matrix (HCM). While earthquake rupture cascading (intra-event interaction) was not described in a HCM, cascading ruptures could be implemented in GenMR by considering these extreme events in the GenMR stochastic event set. We validated the GenMR framework by demonstrating its usability and flexibility. A summary of our results is given below:

- **Extreme earthquakes characterized by long rupture lengths** have been assessed from the concepts of dynamic stress interactions (Mignan et al., in press, a). Such events are not yet considered in the standard seismic hazard models. In a stress test perspective, they lead to a **longer tail of the frequency-magnitude distribution of earthquakes**;
- **Earthquake clustering** has been assessed from the theory of Coulomb stress transfer. Earthquake clustering leads to a **migration of risk towards low-probability–high-consequences multi-risk scenarios (fat tail)**;

- **Interactions within and between natural and operational hazards at dams** have been assessed from a combination of empirical models. **Combinations of events increase the risk of dam failure relative to no hazard interaction scenarios, but such combinations are likely to remain in the beyond-safety-design scenario range**.

Let us note that the conclusions of this report pertain to conceptual/fictitious infrastructures and not directly to the specific critical infrastructures of the STREST project, which are characterized in other work packages. Although the GenMR method was here only tested for multi-hazard analysis, it can also include multi-risk elements (e.g., interactions within the infrastructure, time-variant vulnerability) and it additionally provides an innovative approach to the visualization and selection of risk scenarios (i.e. risk migration matrix, RMM). We thus suggest the GenMR method to be a part of the stress test methodology developed in the STREST project.

References

Adachi, T. and B. R. Ellingwood (2008), Serviceability of earthquake-damaged water systems: Effects of electrical power availability and power backup systems on system vulnerability, Reliab. Eng. Syst. Saf., 93, pp. 78-88

Aki, K. (1966), Generation and Propagation of G Waves from the Niigata Earthquake of June 16, 1964. Part 2. Estimation of earthquake moment, released energy, and stress-strain drop from the G wave spectrum, Bull. Earthq. Res. Inst., 44, 73-88

Akkar, S. and J. J. Bommer (2010), Empirical Equations for the Prediction of PGA, PGV, and Spectral Accelerations in Europe, the Mediterranean Region, and the Middle East, Seismol. Res. Lett., 81, 195-206, doi: 10.1785/gssrl.81.2.195

Altarejos-Garcia, L., F. Silva-Tulla, I. Escuder-Bueno, and A. Morales-Torres (2014). Practical risk assessment for embankments, dams, and slopes.in K.-K. Phoon and J. Ching, editors. Risk and Reliability in Geotechnical Engineering. CRC Press

Ambraseys, N. N. (1970), Some characteristic features of the Anatolian Fault Zone, Tectonophysics, 9, 143-165

Anderson, J. G., S. G. Wesnousky and M. W. Stirling (1996), Earthquake Size as a Function of Fault Slip Rate, Bull. Seismol. Soc. Am., 86, 683-690

Barka, A. A. and K. Kadinsky-Cade (1988), Strike-slip fault geometry in Turkey and its influence on earthquake activity, Tectonophysics, 7, 663-684

Basili R., et al. (2013), The European Database of Seismogenic Faults (EDSF) compiled in the framework of the Project SHARE, doi:10.6092/INGV.IT-SHARE-EDSF, available at: http://diss.rm.ingv.it/share-edsf/ (last assessed September 2014)

Bhat, H. S., R. Dmowska, J. R. Rice and N. Kame (2004), Dynamic Slip Transfer from the Denali to Totschunda Faults, Alaska: Testing Theory for Fault Branching, Bull. Seismol. Soc. Am., 94, S202-S213

Bhat, H. S., M. Olives, R. Dmowska and J. R. Rice (2007), Role of fault branches in earthquake rupture dynamics, J. Geophys. Res., 112, B11309

Bier, V. M., Y. V. Haimes, J. H. Landert, N. C. Matalas and R. Zimmerman (1999), A survey of approaches for assessment and managing the risk of extremes, Risk Analysis, 19, 83-94

Bilham, R. (2009), The seismic future of cities, Bull. Earthq. Eng., doi: 10.1007/s10518-009-9147-0

Catalli, F., M. Cocco, R. Console and L. Chiaraluce (2008), Modeling seismicity rate changes during the 1997 Umbria-Marche sequence (central Italy) through a rate- and state-dependent model, J. Geophys. Res., 113, B11301

Choi, J.-H., K. Jin, D. Enkhbayar, B. Davvasambuu, A. Bayasgalan and Y.-S. Kim (2012), Rupture propagation inferred from damage patterns, slip distribution, and segmentation of the 1957 M_w 8.1 Gobi-Altay earthquake rupture along the Bogd fault, Mongolia, J. Geophys. Res., 117, B12401, doi: 10.1029/2011JB008676

Comfort, L. K. (2006), Cities at Risk: Hurricane Katrina and the Drowning of New Orleans, Urban Affairs Review, 41, pp. 501-516

Cornell, C. (1968), Engineering seismic risk analysis, Bull. Seismol. Soc. Am., 59, 1583-1606

Cornell, C. A. and H. Krawinkler (2000), Progress and Challenges in Seismic Performance Assessment, PEER Center News, 3(2), 1-4

Darbre, G. R. (1999), Dam risk analysis. Federal Office for Water Management, Switzerland.

Dieterich, J. (1994), A constitutive law for rate of earthquake production and its application to earthquake clustering, J. Geophys. Res., 99, 2601-2618

Duputel, Z., H. Kanamori, V. C. Tsai, L. Rivera, L. Meng, J. P. Ampuero and J. M. Stock (2012), The 2012 Sumatra great earthquake sequence, Earth Planet. Sci. Lett., 351, 247-257, doi: 10.1016/j.epsl.2012.07.017

Eberhart-Phillips, D., et al. (2003), The 2002 Denali Fault Earthquake, Alaska: A Large Magnitude, Slip-Partitioned Event, Science, 300, 1113-1118, doi: 10.1126/science.1082703

ENSI (Swiss Federal Nuclear Safety Inspectorate) (2012), Event sequence Fukushima 11032011, ENSI-AN-7999 Report, 48 pp, available at http://www.ensi.ch/en/2012/08/08/event-sequences-fukushima-11032011/ (last assessed October 2014)

ENSREG (European Nuclear Safety Regulators Group) (2011), Declaration of ENSREG, Annex 1, EU “Stress test” specifications, Brussels 31.05.2011, available at http://www.ensreg.eu/node/289 (last assessed September 2014)

Federal Office for Water and Geology (2002). Sécurité des ouvrages d'accumulation ver. 1.1 - Ordonnance sur la sécurité des ouvrages d'accumulation (OSOA). Directives. FOWG, Biel, Switzerland

FEMA (1998), FEMA 306: Evaluation Of Earthquake Damaged Concrete And Masonry Wall Buildings – Basic procedures manual, Federal Emergency Management Agency, Washington DC, 250 pp.

Field, E. H. (2007), A Summary of Previous Working Groups on California Earthquake Probabilities, Bull. Seismol. Soc. Am., 97, 1033-1053

Field, E. H., et al. (2009), Uniform California Earthquake Rupture Forecast, Version 2 (UCERF 2), Bull. Seismol. Soc. Am., 99, 2053-2107, doi: 10.1785/0120080049

Field, E. H., et al. (2013), Uniform California earthquake rupture forecast, version 3 (UCERF3) – The time-independent model, U.S. Geological Survey Open-File Report 2013-1165, 97 pp., California Geological Survey Special Report 228, and Southern California Earthquake Center Publication 1792, http://pubs.usgs.gov/of/2013/1165/

Fliss, S., H. S. Bhat, R. Dmowska and J. R. Rice (2005), Fault branching and rupture directivity, J. Geophys. Res., 110, B06312

Fujii, Y. and K. Satake (2007), Tsunami Source of the 2004 Sumatra-Andaman Earthquake Inferred from Tide Gauge and Satellite Data, Bull. Seismol. Soc. Am., 97, 5192-5207, doi: 10.1785/0120050613

Ganas, A., Z. Roumelioti and K. Chousianitis (2012), Static stress transfer from the May 20, 2012, M 6.1 Emilia-Romagna (northern Italy) earthquake using a co-seismic slip distribution model, Ann. Geophys., 55, 655-662

Gee, D. M. 2009. Comparison of dam breach parameter estimators.in World Environmental and Water Resources Congress 2009. ASCE, Kansas City, Missouri, USA

Giardini, D., et al. (2013), Seismic Hazard Harmonization in Europe (SHARE): Online Data Resource, doi: 10.12686/SED-00000001-SHARE

Goto, H. and H. Morikawa (2012), Ground motion characteristics during the 2011 off the Pacific Coast of Tohoku Earthquake, Soils and Foundations, 52, 769-779

Gülkan, P. and S. Akkar (2002), A simple replacement for the drift spectrum, Engineering Structures, 24, 1477-1484

Haller, K. M. and R. Basili (2011), Developing Seismogenic Source Models Based on Geologic Fault Data, Seismol. Res. Lett., 82, 519-525, doi: 10.1785/gssrl.82.4.519v

Hanks, T. C. and W. H. Bakun (2002), A Bilinear Source-Scaling Model for **M**-log *A* Observations of Continental Earthquakes, Bull. Seismol. Soc. Am., 92, 1841-1846

Hanks, T. C. and H. Kanamori (1979), A Moment Magnitude Scale, J. Geophys. Res., 84, 2348-2350

Harris, R. A., R. J. Archuleta and S. M. Day (1991), Fault steps and the dynamic rupture process: 2-D numerical simulations of a spontaneously propagating shear fracture, Geophys. Res. Lett., 18, 893-896

Harris, R. A. and S. M. Day (1993), Dynamics of Fault Interaction: Parallel Strike-Slip Faults, J. Geophys. Res., 98, 4461-4472

Harris, R. A. and S. M. Day (1999), Dynamic 3D simulations of earthquakes on en echelon faults, Geophys. Res. Lett., 26, 2089-2092

Harris, R. A., J. F. Dolan, R. Hartleb and S. M. Day (2002), The 1999 Izmit, Turkey, Earthquake: A 3D Dynamic Stress Transfer Model of Intraearthquake Triggering, Bull. Seismol. Soc. Am., 92, 245-255

Hendron Jr, A. J. and F. D. Patton (1987). The Vaiont slide - a geotechnical analysis based on new geologic observations of the failure surface. Engineering Geology 24(1–4):475-491

Holschneider, M., G. Zöller, R. Clemens and D. Schorlemmer (2014), Can we test for the maximum possible earthquake magnitude?, J. Geophys. Res., 119, 2019-2028, doi: 10.1002/2013JB010319

ICOLD (1992). Selection of design flood: current methods. International Comission on Large Dams (ICOLD), Paris

ICOLD (2000). Reservoir landslides: Investigation and management. International Comission on Large Dams (ICOLD), Paris

ICOLD (2001). Design features of dams to resist seismic ground motion: guidelines and case studies. International Comission on Large Dams (ICOLD), Paris

ICOLD (2003). Dams and floods: guidelines and case histories. International Comission on Large Dams (ICOLD), Paris

ICOLD (2012). Bulletin on safe passage of extreme floods. International Comission on Large Dams (ICOLD), Paris

ICOLD (2014). Selecting seismic parameters for large dams: guidelines. International Comission on Large Dams (ICOLD), Paris

Iervolino, I., M. Giorgio and E. Chioccarelli (2014), Closed-form aftershock reliability of damage-cumulating elastic-perfectly-plastic systems, Earthquake Engng Struct. Dyn., 43, 613-625, doi: 10.1002/eqe/2363

Kame, N., J. R. Rice and R. Dmowska (2003), Effects of prestres state and rupture velocity on dynamic fault branching, J. Geophys. Res., 108, 2265

Kameda, H. (2012), Engineering agenda on nuclear safety from the 2011 Tohoku-Pacific earthquake, Proc. Int. Symp. Engin. Lessons learned from the 2011 great East Japan Earthquake, March 1-4, 2012, Tokyo, Japan, 102-121

Kappes, M. S., M. Keiler, K. von Elverfeldt and T. Glade (2012), Challenges of analysing multi-hazard risk: a review, Nat. Hazards, 64, 1925-1958

Kijko, A. and M. Singh (2011), Statistical Tools for Maximum Possible Earthquake Magnitude Estimation, Acta Geophysica, 59, 674-700, doi: 10.2478/s11600-011-0012-6

Kilburn, C. R. J. and D. N. Petley (2003), Forecasting giant, catastrophic slope collapse: lessons from Vajont, Northern Italy, Geomorphology, 54, 21-32

Kim, Y.-S. and D. J. Sanderson (2005), The relationship between displacement and length of faults: a review, Earth-Science Reviews, 68, 317-334

King, G. C. P. (1986), Speculations on the Geometry of the Initiation and Termination Processes of Earthquake Rupture and its Relation to Morphology and Geological Structure, Pageoph, 124, 567-585

King, G. C. P., R. S. Stein and J. Lin (1994), Static Stress Changes and the Triggering of Earthquakes, Bull. Seismol. Soc. Am., 84, 935-953

King, G. C. P. (2007), Fault Interaction, Earthquake Stress Changes, and the Evolution of Seismicity, Treatise on Geophysics, 4, 225-255

Komendantova, N., R. Mrzyglocki, A. Mignan, B. Khazai, F. Wenzel, A. Patt and K. Fleming (2014), Multi-hazard and multi-risk decision-support tools as a part of participatory risk governance: Feedback from civil protection stakeholders, International J. Disaster Risk Reduction, 8, 50-67, doi: 10.1016/j.ijdrr.2013.12.006

Lagomarsino, S. and S. Giovinazzi (2006), Macroseismic and mechanical models for the vulnerability and damage assessment of current buildings, Bull. Earthquake Eng., 4, 415-443, doi: 10.1007/s10518-006-9024-z

Lemperiere, F. 1999. Risk analysis: What sort should be applied and to which dams? International Journal on Hydropower & Dams 6(4):128-132

Leonard, M. (2010), Earthquake Fault Scaling: Self-Consistent Relating of Rupture Length, Width, Average Displacement, and Moment Release, Bull. Seismol. Soc. Am., 100, 1971-1988, doi: 10.1785/0120090189

Lin, J. and R. S. Stein (2004), Stress triggering in thrust and subduction earthquakes, and stress interaction between the southern San Andreas and nearby thrust and strike-slip faults, J. Geophys. Res., 109, B02303

Lipscy, P. Y., K. E. Kushida and T. Incerti (2013), The Fukushima Disaster and Japan's Nuclear Plant Vulnerability in Comparative Perspective, Environ. Sci. Technol., 47, 6082-6088, doi: 10.1021/es4004813

Magistrale, H. and S. Day (1999), 3D Simulations of Multi-Segment Thrust Fault Rupture, Geophys. Res. Lett., 26, 2093-2096

Magliulo, G., M. Ercolino, C. Petrone, O. Coppola and G. Manfredi (2014), The Emilia Earthquake: Seismic Performance of Precast Reinforced Concrete Buildings, Earthquake Spectra, 30, 891-912

Mai, P. M. and G. C. Beroza (2000), Source Scaling Properties from Finite-Fault-Rupture Models, Bull. Seismol. Soc. Am., 90, 604-615

Marques, J. O. D. A. (2005), The Paths of Providence: Voltaire and Rousseau on the Lisbon Earthquake, Cad. Hist. Fil. Co., 15, 33-57

Meletti, C., V. D'Amico and F. Martinelli (2009), Homogeneous determination of the maximum magnitude, SHARE project, D3.1 deliverable, available at http://www.earth-prints.org/bitstream/2122/6530/1/D3.3_SHARE.pdf

Mignan, A., P. Grossi and R. Muir-Wood (2011), Risk assessment of Tunguska-type airbursts, Nat. Hazards, 56, 869-880, doi: 10.1007/s11069-010-9597-3

Mignan, A., S. Wiemer and D. Giardini (2014), The quantification of low-probability–high-consequences events: part I. A generic multi-risk approach, Nat. Hazards, 73, 1999-2022, doi: 10.1007/s11069-014-1178-4

Mignan, A., L. Danciu and D. Giardini, Reassessment of the maximum fault rupture length of strike-slip earthquakes and inference on Mmax in the Anatolian Peninsula, Turkey, Seismol. Res. Lett., in press, a

Mignan, A., N. Komendantova, A. Scolobig and K. Fleming, Multi-Risk Assessment and Governance, in Handbook of Disaster Risk Reduction & Management, Eds. C. N. Madu and C.-h. Kuei, World Scientific Press & Imperial College Press, London, in press, b

Mignan, A., S. Wiemer and D. Giardini, The quantification of low-probability–high-consequences events: part II. Guidelines to multi-risk assessment based on the Virtual City concept, in preparation

Milner, K. R., et al. (2013), Appendix T – Defining the Inversion Rupture Set Using Plausibility Filters, In: Field, E. H., et al. (2013), Uniform California earthquake rupture forecast, version 3 (UCERF3) – The time-independent model, U.S. Geological Survey Open-File Report 2013-1165, 97 pp., California Geological Survey Special Report 228, and Southern California Earthquake Center Publication 1792, http://pubs.usgs.gov/of/2013/1165/

Mueller, K., S. E. Hough and R. Bilham (2004), Analysing the 1811-1812 New Madrid earthquakes with recent instrumental recorded aftershocks, Nature, 429, 284-288

Müller-Salzburg, L. (1987). The Vajont catastrophe - a personal review. Engineering Geology 24(1–4):423-444

Muir-Wood, R. and A. Mignan (2009), A Phenomenological Reconstruction of the Mw9 November 1st 1755 Earthquake Source, in: L. A. Mendes-Victor et al. (eds.), The 1755 Lisbon Earthquake: Revisited, Geotechnical, Geological, and Earthquake Engineering, 7, 121-146

Nalbant, S. S., S. Steacy, K. Sieh, D. Natawidjaja and J. McCloskey (2005), Earthquake risk on the Sunda trench, Nature, 435, 756-757

Norio, O., T. Ye, Y. Kajitani, P. Shi and H. Tatano (2011), The 2011 Eastern Japan Great Earthquake Disaster: Overview and Comments, Int. J. Disaster Risk Sci., 2, 34-42

Odell, K. and M. D. Weidenmier (2001), Real Shock, Monetary Aftershock: The 1906 San Francisco Earthquake and the Panic of 1907, Claremont Colleges Working Papers in Economics, No. 2001-07, 22 pp.

Parsons, T., S. Toda, R. S. Stein, A. Barka and J. H. Dieterich (2000), Heightened Odds of Large Earthquakes Near Istanbul: An Interaction-Based Probability Calculation, Science, 288, 661-665

Parsons, T. (2005), Significance of stress transfer in time-dependent earthquake probability calculations, J. Geophys. Res., 110, B05S02

Paté-Cornell, E. (2012), On “Black Swans” and “Perfect Storms”: risk analysis and management when statistics are not enough, Risk Analysis, 32, 1823-1833

Petrova, E. G. and E. Krausmann (2011), From natural hazards to technological disasters, *Nat. Hazards Earth Syst. Sci.*, 11, 3063-3065

Pohl, R. 2000. Failure frequency of gates and valves at dams and weirs. International Journal on Hydropower & Dams(6):77-81

Polese, M., M. Di Ludovico, A. Prota and G. Manfredi (2013), Damage-dependent vulnerability curves for existing buildings, Earthquake Engng Struct. Dyn., 42, 853-870, doi: 10.1002/eqe.2249

Poliakov, A. N. B., R. Dmowska and J. R. Rice (2002), Dynamic shear rupture interaction with fault bends and off-axis secondary faulting, J. Geophys. Res., 107, 2295

Reiter, L. (1990), Earthquake Hazard Analysis: Issues and Insights, Columbia University Press, 254 pp.

Romanowicz, B. and L. J. Ruff (2002), On moment-length scaling of large strike slip earthquakes and the strength of faults, Geophys. Res. Lett., 29, 1604, doi: 10.1029/2001GL014479

Rong, Y., D. D. Jackson, H. Magistrale and C. Goldfinger (2014), Magnitude Limits of Subduction Zone Earthquakes, Bull. Seismol. Soc. Am., 104, 2359-2377, doi: 10.1785/0120130287

Rosakis, A. J., O. Samudrala and D. Coker (1999), Cracks Faster than the Shear Wave Speed, Science, 284, 1337-1340

Seed, H. and J. Duncan (1981). The Teton dam failure–a retrospective review. Pages 15-19 in Soil mechanics and foundation engineering: proceedings of the 10th international conference on soil mechanics and foundation engineering, Stockholm

Si, Y. and D. Qing (1998). The World's most catastrophic dam failures: the August 1975 collapse of the Banqiao and Shimantan dams.in J. Thibodeau and P. B. Williams, editors.

The river dragon has come! The three gorges dam and the fate of China's Yangtze River and its people. M.E. Sharpe,, Armonk, New york, USA

Stirling, M., T. Goded, K. Berryman and N. Litchfield (2013), Selection of Earthquake Scaling Relationships for Seismic-Hazard Analysis, Bull. Seismol. Soc. Am., 103, 2993-3011, doi: 10.1785/0120130052

Taleb, N. N. (2007), The Black Swan: the impact of the highly improbable, Random House, New York

Toda, S., R. S. Stein, P. A. Reasenber, J. H. Dieterich and A. Yoshida (1998), Stress transferred by the 1995 M_w = 6.9 Kobe, Japan, shock: Effect on aftershocks and future earthquake probabilities, J. Geophys. Res., 103, 24543-24565

Toda, S., R. S. Stein, K. Richards-Dinger and S. Bozkurt (2005), Forecasting the evolution of seismicity in southern California: Animations built on earthquake stress transfer, J. Geophys. Res., 110, B05S16

Toda, S., R. S. Stein, V. Sevilgen and J. Lin (2011), Coulomb 3.3 Graphic-rich deformation and stress-change software for earthquake, tectonic, and volcano research and teaching – user guide, U.S. Geological Survey Open-File Report 2011-1060, 63 pp.

van Aalst, M. K. (2006), The impacts of climate change on the risk of natural disasters, Disasters, 30, pp. 5-18

Wells, D. L. and K. J. Coppersmith (1994), New Empirical Relationships among Magnitude, Rupture Length, Rupture Width, Rupture Area, and Surface Displacement, Bull.Seismol. Soc. Am., 84, 974-1002

Wesnousky, S. G. (1986), Earthquakes, Quaternary Faults, and Seismic Hazard in California, J. Geophys. Res., 91, 12587-12631

Wesnousky, S. G. (2006), Predicting the endpoints of earthquake ruptures, Nature, 444, 358-360

Wesnousky, S. G. (2008), Displacement and Geometrical Characteristics of Earthquake Surface Ruptures: Issues and Implications for Seismic-Hazard Analysis and the Process of Earthquake Rupture, Bull. Seismol. Soc. Am., 98, 1609-1632, doi: 10.1785/0120070111

Wheeler, R. L. (2009), Methods of Mmax Estimation East of the Rocky Mountaints, U.S. Geological Survey Open-File Report 2009-1018, 44 pp.

Wieland, M (2014). Seismic hazard and seismic design and safety aspects of large dam projects. Second European Conference on Earthquake Engineering and Seismology, Istambul

Xu, Y. and L. M. Zhang (2009). Breaching parameters for earth and rockfill dams. Journal of Geotechnical and Geoenvironmental Engineering 135(12):1957-1970

Yen, Y.-T. and K.-F. Ma (2011), Source-Scaling Relationship for *M* 4.6-8.9 Earthquakes, Specifically for Earthquakes in the Collision Zone of Taiwan, Bull. Seismol. Soc. Am., 101, 464-481, doi: 10.1785/0120100046

Yeo, G. L. and C. A. Cornell (2009), A probabilistic framework for quantification of aftershock ground-motion hazard in California: Methodology and parametric study, Earthquake Engng Struct. Dyn., 38, 45-60, doi: 10.1002/eqe.840

Zöller, G., M. Holschneider and S. Hainzl (2013), The Maximum Earthquake Magnitude in a Time Horizon: Theory and Case Studies, Bull. Seismol. Soc. Am., 103, 860-875, doi: 10.1785/0120120013